การพัฒนาสถานีทดลองกล้องจุลทรรศน์โฟโตอิเล็กตรอนและการศึกษา
กราฟีนเตรียมโดยการสลายตัวด้วยความร้อนของซิลิกอนคาร์ไบด์

นางสาว จริน โอะคลัง

DEVELOPMENT OF PEEM EXPERIMENTAL STATION

AND STUDY OF GRAPHENE FORMED BY THERMAL

DECOMPOSITION OF SiC

Jarin Osaklung

A Thesis Submitted in Partial Fulfillment of the Requirements for the

Degree of Doctor of Philosophy in Physics

Suranaree University of Technology

Academic Year 2011

DEVELOPMENT OF PEEM EXPERIMENTAL STATION AND

STUDY OF GRAPHENE FORMED BY THERMAL

DECOMPOSITON OF SiC

Suranaree University of Technology has approved this thesis submitted in partial fulfillment of the requirements for the Degree of Doctor of Philosophy.

Thesis Examining Committee

_____

(Asst. Prof. Dr. Chinorat Kobdaj)

Chairperson

_____

(Assoc. Prof. Dr. Prayoon Songsiriritthigul)

Member (Thesis Advisor)

_____

(Dr. Chanan Euaruksakul)

Member

_____

(Asst. Prof. Dr. Supagorn Rugmai)
Member

_____

(Dr. Worawat Meevasana)

Member

_____

(Dr. Hideki Nakajima)

Member

_____   _____

(Prof. Dr. Sukit Limpijumnong)   (Assoc. Prof. Dr. Prapun Manyum)

Vice Rector for Academic Affairs   Dean of Institute of Science

จริน โอษะคลัง : การพัฒนาสถานีทดลองกล้องจุลทรรศน์โฟโตอิเล็กตรอนและการศึกษา
กราฟีนเตรียมโดยการสลายตัวด้วยความร้อนของซิลิกอนคาร์ไบด์ (DEVELOPMENT
OF PEEM EXPERIMENTAL STATION AND STUDY OF GRAPHENE FORMED BY
THERMAL DECOMPOSITION OF SiC) อาจารย์ที่ปรึกษา : รองศาสตราจารย์ ดร.
ประยูร ส่งสิริฤทธิกุล, 161 หน้า.

วิทยานิพนธ์นี้มุ่งเน้นการวินิจฉัยการจัดเรียงตัวของอิพิแทกเซียลกราฟีน (Epitaxial
graphene) บนซิลิกอนคาร์ไบด์ชนิด 6H-SiC(0001) ด้วยวิธีสลายตัวเนื่องจากความร้อน (Thermal
decomposition) โดยในส่วนแรกของวิทยานิพนธ์จะประกอบด้วยการพัฒนาเครื่องมืออุปกรณ์ที่
จำเป็นสำหรับการก่อเกิดและใช้สำหรับวิเคราะห์ ณ ขณะที่เกิดจากจัดเรียงตัวของเอพิแทกซิกราฟีน
(in situ analyze) เครื่องมืออุปกรณ์ที่พัฒนาขึ้นนี้คือสถานีทดลองของระบบลำเลียงแสงซินโคร
ตรอน โดยสถานีทดลองดังกล่าวจะใช้แสงที่ผลิตจากแม่เหล็กเชิงระนาบอันดูเลเตอร์ (Planar
undulator) เพื่อวิเคราะห์สมบัติของวัสดุด้วยเทคนิคกล้องจุลทรรศน์อิเล็กตรอนที่อาศัยโฟโต
อิเล็กตรอนที่หลุดจากผิวตัวอย่างเพื่อทำให้เกิดภาพ (Photoemission electron microscopy, PEEM)
ทั้งนี้ได้ดำเนินการตั้งแต่เริ่มติดตั้งสถานีทดลองตลอดจนทดสอบการใช้งานของระบบลำเลียงแสง
ในส่วนของการจัดเรียงตัวใหม่ของอะตอมบนผิวและการก่อเกิดกราฟีนได้ทำการตรวจสอบด้วย
เทคนิคการศึกษาความเป็นผลึกของสารตัวอย่าง โดยเทคนิคการแทรกสอดของอิเล็กตรอนพลังงาน
ต่ำ (LEED) ซึ่งเป็นส่วนหนึ่งของการประยุกต์ใช้ของกล้องจุลทรรศน์อิเล็กตรอนชนิดนี้ อีกทั้งได้
บันทึกภาพถ่ายจากเทคนิคกล้องจุลทรรศน์นี้ทั้งจากการกระตุ้นด้วยอิเล็กตรอนและโฟตอน
(LEEM/PEEM) บนผิวสารตัวอย่างซิลิกอนคาร์ไบด์ทั้งก่อนและหลังการเกิดกระบวนการจัดเรียงตัว
ใหม่ของอะตอมบนพื้นผิว ซึ่งการแกว่งกวัดของเส้นโค้งระหว่างความเข้มของภาพ LEEM กับความ
ต่างศักย์ที่ใช้ (IV-LEEM) สามารถใช้บ่งบอกจำนวนชั้นของเอพิแทกซิกราฟีนได้นับได้ว่าเป็นครั้ง
แรกที่มีการศึกษาค้นคว้าอิทธิพลของรอยขูดขีดบนผิวซิลิกอนคาร์ไบด์ในการก่อเกิดกราฟีนและวัด
การแปรผันขนาดความกว้างกับจำนวนชั้นของเอพิแทกซิกราฟีนบนพื้นผิวซิลิกอนคาร์ไบด์ ทั้งนี้ได้
นำเสนอแบบจำลองที่ใช้อธิบายผลการทดลองเหล่านี้ด้วย

สาขาวิชาฟิสิกส์   ลายมือชื่อนักศึกษา _____

ปีการศึกษา 2554   ลายมือชื่ออาจารย์ที่ปรึกษา _____

             ลายมือชื่ออาจารย์ที่ปรึกษาร่วม_____

JARIN OSAKLUNG : DEVELOPMENT OF PEEM EXPERIMENTAL
STATION AND STUDY OF GRAPHENE FORMED BY THERMAL
DECOMPOSITION OF SiC. THESIS ADVISOR : ASSOC. PROF.
PRAYOON SONGSIRIRITTHIGUL, Ph.D. 161 PP.

EPITAXIAL GRAPHENE/SILICON CARBIDE/LOW ENERGY ELECTRON
MICROSCOPY/SUBSTRATE SCRATCH

This thesis focuses on the investigations of epitaxial graphene formed by
thermal decomposition of 6H-SiC(0001). The first part of the thesis was the
instrument development, which is the construction of the PEEM experimental station
of the BL3.2a beamline of Synchrotron Light Research Institute (SLRI). The
experimental station utilizes light produced from a planar undulator for materials
analyses based on photoemission electron microscopy. The construction of the
experimental station was completed and the commissioning of the system was
successful. The experimental station was then used for the formation and in-situ
analysis of the epitaxial graphene. Surface reconstruction and the formation of
graphene was monitored by in-situ low-energy electron diffraction using the available
electron microscope. The images of SiC before and after surface decomposition were
observed and recorded by low-energy electron microscopy (LEEM). Intensity-
Voltage LEEM (IV-LEEM) curves were used for determination of number of the
graphene layers. It was the first time to find that there is influence of scratch on the
SiC surface on the formation of the graphene and that there is a spatial variation of the

number of graphene layers on the SiC surface. A model to explain the finding has been proposed.
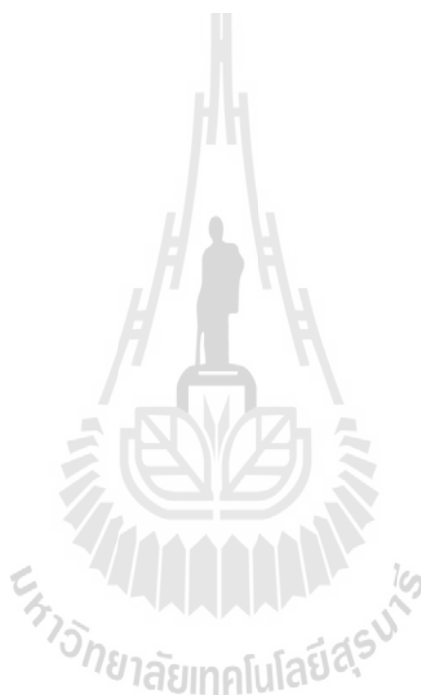
School of Physics Student's Signature _____

Academic Year 2011 Advisor's Signature _____

Co-advisor's Signature _____

ACKNOWLEDGEMENTS

Technology. Importantly, I would like to express thanks to my parents and Dr. Chalermphol Kanchanawarin for their kind support and encouragement.

CONTENTS

CONTENTS (Continued)

CONTENTS (Continued)

CONTENTS (Continued)

LIST OF TABLES

LIST OF FIGURES

LIST OF FIGURES (Continued)

LIST OF FIGURES (Continued)

LIST OF FIGURES (Continued)

LIST OF FIGURES (Continued)

LIST OF FIGURES (Continued)

LIST OF FIGURES (Continued)

LIST OF FIGURES (Continued)

LIST OF FIGURES (Continued)

LIST OF FIGURES (Continued)

LIST OF ABBREVIATIONS

ABS   =   A Heat Absorber

AES   =   Auger Electron Spectroscopy

AFM   =   Atomic Force Microcopy

BL   =   Beam Line

BMP   =   A Photon Beam Position Monitor

BS   =   Bremsstrahlung Shutter

C1(2, 3)   =   Condenser Lens 1(2, 3)

EG   =   Epitaxial Graphene

FBZ   =   First Brillouin Zone

FET   =   Field Effect Transistor

FL   =   Field Lens

FLG   =   Few Layers Graphene

FLG   =   Few layers Graphene

FOV   =   Field of View

GNR   =   Graphene nano Ribbon

HBT   =   High Energy Beam Transport Line

HF   =   Hydro Fluoro Acid

IL   =   Inner Lens

IMFP   =   Inelastic of Electron Mean Free Path

IV-LEEM   =   Intensity Voltage LEEM

LIST OF ABBREVIATIONS (Continued)

LBT	=	Low Energy Beam Transport Line
LEED	=	Low Energy Electron Diffraction
LEED	=	Low Energy Electron Diffraction
LEEM	=	Low Energy Electron Microscopy/cope
LINAC	=	Linear Accelerator
LL	=	Landau Level
MBE	=	Molecular Beam Epitaxial
MCP	=	Multi-Channel Plate
Micro-XAS	=	Micro X-ray Absorption Spectroscopy
Micro-XPS	=	Micro X-ray Photoemission Spectroscopy
NEXAFS	=	Near Edge X-ray Absorption Fine Structure
P1(2, 3)	=	Projector Lens 1(2, 3)
PEEM	=	Photoemission Electron Microscopy/cope
PES	=	Photoemission Spectroscopy
PES	=	Photoemission Spectroscopy
QHE	=	Quantum Hall Effect
SEM	=	Scanning Electron Microscopy
SET	=	Single Electron Transistor
SLRI	=	Synchrotron Light Research Institute (Public Organization)
SMOKE	=	Surface Magneto Optical Kerr Efect
SPS	=	Siam Photon Source
STR	=	Storage Ring

LIST OF ABBREVIATIONS (Continued)

TEM	=	Transmission Electron Microscopy
TL	=	Transfer Lens
UHV	=	Ultrahigh Vacuum
VLSPG	=	Varied-line-spacing plane -grating
WSL	=	Wavelength Shifter
XANES	=	X-ray Absorption Near Edge Spectrum
XMCD	=	X-ray Magnetic Circular Dichroism
XMLD	=	X-ray Magnetic Linear Dichroism
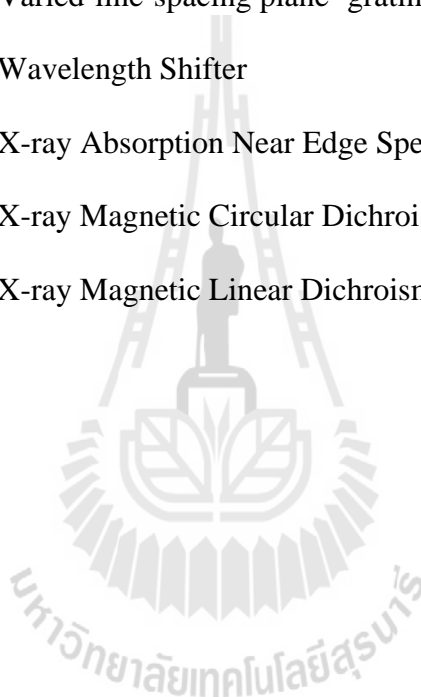
CHAPTER I

INTRODUCTION

1.1 Overview

Graphene is one of the most recent interesting carbon-based materials. It is a monolayer of carbon atoms arranging in a two-dimensional honeycomb lattice which is a basic building block for graphitic materials i.e., fullerenes, nanotubes or graphite. It was first pointed out by theoretical study based on the properties of graphite by Wallace (1947) and Charlier et al. (2008). In Wallace (1947), the 2D structure of graphene was believed to be unstable. Nevertheless, there have been several attempts to extract single graphene sheets with the first successful attempt by May et al. (1969) as a "disorder structure" on platinum surfaces heated in ultra-high vacuum, indicating the first deposition of a single graphitic sheet. In 1999, The Ruoff group at Washington University initiated the route of single-layer graphene sheet fabrication by micromechanical exfoliation of graphite (Lu et al., 1999). However, in 2004 the first graphene monolayer device was presented by a Manchester group as reported by Novoselov et al. (2004). Thereafter, many novel properties of graphene obtained from different research groups have been reported, such as the room-temperature quantum Hall effect (QHE) by Novoselov et al. (2004), extremely-high mobility by Geim and Novoselov (2007), half-metallic nanoribbon by Son et al. (2006), Raman study by Faugeras et al. (2008), plasmons by Bostwick et al. (2008), x-ray absorption by Gao et al. (2008), as summarized in Table 1.1.

Table 1.1   The summary of graphene properties.

Properties	Graphene	Remark
Atomic properties	ripple flat sheet with density less than 1g/cm^3	Linear dispersion (Geim and Novoselov (2007))
Electronic properties	Zero gap semiconductor. Zero effective mass for electron and hole.	Charlier et al. (2008)
Electronic transport	mobility = 15,000 cm^2/Vs at room temp. (Geim and Novoselov (2007))	Resistivity of EG =1 0-6 Ωm. Less than Ag @ room temp.
Optical properties	Absorbs 2.3% of white light	(Nair et al., 2008)
Spin transport	Spintronic (small spin-orbit interaction) (Nikolaos et al (2007))	Absence of nuclear magnetic moment
Anomalous QHE	$\sigma = \pm\ 4(N+\frac{1}{2})\ e^2/h$ (Geim and Novoselov (2007))	Normally $\sigma = N(\ e^2/h)$
Nanostripes: Spin-polarized edge current	Zigzag graphene show spin-polarized metallic edge current-> spin field electronic (Neto et al. (2009))	Armchair graphene show spin-polarized semiconducting edge current
Graphene oxides	By oxidizing and chemically processing graphene and floating them in water	Tensile modulus ~32 GPa. Daniel et al. (2010)

Table 1.1   The summary of graphene properties (Continued).

Properties	Graphene	Remark
Mechanical properties	Strongest material ever tested (Lee et al. (2008))	By Atomic Force Microscopy $\rightarrow$ Y$\approx$ 0.5 TPa
Thermal properties	5.3×10^3 W/mK	Shanshan et al. (2012)

There are various methods for graphene synthesis. Table 1.2 shows some graphene fabrication techniques with advantages and disadvantages in terms of ease-of-use, quality and scalability for each technique.
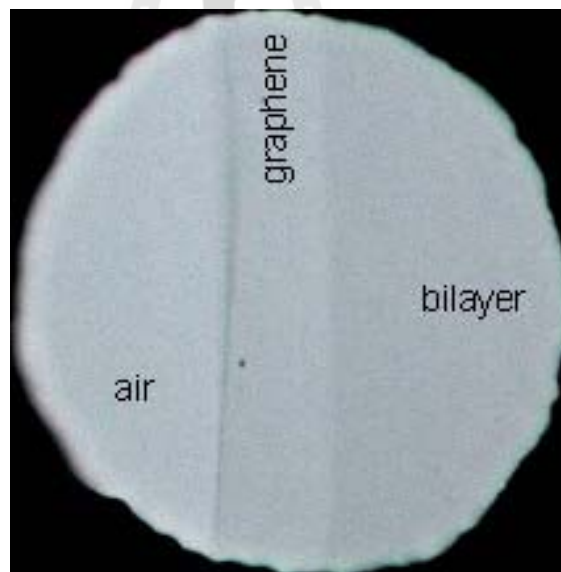
Figure 1.1 Graphene as it appears to an optical microscope examination (Nair et al., 2008).

Table 1.2 Advantage and disadvantage of different graphene fabrication techniques.

Technique	Process	Advantage	Disadvantage
Chemical Exfoliation (Michael, 2009)	Inserting molecules into bulk graphite to separate the crystalline planes in to individual graphene layer	Its facile chemical approach	After the intercalating molecules are removed from the mixture, the resultant C compounds is "sludge" (contains restacked and scrolled graphene sheets)
Micromechanical cleavage (Geim and MacDonald, 2007)	Peel off individual layers of graphene from bulk graphite i.e. rubbing a piece of graphite by adhesive tape	Single-layer graphene (flake) up to 100 μm in size	Difficult to locating individual graphene flakes produce on substrate.
Epitaxial growth -Chemical Vapor deposition (Obraztsov, 2009) -Thermal decomposition on SiC (Sutter, 2009)	CVD of hydrocarbons deposited on metal substrate Heated over 1200 °C	Graphene can mounted on SiC for device integration - FLG exhibit high mobile charge transfer	Large scale integration. Residue of the metal substrate might not be compatible with electronic fabrication. Need high-temperature vacuum processing.
Hydrazine reduction	Placing graphene oxide paper in Sol of pure hydrazine (Ni+H)	Reduce graphene oxide paper into Single-G	
From nanotubes (Jiao et al., 2009)	1. Cutting MW-CNT in sol. by action of Potassium permanganate and sulfuric acid.	2. Plasma etching of nanotubes partly embed in a polymer film	

Due to the salient properties of graphene, it becomes a promising material to be used in various applications. The brief overviews of the more recent main applications of graphene are summarized as following:

a. Polymer nanocomposite materials: Graphene in polymer nanocomposite materials show an extraordinary improvement of several important properties i.e. electrical conductivity, thermal stability, elastic modulus and tensile strength. The manufacturing of such composites requires not only that graphene sheets be produced on a sufficient scale but also be incorporated, and homogeneously distributed into various matrices. A nanocomposite formed by molecular-level graphene dispersion of individual, chemically modified graphene sheets within polystyrene host has been proved by Stankovich et al. (2006) that it exhibits a percolation threshold of 0.1 volume percent and a conductivity of 0.1 S/m, sufficient for many electrical applications.

b. Electronic devices: Graphene applications on electronic devices are given as follows:

    - Field effect transistor (FET) Graphene's ballistic transport across sub-micron distances enables super-fast switching and computation. The achievement of FETs fabricated on a 2-inch graphene wafer with a cut-off frequency in the radio frequency range as high as 100 GHz was reported by Xia et al. (2010). They also achieved a dual-gate bilayer graphene FETs with an on/off current ratio of around 100 and 2000 at room temperature and 20 K, respectively.

    - Single electron transistor (SET) Graphene can be carved into ribbons and islands to form quantum nanostructures-using a combination of e-beam lithography

and dry etching called graphene nanoribbons (GNRs). Unlike other SETs, the all-graphene SET is capable of room-temperature operation.

c. Magneto-electronic devices: (Cai et al., 2010) Narrow GNRs should have large bandgaps, and show tunable properties that depend on the direction of the ribbon relative to the graphene lattice. However, it has been difficult to achieve the atomic-scale control necessary to fabricate GNRs of precise width and direction. That has changed with a recent report in 2010 by Cai and colleagues who demonstrated the assembly of atomically-precise GNRs from molecular precursors on metallic substrates. Zigzag graphene shows spin-polarized metallic edge current, i.e. negligible spin-orbit coupling. Therefore, graphene-based devices have spin-injection and spin-valve effects at room temperature (in spin injection,spin-polarized electrons were injected, resulting in a 10% change in resistance of graphene when interfaced electrodes were switched from the parallel to the antiparallel state).

Furthermore, high electrical conductivity and high optical transparency of graphene make it a promising candidate for transparent conducting electrodes as examined by Li et al. (2008). Employing also its mechanical properties, the macroscopic use of graphene has been demonstrated in the fabrication of flexible, stretchable and foldable electronics by Kim et al. (2009). The fabrication of clean energy devices from graphene-based materials are exploited as electrodes for rechargeable lithium ion batteries and ultra capacitors by Yoo et al. (2008), and Yu and Dai (2010). At last, due to a surface-volume ratio very favorable, graphene demonstrates step-like increase of resistance when a gas molecule attaches to or detaches from its surface, making it suitable to detect single molecules for applications in chemical sensors (Robinson et al., 2008).

1.2 Purpose of this thesis work

One of the main goals of this thesis work is to be able to synthesize graphene by thermal decomposition of a single-crystal SiC, which is a promising technique for large-scale fabrication of few layers graphene (FLG). It is well-known that the properties of graphene are largely dependent on the number of layers such as bandgap opening (Castro et al., 2007, and Ohta et al., 2005) and plasmaron coupling (Bostwick et al., 2010), but the method to pattern the graphene with different numbers of layers is still under development. So far, the in-plane size of uniform graphene obtained by thermal decomposition method is limited to about 3 μm × 5 μm as reported by Emtsev et al. (2009), and 50 μm × 50 μm as reported by Virojanadara et al. (2009). The main problem for thermal-decomposition graphene on SiC is that the FLG obtained so far has had a thickness distribution through the substrate surface due to the roughness of or scratches on the SiC a surface which is one of the factors limiting growth process. To better understand the formation and shape of epitaxially grown graphene, in this study the effects of substrate scratches (~0.2 μm in width) on the spatial variation of graphene layers formed on a 6H–SiC(0001) surface were investigated. The number of graphene layers over selected surface areas were extracted and analyzed by using low-energy electron microscopy (LEEM) using the method called IV-LEEM (Intensity–Voltage LEEM images) analysis.

A large part of this thesis work involved the development of the PEEM experimental station, which is the main instrument used for fabrication and in-situ characterizations of graphene. The PEEM experimental station is connected to the beamline 3.2b of the Synchrotron Light Research Institute (Public Organization), SLRI. Participation in the design, construction and commissioning of the PEEM

experimental station provided me to be trained on advanced instrumentation and many engineering technologies such as vacuum technology and control/data acquisition technology, as well as beamline technology.

1.3 References

Bostwick, A., Emtsev, K. V., Horn, K., Huwald, E., Ley, L., McChesney, J. L., Ohtta, T., Riley, J., Rotenberg, E., Speck, E. F. and Seyller, Th. (2008). Photoemission studies of graphene on SiC: Growth, Interface, and Electronic Structure. **Adv. in Solid State Phys.** 47: 159

Cai, J., Ruffieux, P., Jaafar, R., Bieri, M., Braun, T., Blankenburg, S. Muoth, M., Seitsonen, A. P., Saleh, M., Feng, X., Mullen, K. and Fasel, R. (2010). Atomically prrcise bottom-up fabrication of graphene nanoribbons. **Nature** 466: 470-473.

Charlier, J.-C., Eklund, P. C., Zhu, J. and Ferrari, A. C. (2008) Electron and phonon properties of graphene: their relationship with carbon nanotubes. In Dresselhaus, J. M. S. and Dresselhaus. G. (ed.). **Springer Series on Topics in Appl. Phys.** 111: 673-708.

Daniel, R. D., Sungjin, P., Christopher, W. B. and Rodney, S. R. (2010). The chemistry of graphene oxide. **Chem. Soc. Rev.** 39: 228-240.

Emtsev, K. V., Bostwick, A., Horn, K., Jobst, J., Kellogg, G. L., Ley, L., McChesney, J. L., Ohta, T., Reshanov, S. A., Rohrl, J., Rotenberg, E., Schmid, A. K., Waldmann, D., Weber, H. B. and Seyller, Th. (2009). Toward wafer-size graphene layers by atmospheric pressure graphitization of silicon carbide. **Nat. Mater.** 8: 203-207.

Faugeras, C., Nerriere, A., Potemski, M., Mahmood, A., Dujardin, E., Berger, C. and De Heer, W. A. (2008). Few-layer graphene on SiC, pyrolitic graphite, and graphene: A Raman scattering study. **Appl. Phys. Lett.** 92: 011914 1-3.

Gao, X., Chen, S., Liu, T., Chen, W. and Wee, A. T. S. (2008). Disorder beneath epitaxial graphene on SiC(0001): An x-ray absorption study. **Phys. Rev. B** 78: 201404(R)1-4.

Geim, A. K. and Novoselov, K. S. (2007). The rise of graphene. **Nat. Mater.** 6: 183-191.

Geim, A. K. and MacDonald, A. H. (2007). Graphene: Exploring carbon flatland. **Physics Today** 60(8): 35-41.

Jiao, L., Zhang, L., Wang, X., Diankov, G. and Dai, H. (2009). Narrow graphene nanoribbons from carbon nanotubes. **Nature** 458(7240): 877-8

Kim, K. S., Zhao, Y., Jang, H., Lee, S. Y., Kim, J. M., Kim, K. S., Ahn, J. H., Kim, P., Choi, J. Y. and Hong, B. H. (2009). Large-scale pattern growth of graphene films for stretchable transparent electrodes. **Nature** 457: 706-710.

Lee, C., Wei, C., Kysar, J. And Hone, J. (2008). Measurement of the Elastic Properties and Intrinsic Strength of Monolayer Graphene. **Science** 321(5887): 385-8.

Li, X., Zhang, G., Bai, X., Sun, X., Wang, X., Wang, E. and Dai, H. (2008). Highly conducting graphene sheets and Langmuir-Blodgett films. **Nat. Nanotech.** 3: 528-542.

Lu, X. K., Yu, M. F., Huang, H. and Ruoff, R. S. (1999). Tailoring graphite with the goal of achieving single sheets, **Nanotechnology.** 10: 269-272.

May, J. W. (1969). Platinum surface LEED rings. **Surf. Sci.** 17: 267-270.

Michael, S. (2009). Selling graphene by the ton. **Nat. Nanotechnol.** 4 (10): 612-4.

Nair, P. R., Blake, P., Grigorenko, A. N., Novoselov, K. Sl, Booth, T. J., Stauber, T., Peres, N. M. R. and Geim, A. K. (2008). Fine Structure Constant Defines Visual Transparency of Graphene. **Science** 320(5881): 1308.

Neto, A. C., Guinea, F., Peres, N. M. R., Novoselov, K. S. and Geim. A. K. (2009). The electronic properties of graphene. **Rev Mod. Phys.** 81: 109

Novoselov, K. S., Geim, A. K., Morozov, S. V., Jiang, D., Zhang, Y., Dubonos, S. V., Grigorieva, I. V. and Firsov, A. V. (2004). **Science** 306: 666-669.

Novoselov, K. S., Geim, A., K., Morozov, S. V., Jiang, D., Katsnelson, M. I., Grigorieva, I. V. Dubonous, S. V. and Firsov, A. A. (2005). Two-dimension gas of massless Dirac fermions in graphene. **Nature** 438: 197-200.

Novoselov, K. S., Jiang, D., Schedin, F., Booth, T. J., Khotkevich, V. V., Morozov, S. V. and Geim, A. K. (2005). Two-dimensional atomic crystals. (Editted by Rice, T. M). **PNAS** 102: 10451-10453.

Ohta, T. Bostwick, A. McChesney, J. L., Seyller, T., Horn, K. and Rotenberg, E. (2007). Interlayer interaction and electronic screening in multilayer graphene investigated with Angle-Resolved Photoemission Spectroscopy. **Phys. Rev. Lett.** 98: 206802 1-4.

Obraztsov, A. X. (2009). Chemical vapour deposition: Making graphene on a large scale. **Nat. Nanotechnol.** 4: 212-213.

Polichetti, T. Miglietta, M. and Fracia, G. D. (2010). Overview on graphene: Properties, fabrication and applications. **Chemistry Today/chimica orri** 28: 6-9.

Robinson, J. T., Perkins, F. K., Snow, E. S., Wei, Z. and Sheehan, P. E. (2008). Reduced graphene oxide molecular sensors. **Nano. Lett.** 8(10): 3137-3140.

Son, Y. W., Cohen, M. L. and Louis, S. G. Half-metallic graphene nanoribbons. **Nat. Lett.** 444: 347-349.

Shanshan, C., Qingzhi, W., Columbia, M., Junyong, K., Hengji, Z., Kyeongjae, C., Weiwei, C., Alexander, B. (2012). Thermal conductivity of isotopically modified graphene. **Nat. Mater.** 11(3): 203-207.

Stankovic, S., Dikin, D. A., Dommett, G. H. B., Kohlhaas, K. M., Zimney, E. J., Stach, E. A., Piner, R. D., Nguyen, S. T. and Ruoff, R. S. (2006). Graphene-based composite materials. **Nature** 442: 282-286.

Sutter, P. (2009). Epitaxial graphene: How silicon leaves the scene. **Nat. Mater.** 8 (3): 171-2

Virojanadara, C., Yakimova, R., Osiecki, J. R., Syvajarvi, M., Uhrberg, R. I. G., Johansson, L. I. and Zakharov, A. A. (2009). Substrate orientation : A way towards higher quality monolayer graphene growth on 6H-SiC(0001). **Surf. Sci.** 603: L87-L90.

Wallace, P. R. (1947). "The Band Theory of Graphite". **Phys. Rev.** 71 (9): 622-634.

Xia, F., Farmer, D. B., Lin, Y. M. and Avouris, P. (2010). Graphene Field-Effect Transistors with High On/Off Current Ratio and Large Transport Band Gap at Room Temperature. **Nano. Lett.** 10(2): 715-718.

Yoo, E., Kim, J., Hosono, E., Zhou, H. S., Kudo, T. and Honma, I. (2008). Large reversible Li storage of graphene nanosheet families for use in rechargeable Lithium Ion batteries. **Nano. Lett.** 8(8): 2277-2282.

Yu, D. and Dai, L. (2010). Self-assembled graphene/carbon nanotube hybrid films for supercapacitors. **J. Phys. Chem. Lett.** 1(2): 467-470.

CHAPTER II

THEORETICAL BACKGROUND

Fundamental physics of graphene such as two dimensional lattices, electronic band structure and its substrate, silicon carbide (SiC), are described. According to assembly growth method for synthesized graphene in this study, the purpose of study about surface and thin film growth, the theoretical approaches is very important. Physics of surface science and thin film growth are also demonstrated. Furthermore, it is also important to understand surface characterization techniques which help us to choose appropriate methods of sufficient sensitivity for graphene research. The inception of study surface mechanism is based on vacuum technology, the development of surface analytical techniques. Most of my thesis was carried out in the LEEM system which is the electron microscope based technique. Therefore, the principle reveal with electron microcopy for surface science, the theory about electron in solid as well as the description about electron microscope such as electron source and electron analyzer are mentioned in this chapter.

2.1 Structural properties of graphene

2.1.1 Monolayer graphene

Graphene has a honey comb lattice structure which arises from the sp^2 hybridization with three σ in-planes, each containing one electron. Another one orbital is p_z orbital which is perpendicular to the hexagonal plane and forms π bonds with

other carbon atoms. This is called half-filled system which determines the unusual electronic properties of graphene. The Brillouin zone of graphene is also a hexagonal lattice which has a bipartite symmetry, sublattices A and B, as shown in Figure 1. The wave functions of graphene in the plane are indicated by Wallace (1947) as

$$\frac{1}{\sqrt{3}}\left(\psi_C(2s)+\sqrt{2}\psi_C(\sigma_i 2p)\right) \qquad (i=1,2,3), \qquad (2.1)$$

where $\psi_C(2s)$ is the carbon 2s wave function and $\psi_C(\sigma_i 2p)$ are the 2p wave functions whose axes are in the direction joining the three neighbor carbon atom in a plane. The hexagonal spacing in the layer is $\approx 1.42\,\overset{\circ}{A}$ while the lattice constant of graphene is $a=1.42\times\sqrt{3}=2.46\,\overset{\circ}{A}$ and the reciprocal lattice vectors have magnitude $\left(2/\sqrt{3}\right)a$ as demonstrated in Figure 2.1. The lattice vectors $\bar{a}_1$, $\bar{a}_2$ and the corresponding reciprocal vectors are determined by

$$\boldsymbol{a_1}=\left(\frac{\sqrt{3}}{2}a,-\frac{1}{2}a\right), \qquad \boldsymbol{a_2}=\left(0,a\right) \qquad (2.2)$$

$$\boldsymbol{b_1}=\left(\frac{4\pi}{\sqrt{3}a},0\right), \qquad \boldsymbol{b_2}=\left(\frac{2\pi}{\sqrt{3}a},\frac{2\pi}{3a}\right). \qquad (2.3)$$

According to the two graphene sublattices, the six corners of FBZ can be divided into two groups called K and K' points. The electronic structure for graphene was developed by Wallace in 1947 by considering the nearest and next-nearest-neighbor interaction for π bonds (p_z-orbital). The study, however, ignored the overlapping σ bonds. In 1998, Saito, Dresselhaus, and Dresselhaus (1999) includes this interaction,

but only nearest neighbors in the plane of graphene, to obtain the two-dimensional

energy dispersion between the π bonding and π^* anti-boding as follows,

$$\Delta E\left(k_x, k_y\right) = 2\gamma_0 \sqrt{1 + 4\cos\left(\frac{\sqrt{3}k_x a}{2}\right)\cos\left(\frac{k_y a}{2}\right) + 4\cos^2\left(\frac{k_y a}{2}\right)}, \qquad (2.4)$$

where $\gamma_0 \approx 3.03$ eV is the nearest neighbor overlay integral in tight-binding

calculation. By using Taylor expansion, Equation (2.4) becomes

$\Delta E\left(\vec{k}\right) = \sqrt{3}\gamma_0 a \left|\vec{k} - \vec{k}_K\right|$ which expresses itself as a linear dispersion near the six

corner of graphene FBZ, where the π and π^* bands meet each other at the Fermi

energy as demonstrated in Figure 2.2. This crossing point is called Dirac point (E_D)

because the electron dynamic in graphene corresponds to the 2D Dirac equation,

which describes the behavior of a ½ spin particle in the relativistic regime. For a more

accurate description, the *ab*-initio calculations must include the third nearest
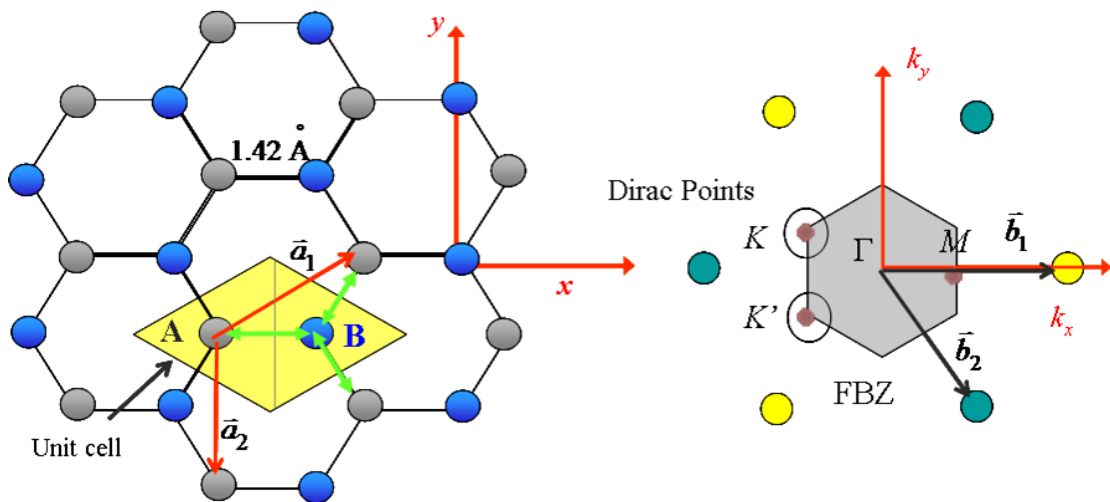
Figure 2.1　(a) Two-dimensional hexagonal lattice of graphene with one unit cell

consisting of two interpenetrating triangular sublattices: A and B, corresponding the

unit vector $\vec{a}_1$ and $\vec{a}_2$. (b) First Brillouin zone (FBZ) in reciprocal space of graphene.
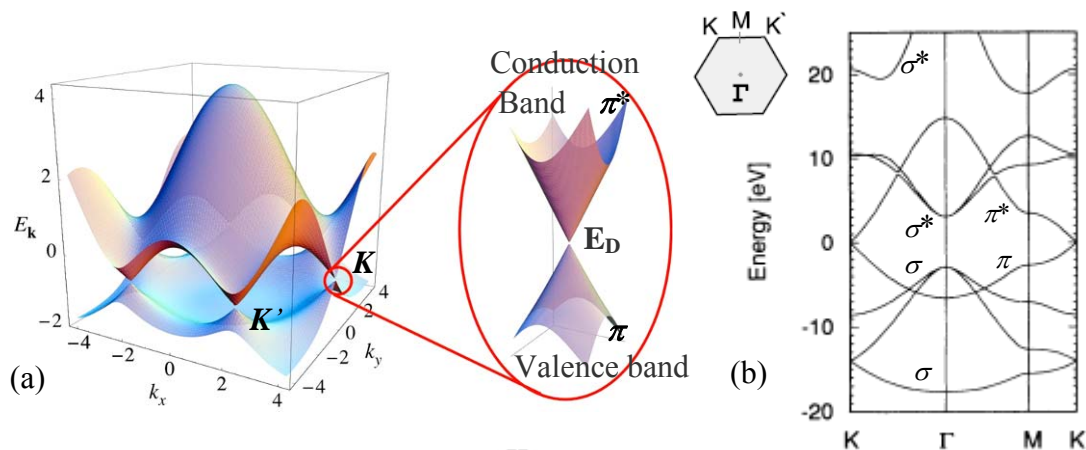
Figure 2.2 (a) The 3D electronic structure of graphene from Novoselov et al. (2009) which expresses the linear energy dispersion at the six corner first Brillouin where the π and π^* bands meet each other at Fermi energy and (b) the tight-binding approach for π and σ bands of graphene calculated by Saito et al. (1999).

neighbors for tight-binding descriptions by Reich, Maultzsch, Thomsen and Ordejón (2002). Monolayer graphene exhibits no gap, hence it can be seen as a zero-gap semiconductor or semimetal.

2.1.2 Bilayer graphene

Unlike monolayer graphene, bilayer or few-layer graphene have different electronics structures in the vicinity of the K, K' point. However, only a 10 layers stack of graphene can be regard as graphene according to examinations by Geim and Novoselov (2007) and Ni et al. (2007). Figure 2.3 (c)-(d) depicts the conical bands with linear dispersion that touch at Dirac point for single graphene and hyperbolic bands for bilayer graphene. For bilayer graphene, the two valence and two conduction bands meet at the Fermi level without overlap or gap formation, thus the band are not

linearly dispersion but rather of parabolic shape. It is quoted by Riedk et al. (2010) that increasing the number of graphene layers results in complicated band structure. Since for multilayer graphene, the stacking between the layer does not need to be of Bernal type as in graphite, it can be other types e. g. rhombohedra (ABCABC). Moreover, it is noted that the slight rotations between the layers result in a decoupling of the layer the so called turbostatic stacking which multilayer graphene can exhibit linear bands as monolayer graphene (Shallcross et al., 2008). Latil and Henrard (2006) report the tight-binding calculation for AB stacking or bilayer graphene that the interlayer interaction alters the band near the K, K' point as shown in Figure 2.3 (e) and (f). For electronics applications, it is important to alter the gap of graphene by making narrow strips of graphene, called graphene nanoribbons as reported by Nakada, Fujita, Dresselhaus, and Dresslhaus in (1996) and Son, Cohen and Louie (2006). One of the main challenges for graphene-based electronic devices is its doping method. Currently hetero atom doping, and chemical modification which can both open the band gap and also tune the Fermi level of graphene have been proved by several experimental studies by Zhou et al. (2008, 2010), Gierz et al. (2008, 2010), Ohta et al. (2006), Zhang et al. (2009), and theoretical studies by Yu et al. (2010), Giovannetti et al. (2008), etc.
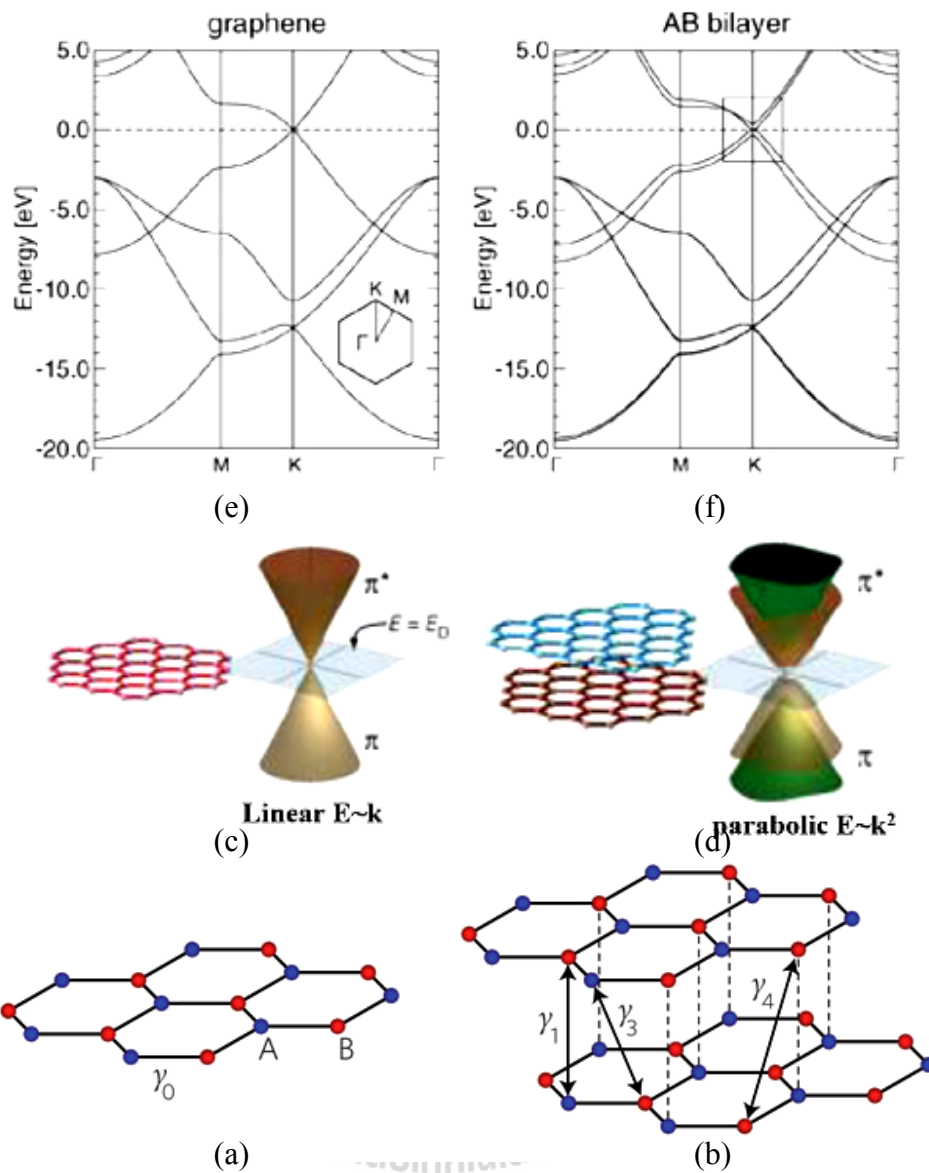
Figure 2.3 (a) The unit cell of single layer graphene with A and B atom. (b) Bilayer graphene consists of two single graphene layers shifted with respect to each other so that the B atoms of one are situated directly above the A atoms of the other. Ohta et al. (2009) presented the conical bands with linear dispersion that touch at Dirac point for single graphene in (c) and for bilayer, this generates an electronic structure that consists of hyperbolic bands in (d). The corresponding electronic band structure calculated by Latil and Henrard (2006) for single and bilayer is indicated in (e) and (f), respectively.

2.2 Electrical properties of graphene

One of the major interesting properties of graphene is the linear energy band spectrum. Graphene is a semi-metal with zero bandgap near six K-points of its Brilloin zone as shown in Figure 2.2 (Wallace, 1947). A linear dispersion relationship of the energy bands of graphene results in zero effective masses for electrons and holes. Consequently, the graphene charge carriers behave like relativistic particles which are described by Dirac equation rather than the usual Schrödinger equation (Geim and Novoselov, 2007). Although the electron moving around carbon atoms of graphene sheet do not really reach relativistic speed, their interactions with the periodic lattice potential make them into quasiparticles, i.e., electrons which have lost their rest mass m_0, or "Dirac massless fermions." The energy of the particle having linear dispersion is given by (Novoselov et al., 2005).

$$E = \frac{|hk|}{2\pi} v_F,$$ (2.5)

where v_F is the Fermi velocity, which is of the order of 10^6 m/s. The dispersion relation of charge carriers in an ordinary conductor is given by

$$E = \frac{h^2 k^2}{2\pi m}.$$ (2.6)

This equation refers that the effective mass of the charge carriers in graphene vanishes at Dirac points (the six K-points of its Brilloin zone) and they travel at the effective speed of light. Moreover, from its linearly dispersive band structure, there is a consequence of electrical and optical properties as described below (Polichetti et al., 2010):

Dirac cone

$$E = h v_F k$$
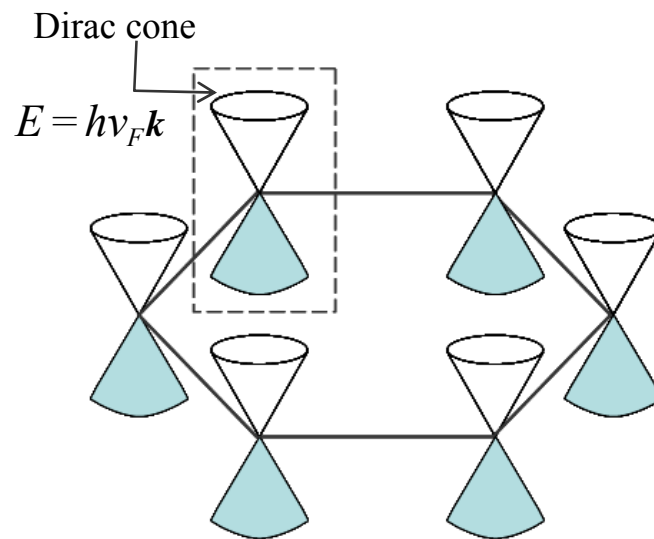
Figure 2.4 Low energy band diagram of single layer graphene at six K points.

Ambipolar Ballistic Transpot: Novoselov et al. (2004) first observed the ambipolar effect of graphene, consisting in the inversion of carrier type with the sign of applied voltage. He and his group at Manchester University measured the carrier mobility values by a multi-terminal Hall bar device using graphene flakes placed on top of an oxidized Si wafer. The results showed mobility values ranging between 3000 and 10000 cm^2/Vs, improvable up to 10^5 cm^2/Vs after an accurate control of impurities as shown in Figure 2.5 (Novoselov, Geim et al., 2005). These mobility values were also stable even at high carrier concentration ($> 10^{12}$ cm^{-2}), leading to a ballistic transport on the submicron scale (currently up to $\cong 0.3$ μm at 300 K).

(a)   (b)
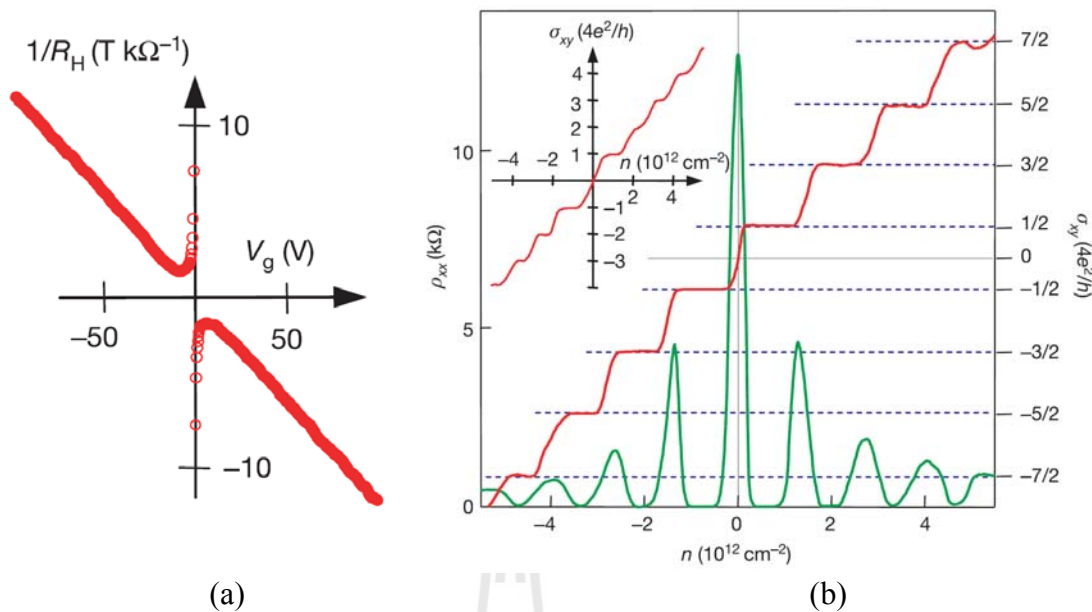
Figure 2.5   (a) Ambipolar effect: the Hall coefficient R_H, at zero gate voltage, exhibiting a sharp reversal of its sign indicating a transition between electrons and holes from the Geim paper showing how gate voltage dopes graphene p-type (as shown by the positive Hall coefficient R_H, through zero, to n-type. Both R_H and electrical conductivity σ extrapolate to zero when the Fermi level passes through the Dirac points. Interestingly, σ is actually pinned at a minimum value near $4e^2/h$, and seems not to actually go to zero. (b) the plateaus appear at half-interger filling factors for the quantum hall effect in graphene while in the inset graph is a quantum hall effect for two-layer graphene which is similar to ordinary 2D conductor at B =14 T and T = 4K. (Novoselov et al., 2005).

Anomalous Quantum Hall effect: (Zhang et al., 2005) Normally, in a magnetic field the electrons have circular cyclotron orbits ω_C= *(eB/mc)*, because when orbits are treated in quantum mechanics, they have discrete energy levels called Landau Levels (LL) which were given by Landau (1937),

$$E_n = \left(\frac{h}{2\pi}\right)\omega_C\left(n+\frac{1}{2}\right).\qquad(2.7)$$

At certain values of field, energy levels are filled up to N and there is no electron scattering as well as the conductivity σ will have discrete steps $g_s e^2/h$ where g_s is the degeneracy factor (spin and sublevels). Therefore,

$$\sigma \approx N\frac{e^2}{h}.\qquad(2.8)$$

The corresponding Hall current (J) is presented by $J_x = \sigma_{xy}E_y$ and $J_y = \sigma_{yy}E_y$. The Hall effect is the occurrence of an electric potential difference between the edges of a conducting material, crossed by an electric current, when a magnetic field is applied perpendicular to the current direction. QHE is observed in 2D conductor with high mobility and low disorder.

In classical Hall effect, ρ_{xy} depends monotonically on H and the concentration of carrier n:

$$\rho_{xy} = \frac{H}{ne}.\qquad(2.9)$$

In quantum Hall effect, ρ_{xy} is quantized as expressed by the relation

$$\rho_{xy} = \frac{2\pi\hbar}{ve^2},\qquad(2.10)$$

where v are integer or fraction numbers refer to "integral" or "fractional" quantum Hall effect.

From this QHE investigation, the material resistance expresses integer quantized values as a function of the applied magnetic field as shown in the inset graph in Figure 2.5 (b). Graphene displays this behavior even at room temperature but with the half integer of LL. Normally, LLs refer to the quantization of electron energy under a

magnetic filed. The Hall conductivity in graphene had an addition ½ term compare to ordinary 2D conductor which is given by

$$\sigma_{xy} = \frac{4\,e^2}{h}\left(N + \frac{1}{2}\right),$$ (2.11)

where σ_{xy} is the Hall conductivity. Figure 2.5 shows the plot of $1/R_H$ expressing the ambipolar behavior (a) and anomalous quantum Hall Effect (b) for graphene which displays the quantized values of the transversal conductivity σ_{xy} and longitudinal resistively ρ_{xx} as a function of their concentration at B = 14 tesla and T = 4 K. Note that the half-integer QHE is preferred in ideal graphene.

Zero Field Conductivity at zero gate voltage: Another interesting phenomenon in graphene is the existence of minimum conductivity even in the absence of charge carriers. Based on theoretical approach, when the Fermi level is pinned at the Dirac point, the carrier concentration is assumed to vanish, and hence the conductivity should be zero, the so called "minimum metallic conductivity". However for graphene, the conductance does not vanish even at temperatures as low as 4 K. From equation 2.8, graphene minimum conductivity is always equal to $4e^2/h$ (graphene is four-fold degenerate, consisting of two-spin and two valley degeneracy).

Visual Transparency and Optical Saturation: Nair et al. (2008) reported that the optical transmittance of single layer graphene was around 98 percent, and it was almost constant in all the visible photon-energy range. Despite being an atom thick, graphene can absorb a significant fraction of incident white light equal to $\pi\alpha = 2.3$ percent, so it can be visible even to a simple optical microscope investigation. α is the fine structure constant describes coupling between light and relativistic electron

which is traditionally associated with quantum electrodynamics describe by the equation

$$\alpha = \frac{e^2}{\hbar c} \approx \frac{1}{137}.$$ (2.12)

The optical absorption of graphene saturates when the input optical intensity is above a threshold value is called non-linear optical saturable absorption. This behavior is according to the zero band gap of graphene as explained by Bao et al. (2009). As shown in Figure 1.1 of Chapter I, which is the conventional optical microscope observation displays monolayer/bi-layer and multilayer graphene.

Tunable bandgap: When graphene is patterned into a narrow strip called graphene nanoribbon, the carriers are confined to a quasi-one-dimensional system, this results in band-gap opening. The energy gap dimension can be tuned during fabrication with the appropriate choice of ribbon width.

2.3 Silicon Carbide Substrate

2.3.1 Silicon carbide (SiC) structure

SiC is a wide band gap semiconductor with the gap energy varying between 2.4 and 3.3 eV depending on its polymorphs. Not only that it is hard and inert material, it also has electronic properties which are the basis for electronic device performances i.e., high breakdown field and thermal conductivity reported by Morkoc (1994) which allows high power and high frequency applications in regimes that are out of reach for Si or GaAs based deviece. SiC consists of carbon and Si covalently bound to four atoms of the other chemical species in tetrahedral coordination (Figure 2.6). The Si-C bonds are arranged in a hexagonal bilayer with carbon and silicon in different

stacking. The tetrahedral arrangement of Si-C bonds can be continued in two orientations differing by a 60° rotation. The different stacking sequence produces SiC crystals with various structures called polytypes which can be distinguished by the periodicity along the stacking. From Starke, Bernhardt, Schardt, and Heinz (1999), there are two extreme cases of the various possibilities as follows:

- **Zincblend structure (β-SiC)** is obtained with all bilayers oriented in the same direction that correspond to the cubic SiC modification. It also can be described by a planar hexagonal unit cell with a periodicity of three bilayers along the c-axis forming an ABC sequence i.e., 3C-SiC (C is denoted cubic unit cell symmetry).

- **Wursite structure (α-SiC)** is obtained when the stacking for every bilayer is rotated by 60° resulting in hexagonal structure. It has an AB sequence and is called 2H-SiC (H is denoted hexagonal unit cell symmetry).

Figure 2.7 illustrate the different stacking for the most popular substrate for electronic applications, i.e., 3C, 4H and 6H polytypes. The 4H-SiC has two bilayers of identical orientation followed by two bilayers with the opposite orientation, with an ABCB sequence, while the 6H-SiC has an ABCACB sequence and up to the third bilayer has the same sequence as the 3C-polytyes.
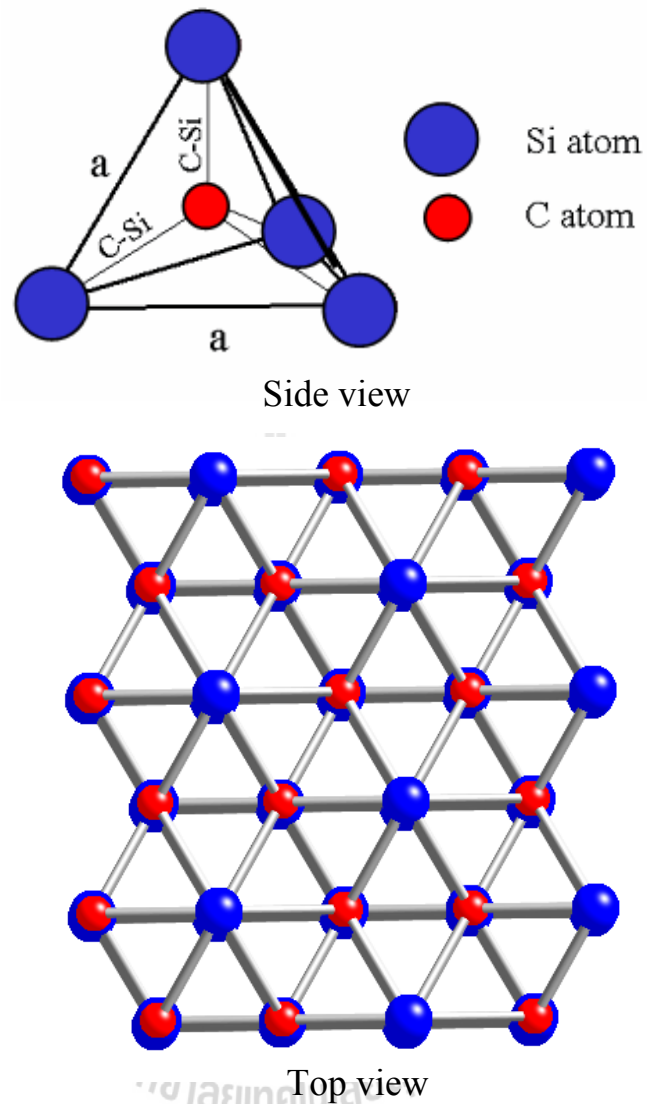
Figure 2.6 SiC crystal atom consist of one chemical species (C or Si atom) covalently bond to four other chemical species in a tetrahedral coordination.
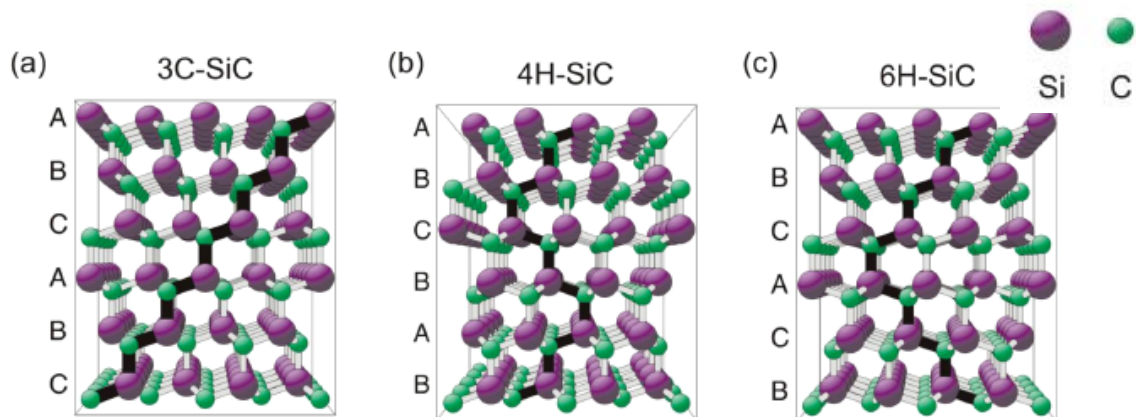
Figure 2.7   Crystal structure of SiC in the side view along $(11\bar{2}0)$ direction. (a) 3C-SiC present Zincblend structure with ABC stacking. (b) and (c) present wurtzite structure in 4H-SiC with ABCB stacking,   and 6H-SiC with ABCACB stacking, respectively. The images are adapted from Starke et al. (1999).

2.3.2 Charge transfer and surface termination in SiC

SiC has a tetrahedral structure with a convalent bond length of $1.89\,\mathring{A}$. However it also has ionic nature due to the large difference in covalent radii of Si ($r_{Si} = 1.17\,\mathring{A}$) and C ($r_C = 0.77\,\mathring{A}$) that comes from the different strength of the Si and C potentials. Charge transfer from Si to C atoms is arise the large difference of electro negativity of the Si-C elements, i. e., e_{Si} = 1.7; e_C = 2.5 ("Chapter 3 SiC(0001) cleaved surface reconstruction", www). The ionicity of SiC leading to an ionic gap, while the Si atoms act as cations and the C atoms as anions. The ionicity is taking into account the asymmetry of the charge density along the bounds. It resulted in the different in angular forces which is one of the reasons for the distinctively different reconstruction behaviors of the Si- and C- terminated surfaces. The angular forces are much larger at

the C than at Si atoms, so that changes of the tetrahedral configuration around the C
atoms involve much more energy than for Si atoms. This is also one of the reasons for
the distinguished growth mechanism in graphene form on SiC which will be described
later. The SiC surface parallel to the hexagonal bilayers is identified as the basal plane
which is the hexagonal lattice symmetry orientation. Different surface terminating
stacking sequences can be performed in Figure 2.8 for 4H-SiC. The four different
surface stacking are indicated by the depth of the bilayer orientation change, i.e. S1,
S2, S1* and S2* (S1*, S2* are identically to S1, S2 except for a 60° rotation of the
whole semi –infinite crystal).
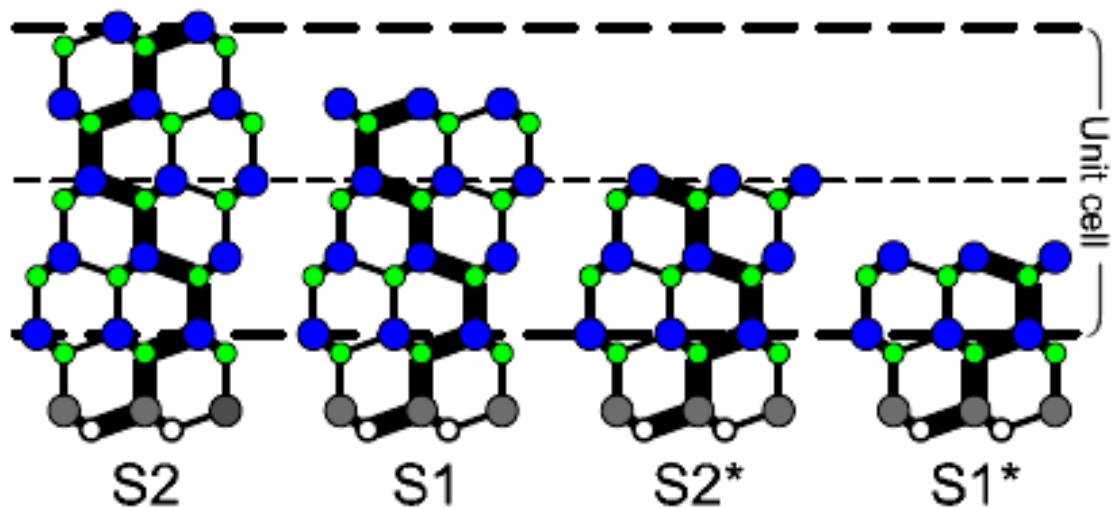
Figure 2.8   4H-SiC(0001) surface stacking possibilities. S1 and S2 indicated the
number of identically orientated bilayer directly at the surface, but rotated 60° for S1*
and S2* configurations. This stacking sequence is in the $(11\bar{2}0)$ direction plane. The
image was taken from Starke et al. (1999)

2.3.3 6H-SiC(0001) reconstruction

In this thesis, the graphene is formed on 6H-SiC(0001), so the description in this polytype of SiC is focused on in this chapter. Due to the reconstruction being strongly dependent on the surface preparation procedure and on the surface termination, a single polytype may exhibit different surface termination, depending on the postion of the topmost bilayer in the stacking sequence of the bulk unit cell. For a 6H-SiC, six different bulk truncations are distinguished by the depth of the bilayer orientation change and by the orientation of the topmost layer. It is distinguished between the two possible polarities of the 6H-SiC crystal, i.e. (0001) is denoted for Si terminated and $\left(000\overline{1}\right)$ is denoted for C terminated as illustrated in Figure 2.9. The surface reconstruction and relaxation in semiconductor is created by the breakings of bonds between atoms on the surface intodangling bonds), producing a strong increase in the surface free energy. Another driving force for surface reconstruction in SiC arises from the large difference in the lattice constants of the two elements: for C, $a_C = 3.57\overset{\circ}{A}$, and for Si, $a_{Si} = 5.43\overset{\circ}{A}$. For SiC, it has an intermediate value $a_{SiC} = 4.36\overset{\circ}{A}$. After chemical cleaning, well ordered SiC surfaces can be prepared by thermal treatment. A surface reconstruction of SiC due to the heat treatment is given in Table 2.1 as reported by Starke (1997).
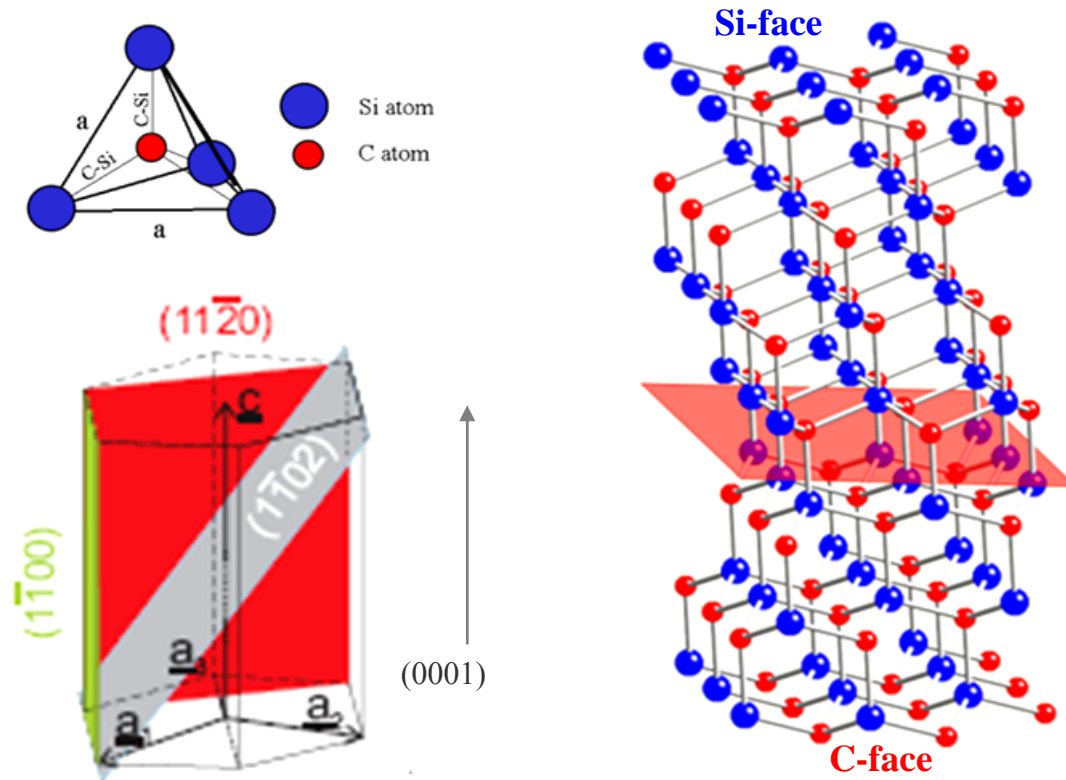
Figure 2.9 6H-SiC in both Si-terminated (Si-face) denoted by 6H-SiC(0001) and C-terminated (C-face) denoted by 6H-SiC($000\bar{1}$) stacking in the ($11\bar{2}0$) plane.

Table 2.1 Surface reconstructions due to heat treatment for both Si- and C-orientation of 6H-SiC(0001) from Starke (1997).

Method	Si-orientation (0001), (1111)	C orientation $\left(000\overline{1}\right),\left(\overline{1}\,\overline{1}\,\overline{1}\,\overline{1}\right)$	Reference
Heating	$\left(\sqrt{3}\times\sqrt{3}\right)-R30^\circ$, $\left(\sqrt{6}\times\sqrt{6}\right)-R30^\circ$, graphite	(2×2), (3×3)	Van Bommel et al. (1975)
Heating	$\left(\sqrt{3}\times\sqrt{3}\right)-R30^\circ$	(3×3)	Nakanishi et al. (1989)
Annealing in Ga flux further annealing	(3×3)	(1×1), $\left(\sqrt{3}\times\sqrt{3}\right)-R30^\circ$	Kaplan and Parrill (1986)]
Annealing in Si flux further annealing	(3×3)-$R30^\circ$ (1×1)		Kaplan (1989)
Annealing in Si flux further annealing	(3×3), $\left(\sqrt{3}\times\sqrt{3}\right)-R30^\circ$, (1×1)	(1×1), (3×3)	Bermudez (1996)
Annealing in Si flux further annealing	(3×3), $\left(\sqrt{3}\times\sqrt{3}\right)-R30^\circ$	(3×3), $\left(\sqrt{3}\times\sqrt{3}\right)-R30^\circ$	Li and Tsong (1996)
Heating	$\left(\sqrt{3}\times\sqrt{3}\right)-R30^\circ$, Mixed phased producing apparent $\left(\sqrt{6}\times\sqrt{6}\right)-R30^\circ$ LEED pattern		Owman and Martensson (1996)
Heating	Graphitic over layer with (6×6) honey comb structure		STM work. Owman and Martensson (1996)

2.4 Epitaxial growth of graphene by thermal decomposition of SiC

2.4.1 Procedures for epitaxial graphene growth on 6H-SiC(0001)

The standard procedures to synthesize epitaxial graphene from SiC by Bostwick et al. (2008) are as follows: firstly, a SiC wafer/substrate is chemically cleaned by acetone, ethanol and then etched by 5% HF (there are many procedures for the chemical cleaning process). After that the substrate is introduced to a UHV sample preparation system. The base pressure of the system is in the order of 10^{-10} Torrs or below. To removes O, the sample is annealed under Si flux at 950 °C to form the Si-rich (3×3) surface reconstruction. Then the sample temperature is increased up to 1050 °C without Si flux to obtain the $\left(\sqrt{3} \times \sqrt{3}\right)R30^{\circ}$ surface reconstruction and further to 1150 °C until the C-rich $\left(6\sqrt{3} \times 6\sqrt{3}\right)R30^{\circ}$ surface reconstruction is observed. Finally, the sample is annealed until graphene layers with the (1×1) structure of graphite forms on the surface. The surface reconstruction at each stage can be observed directly from the low energy electron diffraction (LEED) pattern as shown in Figure 2.10. Ohta et al (2006) describe the graphene growth process on SiC as follows: the first layer of graphene on SiC is designated as a buffer layer which does not exhibit graphitic properties. Therefore, the next graphene layer above this buffer layer will induce the gap. However, as the sample becomes thicker, the gap decreases rapidly and shifts from -0.4 to -0.29 to -0.2 at the 2nd, 3rd and 4th layer of graphene, respectively, as illustrated in Figure 2.11.
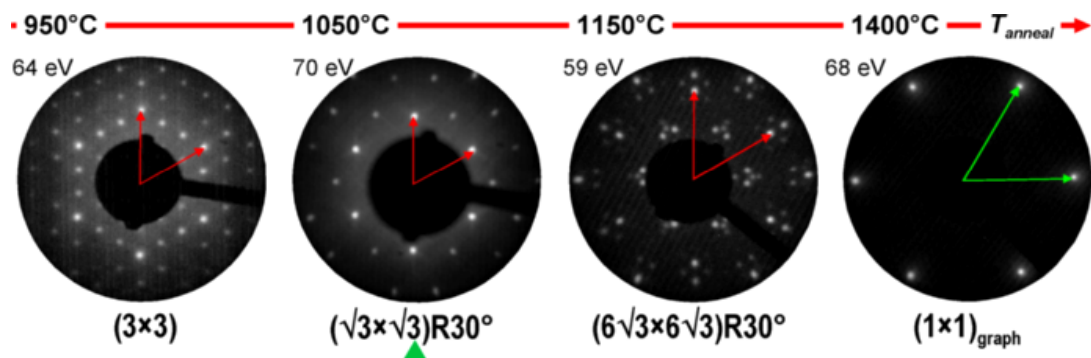
Figure 2.10 Typical LEED patterns observed during various stages of themal decomposition epitaxial graphene growth on SiC(0001) reported by Bostwick et al. (2008).
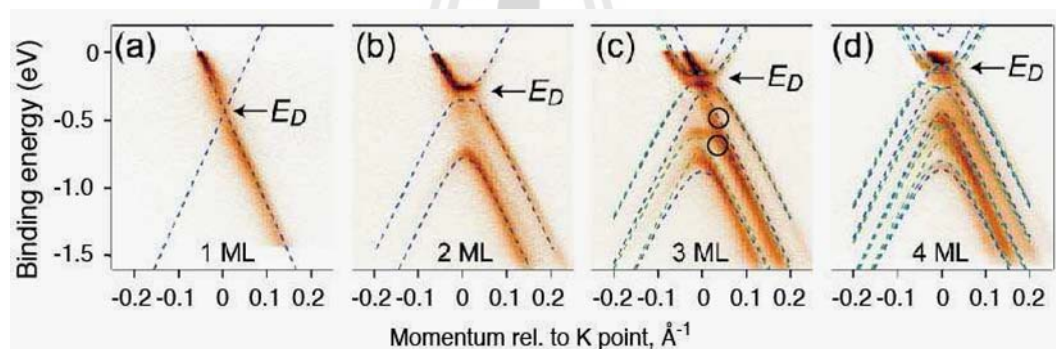
Figure 2.11 The energy band structure of epitaxial graphene with different numbers of layers on SiC from Ohta et al. (2007).

2.4.2 Graphene growth mechanism

For large-scale few layers of graphene (FLG) fabrication, the growth mechanism must be clarified because electronic properties of FLG strongly depend on its thickness. Many theoretical studies express the stable structures of SiC(0001) surface, i.e., Kageshima, Hibino, Nagase and Yamaguchi (2009). Here, the experimental study to model the growth mechanism is demonstrated. In 2008, Poon, Chen, Tok and Wee

probed epitaxial growth of graphene on SiC with *in situ* scanning tunneling microscope. From the result they proposed the growth mechanism process as demonstrated in Figure 2.12 with the description as follows:

State I: The $6\sqrt{3}$ reconstruction is the early stage to form graphene which is the C-rich layer are covalently bounded to Si-atom of the substrate below.

State II: When heating at 1200-1300 °C, Si-atoms desorb, leaving C-rich interface (reactive C* occurs).

State III: The highly reactive C* adatoms diffuse to another terrace to form new C-rich $6\sqrt{3}$ phase beneath. New $6\sqrt{3}$ interface layer is believed to provide extra stability to the graphene by buffering it from direct interaction with the underlying SiC by the psedo-van der Waals force.
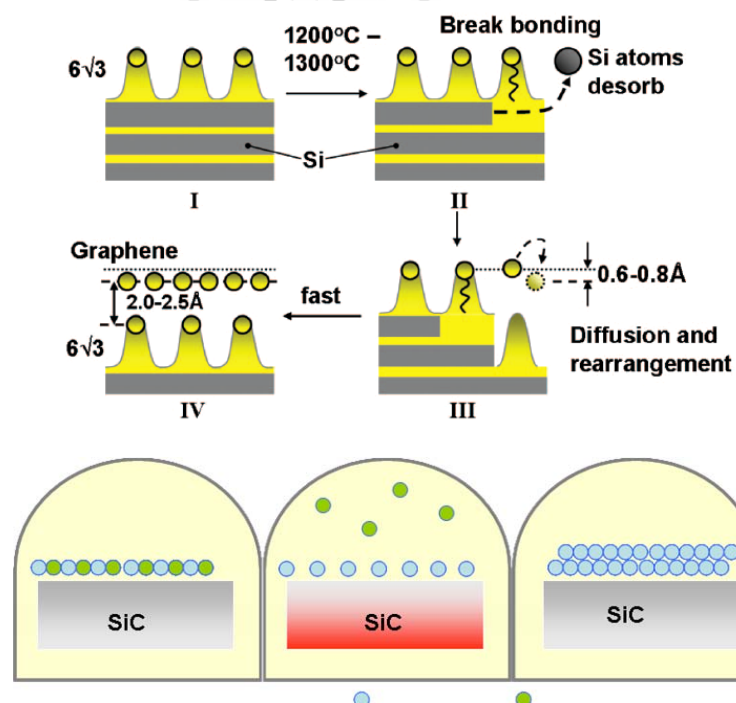
Figure 2.12 (Top) Growth mechanism model from Poon et al. (2008) and schematic illustration of thermal decomposition method (Below).

2.4.3 Evaluation of number of graphene layers

According to the fact that graphene electronic properties are thickness dependent, it is necessary to evaluate the umber of graphene layer. From an experiment in which graphene is exposed to a low-energy electron beam, and the relection of electron is detected, the number of graphene layer can determined from the quantized oscillations of the electron reflectivity as demonstrated by Hibino et al. (2008). Due to electron's wave-like properties with their wavelength determined by the kinetic energy, electrons reflected from the graphene surface and from graphene/SiC interface can interfere with each other, resulting in the electron reflectivity that changes periodically as a function of the electron energy. The oscillation period has been found to be closely related with FLG thickness (Hibino et al., 2008). Therefore, the graphene thickness can be determined from the reflectivity oscillation as shown in Figure 2.13. The simplest way to model the effect of quantum confinement on the energy of an electron is to consider it as a "particle-in-a-box" problem. For an electron inside a potential well of width l, the spacing between the lowest two quantum energy levels is: (Limit kT ≈ 25 for thermal excitations)

$$E_{QM} = \frac{3h^2}{8ml^2}.$$ (2.13)

If one require $E_{QM} > 25$ meV to prevent thermal excitations, the width of the well must be $l < 7$ nm (Petrovkh, n.d.).
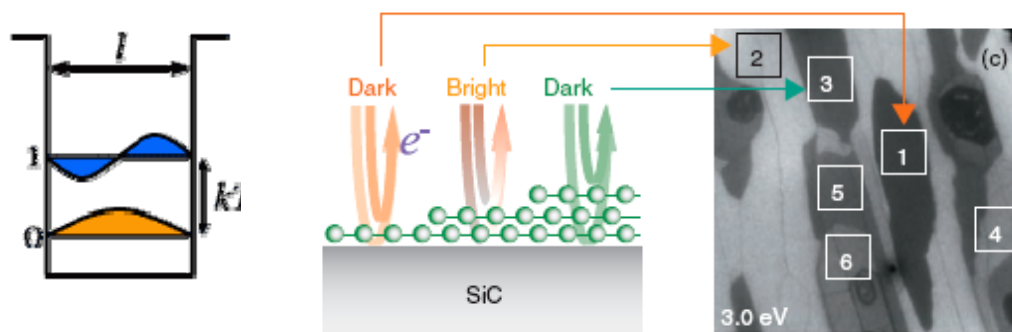
Figure 2.13 Schematic for quantum confinement of electron reflected from varying thickness distributed to the contrast mechanism in LEEM image depicted from Hibino, Kageshima and Nagase. (2010), which is based on the interference of electron in the potential well or "particle in the box".

2.5 Electron microscopy for surface science

Electron microscopy served as a surface sensitive technique owing to the small free path of electrons in the solid at certain energies. Moreover, electron can probed the whole surface Brillouin zone of materials and are easy to generate and handle.

2.5.1 Electrons in solids

Considering the scattering of an electron beam escaping from the surface of the solid. The reason provide electron based technique is very surface sensitive will be simply described. First, for elastic scattering, the energy is conserved corresponding with the equation:

$$E_s = E_0 \qquad (2.14)$$

where E_0 is the energy of the incoming electrons and E_s is for the scattered electrons. The momentum parallel to the surface is also conserved apart from a surface reciprocal lattice vector g and is expressed by

$$\mathbf{k}_{\square s} = \mathbf{k}_{\square 0} + \mathbf{g}.$$
(2.15)

Therefore, elastic scattering provides information about the surface reciprocal lattice and the surface geometry. The measurement of the crystal's **k** vectors can be done using LEED technique which will be discussed in chapter III. Secondly, only small fraction of emitted electrons can escape from the sample surface due to loss of energy as it travels through the solid. Therefore, the closer the electron is to the surface the greater the fraction of electrons is detected by the detector. This process give significant for the electron mean free path and hence surface sensitivity.

2.5.2 Electron mean free path

The superior of electrons in surface science is the electron mean free path λ (or inelastic mean free path, IMFP) which is the average distance traveled by electron through a solid as indicated by

$$\lambda(E_{kin}) = v(E_{kin})\tau = \frac{\hbar k}{m}\tau$$
(2.16)

where v is the velocity and τ is the collision time. Since, τ in the Drude model is the mean time between two scattering events whereas in a quasi-particle aspect τ is determine the lifetime of the quasi-particle. Typically, the minimum mean free path of electron is restricted to about 50-100 eV since, at lower energies the electron has insufficient energy and other scattering mechanisms will dominate such as phonons scattering. Figure 2.14 is the inelastic of electron mean free path (IMFP) in a solid as

a function of its kinetic energy. The dashed line exhibited a calculation mean free path independent of the material while the data point is the result from the experimental data of many elemental solids. The universality of this curve is that the inelastic scattering of electrons in this energy rage is generally involving excitation of conduction electrons, which is mostly the same for all elements. The IMFP in metals is corresponding only a few atomic layers, typically less than 10 Å for electron energies about 70 eV.

Figure 2.14 The inelastic mean free path of electron in solid. The dashed line is from calculation whereas the data points are from experimental data.
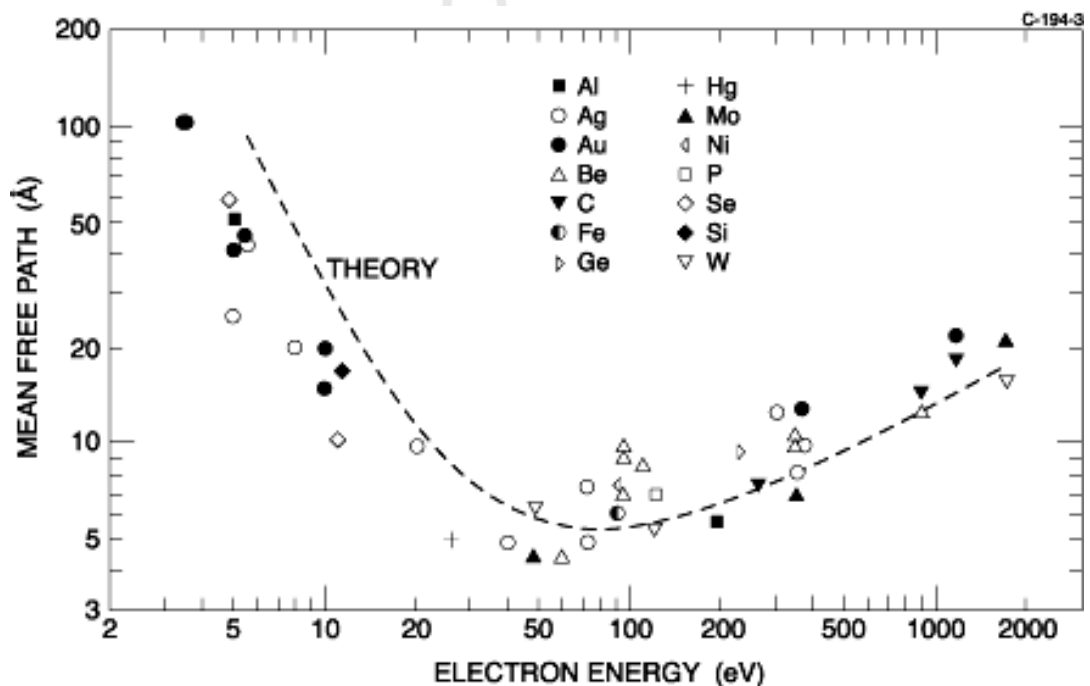
2.5.3 Electron source

Electrons are easy to produce by passing a current through a hot filament. Generally, to stimulate the thermally excited electrons, an anode was added by placing it in front of the filament. The electron beam is focused by a Wehnelt cylinder placing between the anode and the filament which is at a negative potential with respect to the filament. The basic principle of electron source or electron gun is demonstrated in Figure 2.15. The drawbacks from direct heat filament are the voltage drop over the length of the filament (0.5 V) which is also reflected in the kinetic energy of the electron, and the thermal broadening due to the high temperature needed to emit the electron.
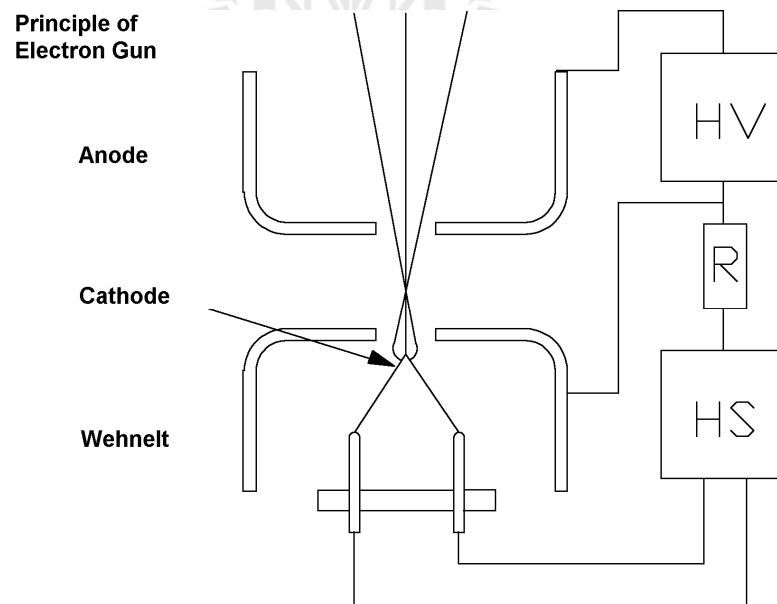
Figure 2.15 Basic principle for electron gun (Elmitech, Manual).

2.5.4 Electron analyzers

An electron beam can be detected and amplified by a channeltron, which is a glass tube coated by a resistive film inside. In principle, a high voltage is applied between the front and the end of a channeltron in order to accelerate the incoming electron to the wall where it kicks out more electron signals in order to provide measurable current pulse. The electron analyzer is designed to probe the monochromatic beam and selected energy distribution of scatter or emitter electrons, i.e., high count rates and high angular/energy resolution. The common design is cylindrical mirror analyzer (CMA) which consists of two co-axial cylinders in from of the sample. The inner cylinder is held at a positive potential while the outer cylinder is negative. Only the electron with the right energy, the so called "*pass energy'*" can pass through this set-up and be detected eventually. A disadvantage for CMA is poor resolution both in energy and angle. A better design is a hemisphere analyzer which provides higher energy resolution. As illustrated in Figure 2.16, it consists of two concentric hemispheres held a different potential in order to bias for select the desire electron energy. The additional electrostatic lens-system can be placed to focus the electron before the entrance slit and also to change the angular acceptance.
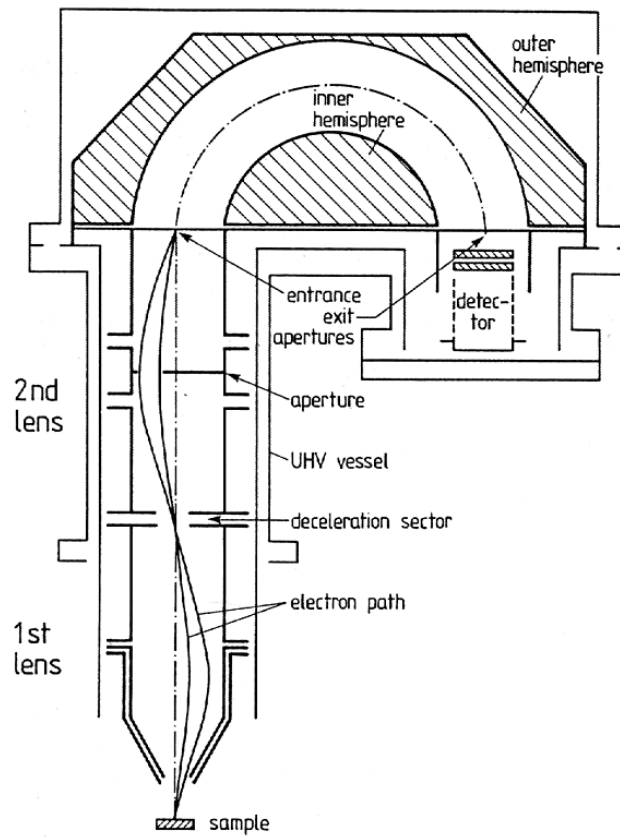
Figure 2.16 Schematics of a hemispherical electron analyzer with a focused lens system (Center for advanced friction studies, 2005).

2.6 Ultra-high vacuum

For the purpose of study about surface and thin film growth, the theoretical approach is very important in order to understand the physics of surface property and thin film growth mechanism. When referring to surface, we mean the topmost few atomic layer of the crystal about 10 $\overset{\circ}{A}$ thick. Therefore, those atomic arrangement and electronic structures differ from those in the crystal bulk. To characterize solid surface on an atomic level, the surface composition is essentially unchanged through the experiment. This requires control of the rate of gas flow environment that should be

low, or the experiment should be done in vacuum. The definition of vacuum is related to molecular density, mean free path and the time constant to form a monolayer. According to kinetic theory concept (Dushman, 1992), the arrival rate R of atoms at a surface (sometime call deposition flux, I (Oura, 2003) in a vacuum chamber is defined by

$$I = \frac{n\overline{v}}{4(unit\ area)} = \frac{p}{\left(2\pi mkT\right)^{1/2}} .$$ (2.17)

Here n is the molecular density, m is the mass of the molecule, $\overline{v}$ is the mean speed of the molecules (sometime written v, c or $\overline{c}$) and p is the pressure. Since, $\overline{v} = \left(8kT/\pi m\right)^{1/2}$ (Hudson, 1992), k_B is Boltzmann's constant and T is the temperature, thus one obtains

$$\text{Molecular density: } n = \frac{p}{k_B T} .$$ (2.18)

The mean free path between molecular collisions in the gas phase can be defined in Equation 2.19, where the proportionality constant f was solved by Maxell in 1860 (Garber, 1986),

$$\text{Mean free path: } \lambda = \frac{f}{n\sigma^2} .$$ (2.19)

Therefore, at low pressure $n = Ap$ with n per cm^3 and p in mbar, thus the constant $A = (100)/(k_B T \times 10^6)$. This gives $n = p/k_B T = 7.2464 \times 10^{18}/T$ (Altman, 2005). For example of CO at room temperature ($25\,C^{\circ}$) with the pressure in the range of 10^{-6} mbar, there are the molecule density in the range of 2.42×10^{10} molecule/cm³. As there are lots of molecules even in vacuum, the UHV (Ultra-High Vacuum, below 10^{-9} mbar) condition is appropriate for surface science experiments, since at this range

of UHV pressure the gas molecules (mean free path) will travel from wall to wall of the UHV chamber without intermediate collisions. Table 2.2 is the example case of nitrogen molecule at room temperature (T = 293 K) to illustrate how their values vary with the pressure. It is remarkable that a time constant to form a monolayer as shown in Table 2.2 express that why doing experiment in UHV conditions is necessary because only low pressure can maintain a clean surface long enough to do the experiment related τ is greater than 1 hour for $p < 10^{-9}$ mbar.

$$\text{Time constant to form a monolayer: } \tau = \frac{n_0}{I} = \frac{n_0\sqrt{2\pi m k_B T}}{p} \qquad (2.20)$$

where σ^2 denotes the molecular cross-section and n_0 is is the number of atoms in a monolayer. There are several units used for measuring vacuum pressure. The conversion from the most common unit, Torr (or millimeters of mercury, mmHg) and others units, i.e., Pascal (SI unit, 1 Pa = 1N/m^2) and mbar (1 mbar = 100 Pa) is

$$
\begin{aligned}
1 \text{ mbar} &= 100 && \text{Pa,} \\
1 \text{ mbar} &= 1 && \text{Torr} \\
1 \text{ Pa} &= 7.5 \times 10^{-3} && \text{Torr,} \\
1 \text{ Torr} &= 1.33 && \text{mbar,} \\
&= 133 && \text{Pa.}
\end{aligned}
$$

Table 2.2 Molecular density n, arrival rate I, mean free path λ, and the time constant τ, to form a monolayer for N_2 at room temperature by assumed the sticking coefficient to be unity. Defined the density of one monatomic layer $n_0 = 10^{15}$ cm^{-2}. (Oura, 2003)

Pressure (Torr)	Molecular density, n (cm^{-3})	Arrival rate I (cm^{-2}s^{-1})	Mean free path, λ	Monolayer arrival time, τ
760	2×10^{19}	3×10^{23}	700 Å	3 ns
1	3×10^{16}	4×10^{20}	50 μm	2 μs
10^{-3}	3×10^{13}	4×10^{17}	5 cm	2 ms
10^{-6}	3×10^{10}	4×10^{14}	50 m	2 s
10^{-9}	3×10^{7}	4×10^{11}	50 km	1 hour

2.7 References

Bostwick, A., Emtsev, K. V, Horn, K., Huwald, E., Ley, L., McChesney, J. L., Ohtta, T., Riley, J., Rotenberg, E., Speck, E. F. and Seyller, Th. (2008). Photoemission studies of graphene on SiC: Growth, Interface, and Electronic Structrue. **Adv. in Solid State Phys.** 47: 159-170.

Center for advanced friction studies (2005). **Surfaces and contact mechanics**. [On-line]. Available: http://frictioncenter.engr.siu.edu/course/coursematerial.html.

Dresselhaus, M. S. and Dresselhaus, G. (2002). Review: Intercalation compounds of graphite. **Adv. Phys.** 51(1): 1-186.

Elmitec Elekronenmikroskopie. **Manual upgrade LEEM for a PEEM III with imaging energy analyzer**.

Geim, A. K. and Novoselov, K. S. (2007). The rise of graphene. **Nature Mater.** 6: 183-191.

Giovanetti, G. Khomyakov, P. A., Brocks, G., Karpan, V. M., Brink, J. and Kelly, P. J. (2008). **Phys. Rev. Lett.** 101: 026803 1-4.

Hibino, H., Kageshima, H. and Nagase, M. (2010). **Graphene Growth on Silicon Carbide**. Special Feature: Front-line Materials Research 8(8): Atsugi-shi, Japan: NTT Technical review.

Hibino, H., Kageshima, H., Maeda, F., Nagase, M., Kobayashi, Y. and Yamaguchi, H. (2008). Microscopic Thickness Determination of Thin Graphite Films Formed on SiC from Quantized Oscillation in Reflectivity of Low-energy Electrons. **Phys. Rev. B** 77: 075413-075425.

Kageshima, H., Hibino, H., Nagase, M. and Yamaguchi, H. (2009). Theoretical Study of Epitaxial Graphene Growth on SiC(0001) Surfaces. **Appl. Phys. Exp.** 2: 065502-1-3.

Kaplan, R. (1989). Surface structure and composition of β- and 6H-SiC. **Surf. Sci.** 215: 111-134.

Kaplan, R. and Parrill, T. M. (1986). Reduction of SiC surface oxides by a Ga molecular beam: LEED and electron spectroscopy studies. **Surf. Sci. Lett.** 165: L45-L52.

Latil, S. and Henrard, L. (2006). Charge Carriers in Few-Layer Graphene Films. **Phys. Rev. Lett.** 97: 036803-036805.

Mårtensson, P., Owman, F. and Johansson, L. I. (1989). Morphology, Atomic and Electronic Structure of 6H-SiC(0001) **Surf. Phys. Stat. Sol (b)** 202: 501-528.

Nakada, K., Fujita, M., Dresselhaus, G. and Dresselhaus, M. S. (1996). Edge state in graphene ribbons: Nanometer size effect and edge shape dependence. **Phys. Rev. B** 54: 17954-17961.

Nakanishi, S., Tokutaka, H. Nishimori, K., Kishida, S. and Ishihara, N. (1989). The difference between 6H-SiC(0001) and (0001) faces observed by AES, LEED and ESCA. **Appl. Surf. Sci.** 41/42 :44-48.

Noveselov, K., Geim, A., Castro neto, A. H., Gulinea, F. and Peres, N. M. R. (2009). The electronic properties of graphene: **Rev. Mod. Phys.** 81: 109-162.

Ohta, T., Bostwick, A., Seyller, T., Horn, K. And Rotenbergy, E. (2006). Controlling the electronic structure of bilayer graphene. **Science** 313: 951-954.

Owman, F. and Martensson, P. (1996). Scanning tunneling microscopy study of SiC(0001) surface reconstructions. **J. Vacuum Sci. Technol. B** 14 : 933-937.

Owman, F. and Martensson, P. (1996). The SiC(0001)$6\sqrt{3}\times6\sqrt{3}$ reconstruction studied with STM and LEED. **Surf. Sci.** 369: 126-136.

Poon, S. W., Chen, W., Tok., E. S. and Wee, A. T. S. (2008). Probing epitaxail growth of graphene on silicon carbide by metal decoration. **Appl. Phys. Lett.** 92: 104102-104104.

Reich, S., Maultzsch, J., Thomsen, C. and Ordejón, P. (2002). Tight-binding description of graphene. **Phys. Rev. B** 66: 035412-035412-5.

Riedl, C., Coletti, C. and Starke, U. (2010). Structural and electronic properties of epitaxial graphene on SiC(0001): a review of growth, characterization, transfer doping and hydrogen intercalation. **J. Phys. D: Appl. Phys.** 43: 374009.

Saito, R., Fujita, M., Dresselhaus, G. and Dresselhaus, M. S. (1992) . Electronic structure of graphene tubules based on C60. **Phys. Rev. B** 46: 1804-1811.

Saito, R., Dresselhaus, G. and Dresselhaus, M. S. (1999). **Physical Properties of Carbon Nanotubes** (2nd ed.). Imperial, London.

Shallcross, S., Sharma, S. and Pankratov, O. (2008). Quantum interference at the twist boundary in graphene. **Phys. Rev. Lett.** 101: 056803 1-4.

Starke, U. (1997). Atomic structure of Hexagonal SiC Surface, **Phys. Stat. Sol. (B)**. Applied Research. 202: 475-499.

Starke, U., Bernhardt, J., Schardt, J. and Heinz, K. (1999). SiC surface reconstruction: releavacy ofof atomic structure for growth technology. **Surf. Rev. Lett.** 6: 1129-1141.

Starke, U., Bram, Ch., Steiner, P.-R. Hartner, H., Hammer, L., Heinz, K. And Muller, K. (1995). The (0001) surface of 6H-SiC: morphology, composition and structure. **Appl. Surf. Sci.** 89: 175-185.

Van Bommel, A. J., Crombeen, J. E. and Van Tooren, A. (1975). LEED and Auger electron observations of the SiC(0001) surface. **Surf. Sci.** 48: 463-472.

Wallace P. R. (1947). The Band Theory of Graphite. **Phys. Rev.** 71(9): 622-634.

Zhang, Y., Tang, T.-Ta., Girit, C., Hao, Z. Martin, M. C., Zettl, A., Crommie, M. F. Shen, Y. R. and Wang, F. (2009). Direct observation of a widely tunable bandgap in bilayer graphene. **Nature** 459: 820-823.

CHAPTER III

EXPERIMENTAL TECHNIQUES

In this chapter, the experimental procedures and measurement techniques employed during the course of this thesis work are described. This work was carried at the BL3.2b beamline of the Synchrotron Light Research Institute (SLRI). The main instrument of this beamline is the Elmitec LEEM III system. The system was used for both synthesization and characterization of graphene. In this work, graphene was synthesized by thermal decomposition of a SiC single crystal. LEEM and LEED (low-energy electron diffraction) measurement techniques were employed with an electron gun equipped with the LEEM system. By using synchrotron light as the excitation, the microscope can be used for PEEM (photoemission electron microscopy). The combination of LEEM and the ability to select any photon energy of synchrotron light allows that X-ray absorption spectroscopy (XAS) can be performed with sub-micron spatial resolution. The above-mentioned measurement techniques were carried out in situ, in the LEEM system. Ex situ measurements using photoemission spectroscopy (PES) were also attempted at the PES experimental station of the BL3.2a beamline.

3.1 Preparation of SiC substrate

Graphene was synthesized from SiC single crystal samples by thermal decomposition. One-side polished *n*-type doped 6H-SiC (0001) samples were supplied by the MTI Corporation. The surface of the substrate is parallel to the (0001)

crystallographic plane. The dimension of the substrate is $5\times5\times0.3$ mm^3. The procedures for surface treatment before thermal decomposition maybe summarized as the followings:

- The samples were first chemically cleaned in the mixture of NH4OH, H_2O_2, and de-ionized water with a ratio of 1:1:5 as well as heated at 70 °C for 10 minutes;

- Then, the samples were chemically etched by dipping in the 5% HF acid.

- The last chemical cleaning process was by leaving the samples in the mixture of HCL, H_2O_2, and de-ionized water with a ratio of 1:1:5 at 70 °C for 10 minutes;

- Surface topography of some samples was studied by using an atomic force microscope (AFM) after chemical cleaning processes;

- After that the samples were introduced into the load-lock chamber of the LEEM-PEEM experimental station of BL3.2b. The samples were then degassed in the load-lock chamber;

- After sample transfer to the LEEM system, further degassed at elevated temperature in the LEEM system was also essential.

Thermal decomposition of the SiC samples was carried out in the LEEM system. Heating of the samples was by using an electron-electron beam bombardment. heating system. The heating system of LEEM allows the temperature of the sample to be raised up to approximately 1700 °C maximum. The advantage of this sample preparation was that the surface reconstruction of SiC leading to the formation of the graphene could be followed in situ by observing LEED patterns in the LEEM system.

More importantly, the number of graphene can easily be deduced from the "Intensity versus Bias Voltage of the Sample", or I-V LEEM curve, as demonstrated by Hibino, Kageshima, Maeda, Nagase, Kobayashi and Yamaguchi (2008).

3.2 Atomic Force Microscopy (AFM)
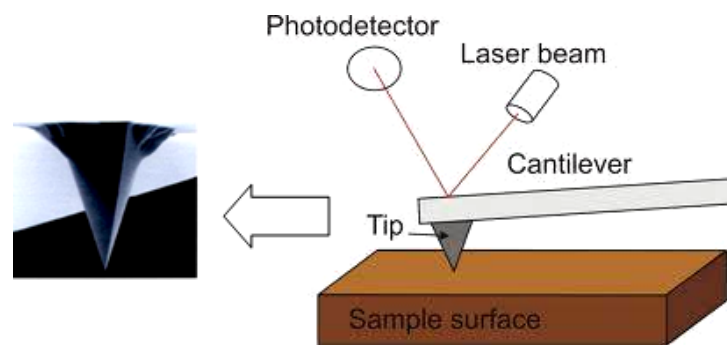
Figure 3.1   Schematic of AFM component and the shape of the tip.

In this work, AFM was used to study the surface topography of the SiC substrate before the thermal decomposition process. AFM is a very useful and powerful technique for studying surface topography and very easy to operate since the measurements can be carried out in ambient condition for both insulating and conducting surface. The schematic diagram of AFM is given in Figure 3.1. It shows the main components of AFM, i.e. the cantilever, the laser source and the photodetector (Hubbard, 1995). The principle of AFM is based on the measurement of the force applied between the tip and the sample surface held in close proximity to each other. The spring displacement of the cantilever is proportional to the force and is governed by the Hooke's law

$$F = -kx, \tag{3.1}$$

where F is the force, k is the spring constant and x is the spring displacement. The

distance between the tip and the surface atom is crucial in determining the mode of

operation of AFM. As the matter of fact, the nature and the magnitude of the force

between the tip and the surface, and thus the AFM modes of operation, between the

tip and the surface are governed by the interatomic potential as illustrated in Figure

3.2. The three different modes of operations of AFM are described below.
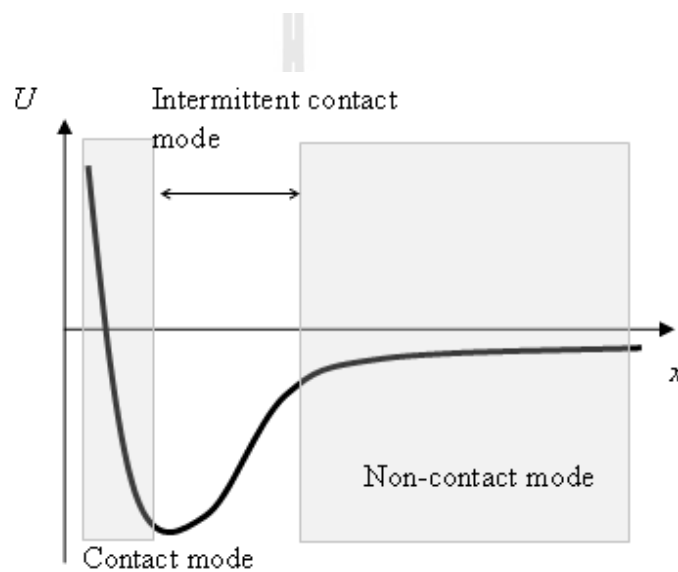
Figure 3.2   Surface force in the regime of tip-sample interaction or AFM mode.

   (1) Non-contact AFM mode: In this operational mode, the tip does not contact

the sample surface. Typical distance between the tip and the surface is in the range

10-100 $\overset{\circ}{A}$, this is the range where van der Waals forces are the strongest. This mode

is good for soft or elastic surface since the measurement will cause least

contamination and least destructive on the sample surface. The forces measured are

very weak, typically in the range of $\sim 10^{-12}$ N. Such small forces are difficult to

measure, thus the measurement is in dynamic mode by oscillating the cantilever at a

frequency slightly above its resonant frequency where the amplitude of the oscillation

is a few tens $\overset{\circ}{A}$. The resonant frequency of the cantilever is reduced by van der Waals

force. The resonant frequency is given by

$$f = \frac{1}{2\pi}\sqrt{\frac{k}{m}} \; . \tag{3.2}$$

where k varies with external force gradient (*dF(x)/dx*) and the resonant frequency

changes with external force. The feedback system is used in a combination with the

reduction of the resonant frequency of the cantilever to maintain a constant frequency

or amplitude. Construction of a topographical image of the sample surface can be

obtained by measuring the tip-to-surface distance at each (x,y) data point.

    (2) Contact Mode: In this mode of operation, the deflection of the cantilever is

used as a feedback signal. The spring constant of cantilever is, thus, less than surface

force so that the cantilever is bended when the tip is experienced with the overall

repulsive force as illustrated in Figure 3.3. If the spring constant of the cantilever were

greater than surface force, the surface or the tip would be mechanically damaged. The

deflection of the tip is normally measured by 'beam bounce' method as show in

Figure 3.4, or use of piezoelectric cantilever (resistance change with deformation).

There are two modes of operation, i.e.

        (a)   *Constant force mode*: In this mode of operation, the piezoelectric

                cantilever moves sample in z direction in order to keep a constant tip

                deflection. This method provides accurate topography, but takes time

                (slow) which is limited by the time constant of the cantilever.

(b)   *Constant height mode*: In this mode of operation, the piezoelectric cantilever will keep z-piezo fixed and deflection of the cantilever is directly measured. This mode provides fast measurement, but it limits only to rather flat sample.
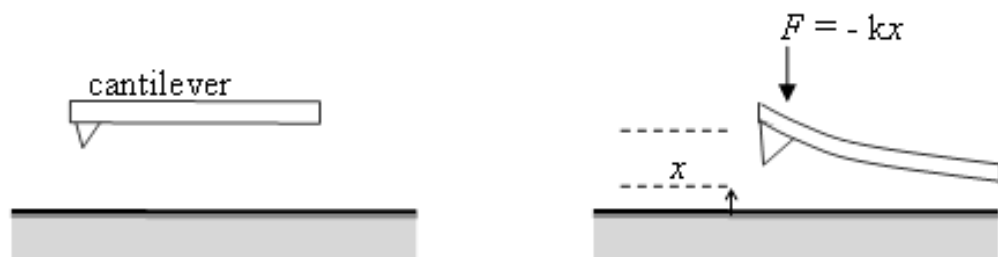
Figure 3.3   The cantilever bends in contact mode due to the spring constant of the cantilever being less than the surface force.
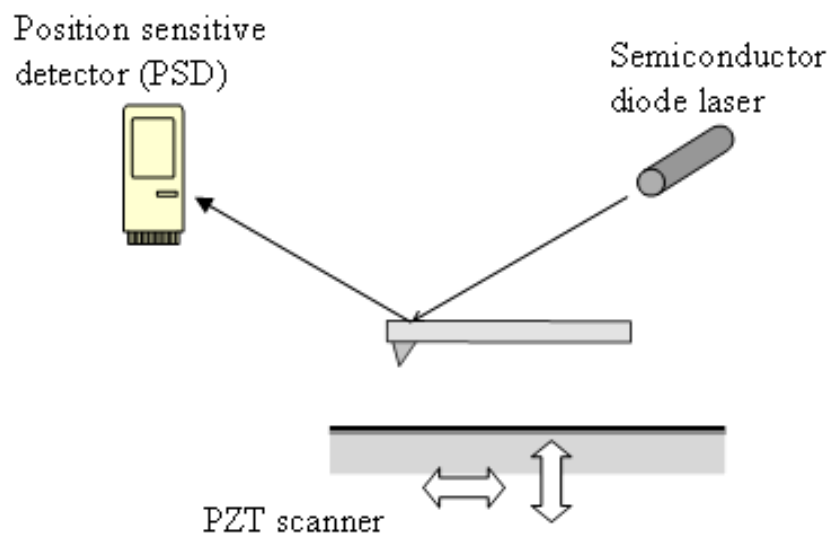
Figure 3.4   Beam bounce method to measure the deflecting of the tip.

(3) Intermittent contact or tapping mode: This mode of operation was invented to enhance the detection sensitivity. The tip is kept close enough to detect the close-range force while the tip is prevented to stick tip the surface. This mode of operation is sometime called "AC Mode". The above technical requirements can be achieved by oscillating the cantilever near its resonant frequency the same way as in the non-contact mode. However, the amplitude of the oscillation is greater than 100 $\overset{\circ}{A}$.

It should be noted that AFM measurements performed during the course of this thesis work were carried out at the Kasetsart University, Bangkok, using the Asylum Research MFP-3D-Bio AFM.

3.3 Synchrotron light beamline: BL3.2

Synchrotron light is the radiation emitted from a relativistic charge particle travelling in a curved motion. Note that an electron will be referred to, instead of a charged particle, since nearly all synchrotron light sources use electrons. Due to its unique properties, synchrotron light is an essential probe for investigation of various materials at the atomic and molecular scales. The unique properties of synchrotron light may be summarized as the followings (Winick, 1994):

Continuous spectrum and tunability: The spectrum of synchrotron light from bending magnet and wiggler is continuous. The spectrum covers from infrared to X-rays, depending on the electron energy and the magnetic field. Undulator light exhibits a strong interference peak at certain photon energies. However, the position of the peak can be adjusted by changing the gap of the undulator, therefore the synchrotron light becomes a tunable light source.

Low emittance and high collimation: Synchrotron light is emitted from a bunch of electrons in the electron beam. The beam size and the properties of the electron bunch are well controlled. The electron beam in modern light source can now be controlled down to micron size with low emittance, and thus becomes a very small light source with low emittance producing synchrotron light with a small beam size and high collimation.

High flux and high brilliance: The photon flux of synchrotron light is very high and many order of magnitudes compared with conventional X-ray source. Due to its' very small beam size and very low divergence, the brightness or brilliance is greatly enhanced.

Polarization: The synchrotron light from a bending magnet has linear polarization only in the plane of the storage ring. Light emitted off this plane is elliptically polarized. Polarization of the light may be used for studying dichrois properties of materials.

Pulse Light: Synchrotron light has a pulse structure since the electron beam also has pulse structure arising from the nature of rf acceleration. This property may be used for dynamics study of materials.

3.3.1　The Siam Photon Source: Source of BL3.2
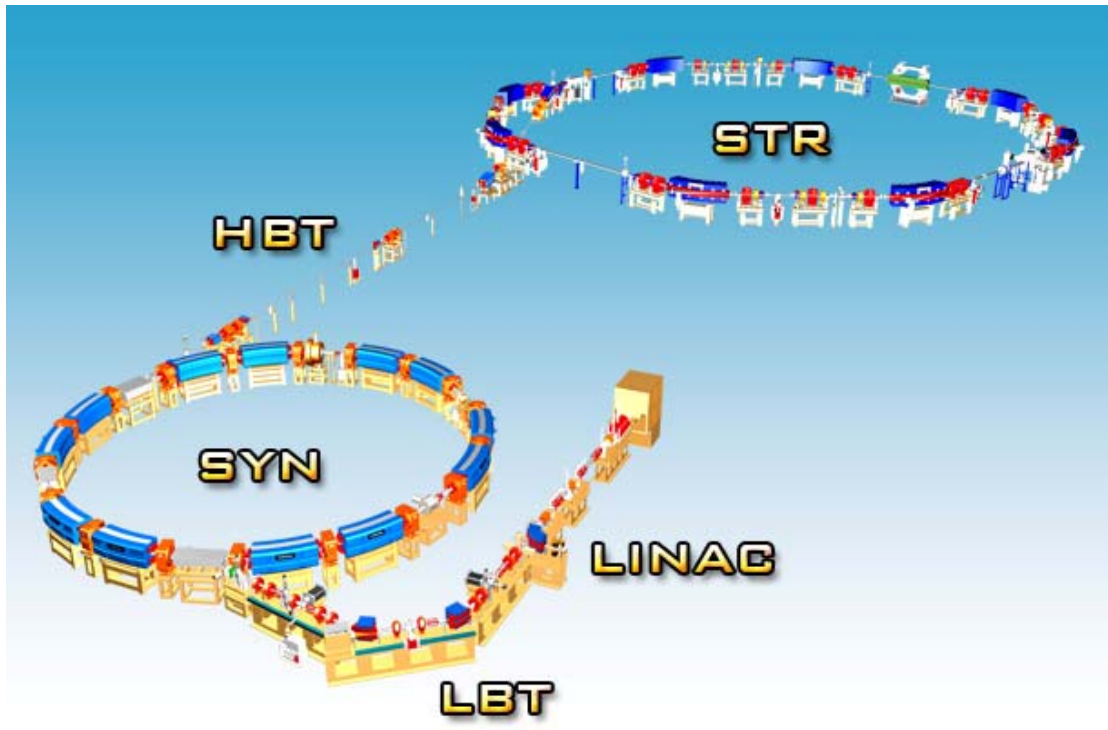
Figure 3.5　The Siam Photon Source of SLRI, Nakhon-ratchasima, Thailand (SLRI, 2012).

The Siam Photon Source is the first and only synchrotron light source of Thailand. The Siam Photon Source consists of a 40 MeV electron linear accelerator (LINAC), a 1 GeV booster synchrotron and a 1.2 GeV storage ring (STR), as illustrated in Figure 3.5. The characteristic of synchrotron light is governed by the beam properties in the storage ring. The ring consists of a magnetic lattice with four-fold structure. There are totally bending magnets. Four long straight sections provides space for installing insertion devices. A planar undulator (U60), which is the source for BL3.2, is installed upstream of the BM3 bending magnet. The parameters of U60 are given in Table 3.1. The spectra of synchrotron light produced from U60 are shown in Figure

3.6 in comparison with light generated from the bending magnet and the 6.4 Tesla wavelength shifter.
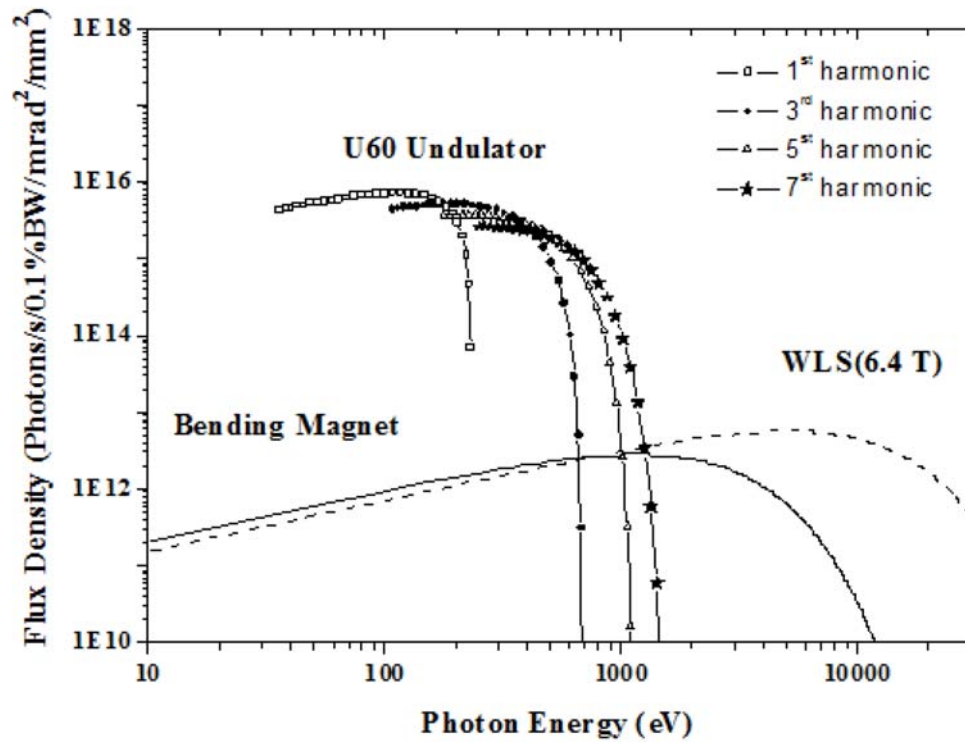
Figure 3.6 Calculated spectra of synchrotron light of SPS generated from Bending Magnet of the storage ring, the U60 planar undulator and the 6.4 tesla superconducting magnet wavelength shifter (Tong-on, 2010).

Table 3.1   The main parameters of the U60 undulator.

Parameter	Data
Configuration	Pure Permanent Magnet (PPM) symmetric
Magnet material	VACODUM
Period length (λ_u)	60 mm
Minimum & maximum gap	26 & ≥ 200 mm
Operated minimum & maximum gap	26.5 & 100 mm
Total length of magnetic assemblies (L)	2510 mm
Number of full size poles	81
Number of periods (N)	41
Peak magnetic field (B_0)	0.54674 T
Peak magnetic field strength (K)	3.06306
Minimum photon energy (Gap 26.5 mm, Electron beam 1.2 Gev)	~ 40 eV

3.3.2   Optical layout of BL3.2

Optical layout of BL3.2 is in Figure 3.7. The optical beamline consists of a focusing mirror (M0), a monochromator and two post-focusing mirror systems. The beamline employs a varied line-spacing plane grating (VLSPG) monochromator with two constant included angles (167.5° and 172.5°). There are three gratings with the groove density at the center of grating N_o = 600, 1200 and 2400 lines/mm. The

beamline delivers light generated from the U60 undulator with photon energy between 40-160 eV and 220-1040 eV.

The focusing mirror M0 is a toroidal mirror. In the dispersive plane, light is focused by M0 onto the entrance slit of the VLSPG monochromator. The included angle of the monochromator is selected by selecting either M1/1 or M1/2 for the high or low photon energy range, respectively. Grating with $N_o = 600$ is used for the low photon energy region while the other two are for the high photon energy region. Downstream of the monochromator, there are two branchlines operating in a time sharing mode, i.e. BL3.2a and BL3.2b. BL3.2a is dedicated for photoemission spectroscopy while BL3.2b is designed for photoemission electron microscopy. Figure 3.8 is the photon flux measurement at sample position in XPS station of BL3.2a compare with the simulation results.
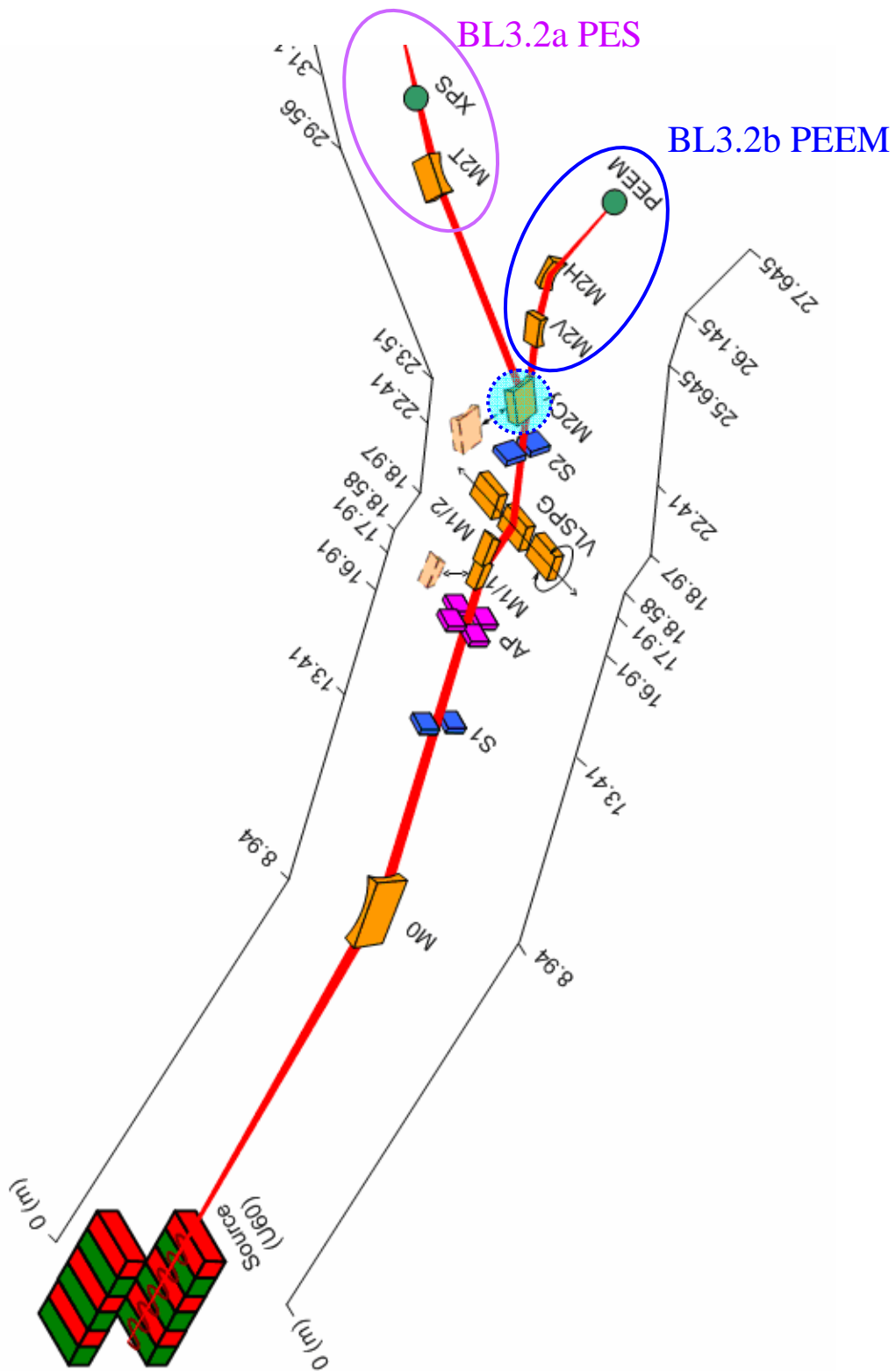
Figure 3.7 The BL3 optical element layout. The M2Cy is used for selecting between the PES and PEEM branchlines.
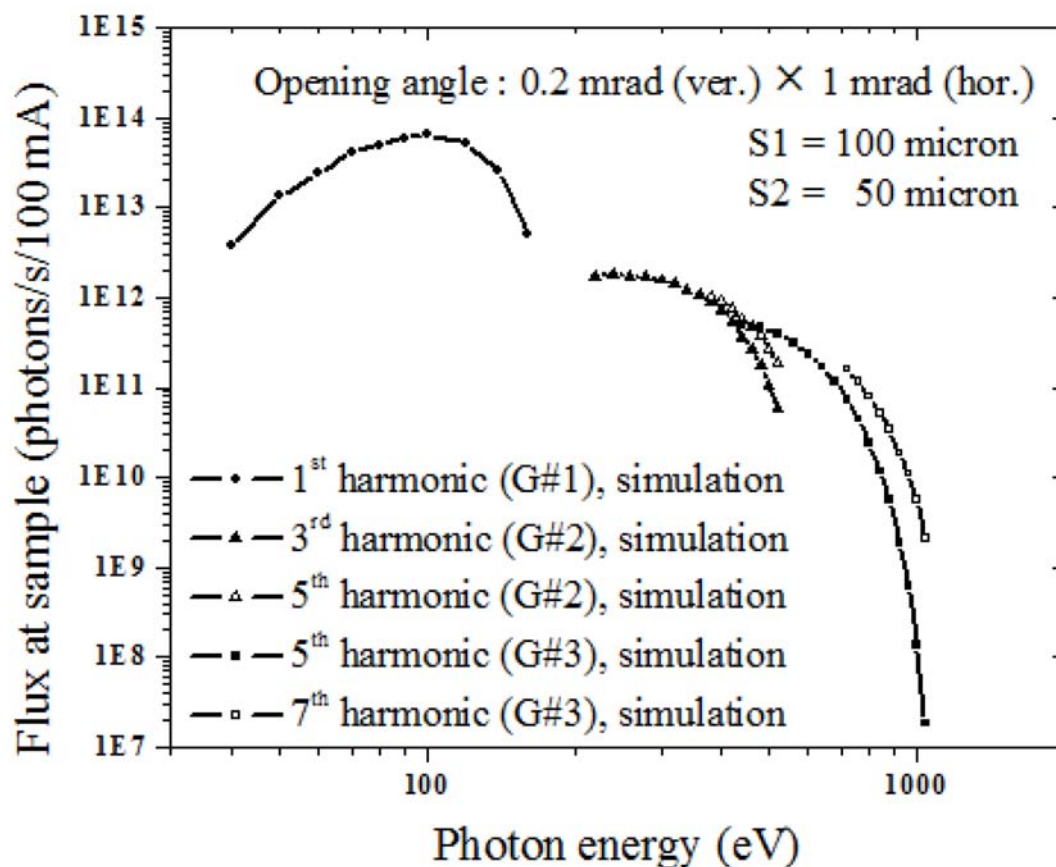
Figure 3.8 The measured and simulated photon flux at the sample position of BL3.2 (Tong-on, 2010).

3.3.3 Experimental stations of BL3.2

As mentioned above, BL3.2 has two branchlines. The BL3.2a branchline is designed for photoemission spectroscopic experiments and (soft) X-ray absorption spectroscopy (XAS). The experimental station of BL3.2a is schematically shown in Figure 3.9. There are four experimental chambers. Two small chambers are dedicated for XAS in electron-yield mode. The main chamber (ARPES) is for angle-resolved and angle-integrated photoemission spectroscopy for surface and interface science research. There is also a dedicated photoemission spectroscopy dedicated for general

chemical analysis, knows as XPS. The advantage of this experimental station is that there are simple transfer systems allowing samples to be transferred from the preparation chamber to the ARPES system without exposing to air.
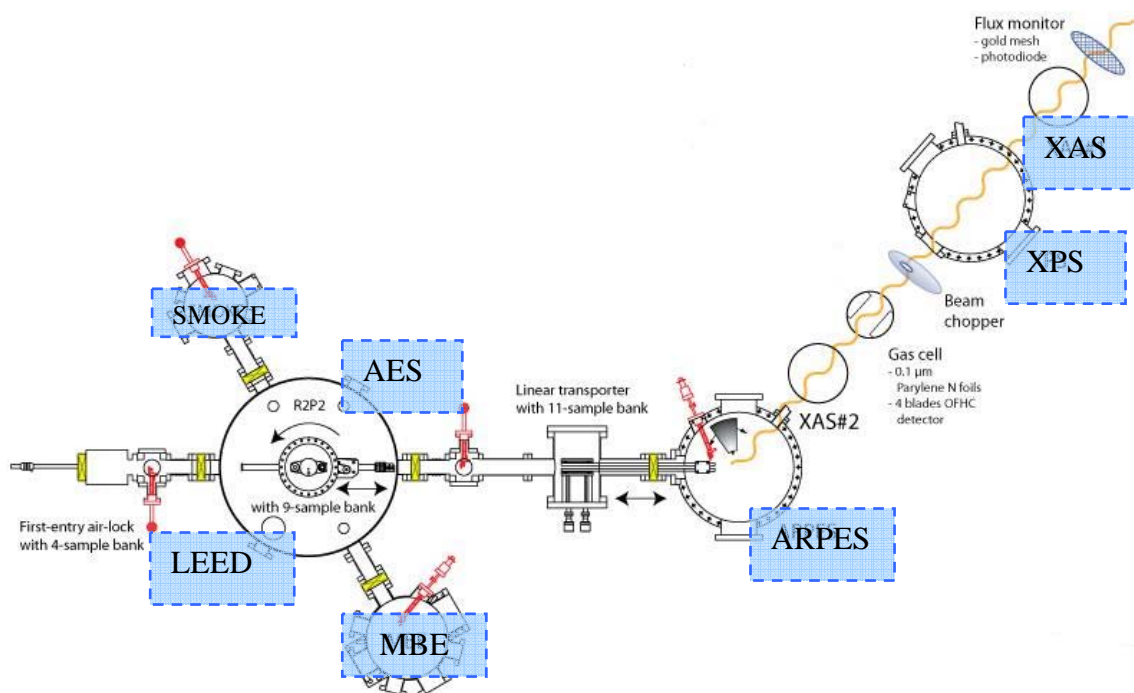
Figure 3.9 The schematic diagram of the experimental station of BL3.2a.

The design and construction of the experimental station of BL3.2b is part of this thesis work. It is for PEEM, as well as LEEM, experiments. The principles of LEEM and PEEM will be given in a separate section.

3.4 Low Energy Electron Microscopy (LEEM) and Photo Emission
Electron Microscopy (PEEM)

3.4.1 Basic principle of LEEM

LEEM is basically an electron microscopic technique. The main difference from other electron microscopes such as SEM (scanning electron microscopy) and TEM (transmission electron microscopy) is the origin and characteristic of electrons, resulting in a difference in electron optics. LEEM was first successfully demonstrated in 1985 by Bauer and Telieps. The main goal for the development of LEEM was to observe nano-scale processes on surfaces in real-time surface dynamics at nanometer scale i.e. adsorption, phase transition, chemical reactions, thin film growth etc., as described by Heun, Schmidt, Ressel, Bauer and Prince (1999), Heun and Salviati (2000). LEEM technique has some limitations for uses in characterization of materials. The limitation is that the specimen must be a conducting material, and its surface must be flat relative to the required spatial resolution. Typically, the electron energy used in LEEM is much lower, compared with 5-40 keV for SEM. Not only the electron analyzer equipped with LEEM, but also another dominant part of LEEM that differs from other conventional electron microscopes is the cathode lens which is used as the objective lens (resulting in the specimen being one of the electrodes). LEEM is usually combined with the LEED technique, since both use electron gun as a source, to provides a superior tool for surface studies. A more advanced LEEM system consist of several electron optical components and can only be found in synchrotron research facilities. Such a LEEM system is equipped with an imaging energy analyzer to provide imaging spectroscopic mode of measurement (LEEM III). Thus the

principle of operation for LEEM given below will refer to this type of the LEEM III system.

3.4.2 Basic principle of PEEM

Kordesch (2006) had given an explanation about Photoemission microscopy and Photoelectron emission microscopy as follows: i) Photoemission microscopy is a high-contrast method used in surface science because of its versatility and surface selectivity, ii) the photoelectron emission microscope (PEEM) is a microscope type that uses photons for illumination; it is a direct or "parallel" imaging technique, and it uses a cathode lens as part of the microscope objective lens. At synchrotron research facilities, LEEM systems are attached to a synchrotron light beamline. Thus, the LEEM system may be used in (imaging) PEEM mode of measurement. In this mode, synchrotron light, instead of low energy electrons, is used to excite atoms in the sample to emit electrons, called photoelectrons which described by photoelectric effect. The photoelectron emitted from surface with the maximum kinetic energy given by

$$E_{kin} = h\nu - E_b - \phi_{sample}, \tag{3.3}$$

where $h\nu$ is the photon energy, E_b is the binding energy of the electron and ϕ_{sample} is the sample work function. However, this process is measured inside the analyzer as demonstrated in Figure 3.10, so the kinetic energy of the electron in the analyzer ($E_{analyzer}^{k}$) can be express by

$$E_{analyzer}^{k} = h\nu - E_b - \phi_{analyzer}. \tag{3.4}$$

With tunable synchrotron light, one may select appropriate photon energy for the excitation or one can scan excitation photon energy measure absorption spectrum,

which is known as imaging XAS. In the imaging PEEM mode, the contrast mechanism may be due to the spatial variation of topology, work function, elements and magnetic domains, as illustrated in Figure 3.13. The spatial resolution for PEEM is about 20-50 nm, depending on the excitation photon energy. An imaging energy analyzer provides a possibility for imaging XPS.
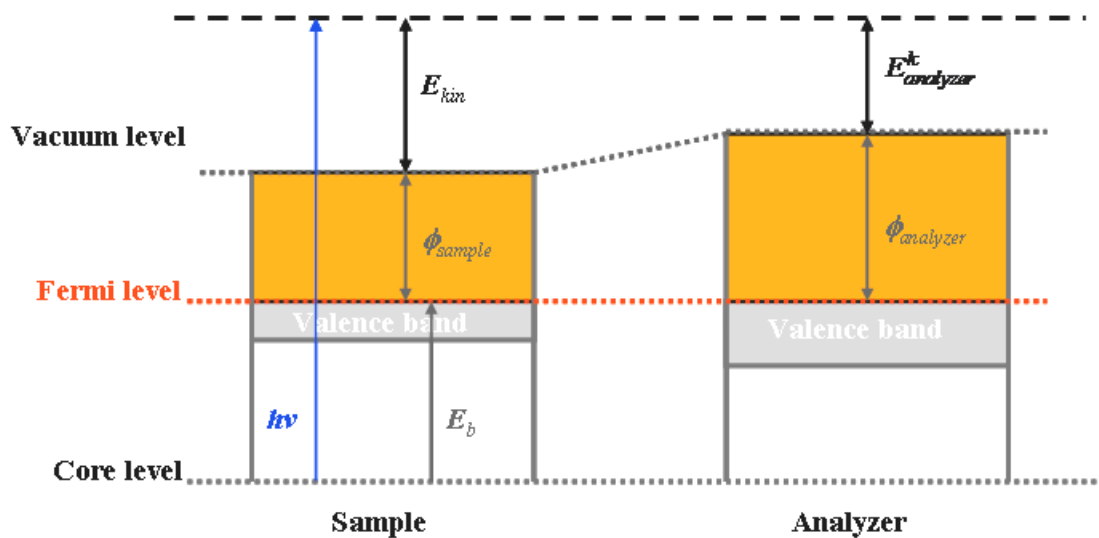
Figure 3.10 Schematic diagram demonstrating the sample-analyzer work function in photoemission technique.

3.4.3 LEEM electron optic

The electron optics in any LEEM system is designed and optimized for electrons with a fixed narrow energy range, that is the energy range about the energy of electrons extracted from the electron gun, typically 20 keV. The condenser lenses and deflectors are used to condition the electron beam coming from the electron gun. As the sample has to be perpendicular to beam direction, a sector magnet (or separator) is employed to provide a common optical axis between the objective lens and the

sample for the incident and reflected electron beams. The electron beam from the sample is successively magnified by the objective lens, transfer lens, field lens and then projected to mid-plane of the imaging analyzer. After the exit of the analyzer, the energy-analyzed beam is projected on the multi-channel plate (MCP), which is a 2-dimentional electron multiplier. The electrons from MPC are accelerated to collide with a phosphor screen. Thus the image of the sample is formed on the phosphor screen and is recorded with a CCD camera connecting to a computer. The description for electron optics mechanism will be described later in the mode of operations. The abbreviation for electron optics lens in Figure 3.11 are denote as following:

Illumination column is composed of collimating 1, 2, 3 (CL1, CL2, CL3) use to collimated the electron beam.

Imaging column is composed of transfer lens (TL), field lens (FL), illumination len (IL) and projector lens (P1)

Projector column is composed of projector lens (P2 and P3).
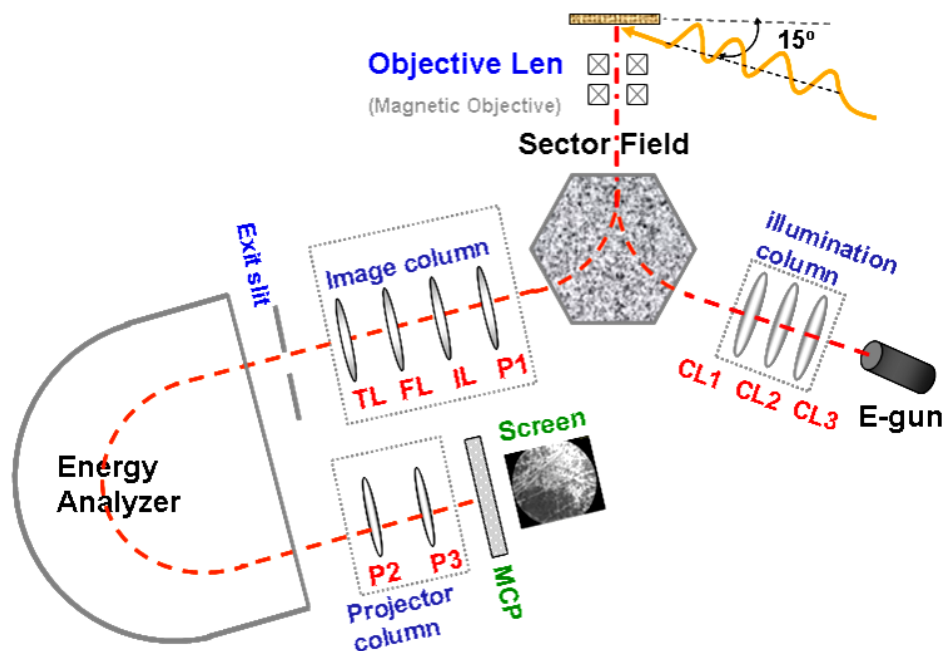
Figure 3.11 The schematic of electron optics for LEEM III equipped with an imaging energy analyzer.

3.4.4 Imaging mechanism in LEEM

The principle of LEEM is the interaction between electron and the surface of the specimen at low energy which provides elastic and inelastic scattering. Whether the energy of electrons is higher than several hundred electron volts, the electrons will travel fast enough to dominate the forward elastic scattering compared with the inelastic scattering. In this case, the first Born Approximation is used to estimate the behavior of interactions. In contrast with the low energy electron, ranging 1-100 eV, some scatter electrons may dramatically change their momentum in the opposite direction of the incoming beam which is called backscattering process. According to the backscattering cross sections between the light and heavy atoms (substrate) are quite different, hence those back scattered electrons can be collected for imaging.

Moreover, diffraction patterns of wave properties of electron can be observed in LEED mode of LEEM. Since these diffraction patterns arise from low energy electron diffract from the periodic of lattice of atom. The center spot of LEED pattern is the direct reflected beam while other spots are caused from the diffraction process. The advantage of LEED mode in LEEM is choosing one of the diffraction spots by using contrast aperture for imaging. The image by select the center spot is called "**bright field**" image while other spots called "**dark field**" image which give in detailed in the mode of operation later.

3.4.5 Mode of operations

Schemidt et al. (1998) give an explanation for electron optics of LEEM III in different mode of operations to produce image, diffraction spot, and photoemission microscope as shown in Figure 3.12 as well as, the description of the mode of operations is given from Microscope procedure manuals at Nanospectroscopy Beamline at Elettra synchrotron, Italy, as follows:

3.4.5.1 LEEM imaging mode

As electron gun as a source, the sample is illuminated with electrons. From Figure 3.12, IL and P1 located the specimen image produced by the objective. The final image is projected onto the detector by the action of P2 and P3. For improvement the image contrast, insert the contrast aperture in the diffraction plane to restrict the angular acceptance for optimum lateral resolution.

Figure 3.12 Electron optics for (a) imaging mode, (b) diffraction mode, and (c) spectromicroscope mode (Schemidt et al., 1998).

3.4.5.2 PEEM imaging mode

The sample is illuminated with x-rays or UV radiation, to excite photoemission. It is also the same optics operation as in LEEM imaging. A slit is inserted in the dispersive plane of the analyzer, in order to select the desired energy of the photoelectrons. The final image is projected onto the detector by the action of P2 and P3. The contrast aperture in the diffraction plane limits the angular acceptance for optimum lateral resolution. The contrast mechanism for PEEM arises from electric field distortion at surface topography features and the different in local work function as shown in Figure 3.13 (a) as well as described following:

- **The topological contrast** appears on rough samples and is caused by the distortion of the electric field around topographic features of the surface. The field distribution distortions disturb the electron trajectory leading to an image contrast. Figure 3.13 (b) illustrates the surface topography and their corresponding PEEM images;

- **Work function contrast** illustrated using UV illumination with energy close to the work function of the surface. It demonstrated the intensity modulation of the photoemission intensity due to the different emission of local work function;

- **Elemental contrast** is an element-selective imaging arising from tuning the synchrotrons radiation form infrared (meV) to hard x-ray (keV). Many light elements give strong absorption edges, thus will appear contrast in the final image;

- **Magnetic contrast** exhibit magnetic domains, which can be visualized by PEEM imaging using polarized X-ray i.e. X-ray Magnetic Circular Dichroism (XMCD) or X-ray Magnetic Linear Dichroism (XMLD) so the different contrast of specimen due to the polarization of the incoming synchrotron light can be investigated to monitor studied magnetization area of specimen.

(a)

hν

e$^-$

topographic   elemental/   work   magnetic
                chemical   function   domains

(b)

Corresponding PEEM images

Electron
trajectories

Topographical surface features
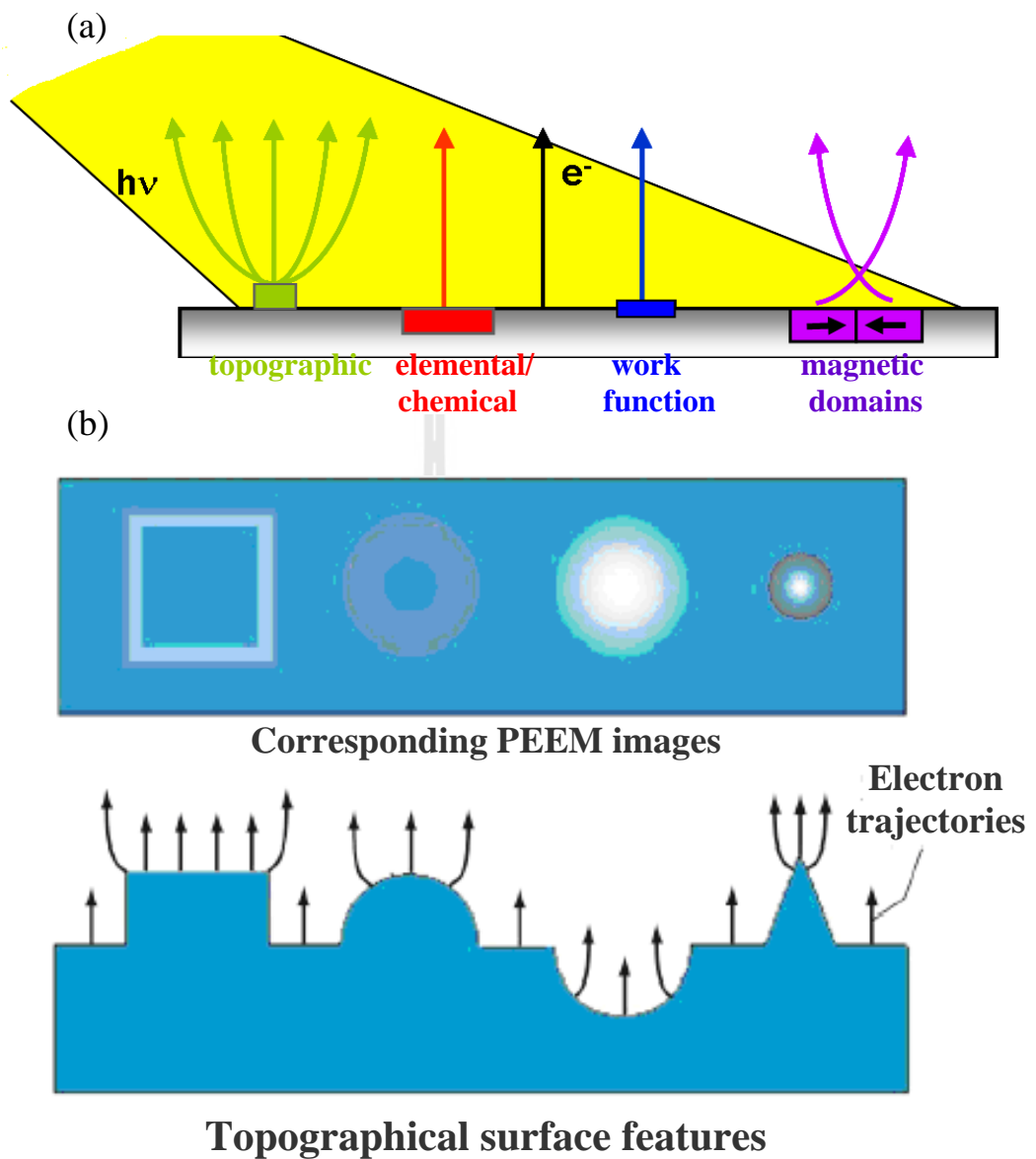
Figure 3.13 Imaging mode for PEEM (a) the surface sensitivity of contrast mechanism for PEEM and (b) the topography surface features and their corresponding PEEM images (Stohr and Anders, 2000).

3.4.5.3 Diffraction mode

The sample is illuminated with low energy electrons for LEED mode, or soft x-rays or UV radiation for photoelectron emission angular distribution (PEEAD). IL

and P1 image the diffraction pattern produced in the back focal plane of the objective lens. Inserting the analyzer exit slit allows angle resolved photoemission and x-ray photo-electron diffraction measurements. The probed area is selected by inserting the field-limiting aperture in the image plane after the objective lens, the contrast aperture is removed. The schematic for imaging and diffraction plans is shown in Figure 3.14, since there are two mode of diffraction for e-gun source as follows:

- **Lateral diffraction, dark field imaging** is the choosing of one of LEED spots except the center beam. All areas on the surface that correspond to these spots appear bright in the image, while the other areas appear dark. While varying electron energy at the same time recording the LEEM images, this is also measuring the intensity of the specula beam at very low energies the so called "LEEM/IV" (by recording the current absorbed by the sample analogous to LEED/IV study);

- **Vertical diffraction, phase contrast** is useful to investigate the steps on the surface of the specimen. The basic principle is the interference of the wave nature of the incoming electron beam. The destructive interference occurs between the adjacent terraces present steps separating of the terraces as the dark line in the image. In contrast with all terraces will appear as the same gray level in the microscopic image.
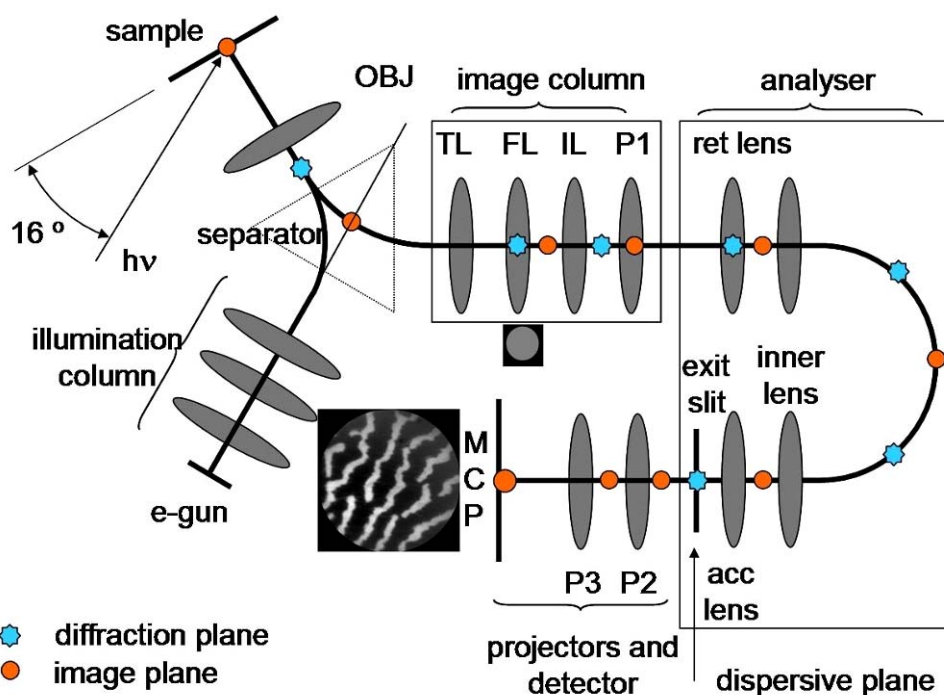
Figure 3.14 Schematic of the plane for image and diffraction (Locatelli and Bauer, 2008).

3.4.5.4 Micro- XPS or dispersive plane operation

The last two projectors of the imaging column, P2 and P3, are used to image the dispersive plane of the analyzer. The dispersive plane appears as a thin line, and its intensity profile represents the photoemission spectrum. The probed area is selected by the field limiting aperture inserted in the image plane after the objective lens. This operation mode allows imaging an energy window of about 12 eV. It is used to acquire local XPS spectra from an area of 2 µm diameter.

3.4.5.5 Micro- XAS mode

The utilities for tunable synchrotron light are used for scan energy by choosing the energy near the edge of the element that is required to be measured. Therefore, the

stack of images that measure will be converting to spectrum by Image-J. Figure 3.15

is an example for XAS measurement of Ag-3d$_{5/2}$ edge by Winkler (2009).

3.5 Theory Concerned with PEEM Function

3.5.1 Principles of operation

Remperf and Griffith (1987) describe the electron optics used in PEEM as

follows: According to PEEM is based on the cathode lens which is shown in Figure

3.16. A flat specimen is in the position separate from the aperture lens by a distance l.

The uniform accelerating electric field applied between the specimen ("cathode") and

the anode is V_A. Figure 3.17 (a) demonstrate the electron trajectories from a specimen

point on the axis. The electron paths are parabolic arcs which diverge after passing

through the aperture lens.
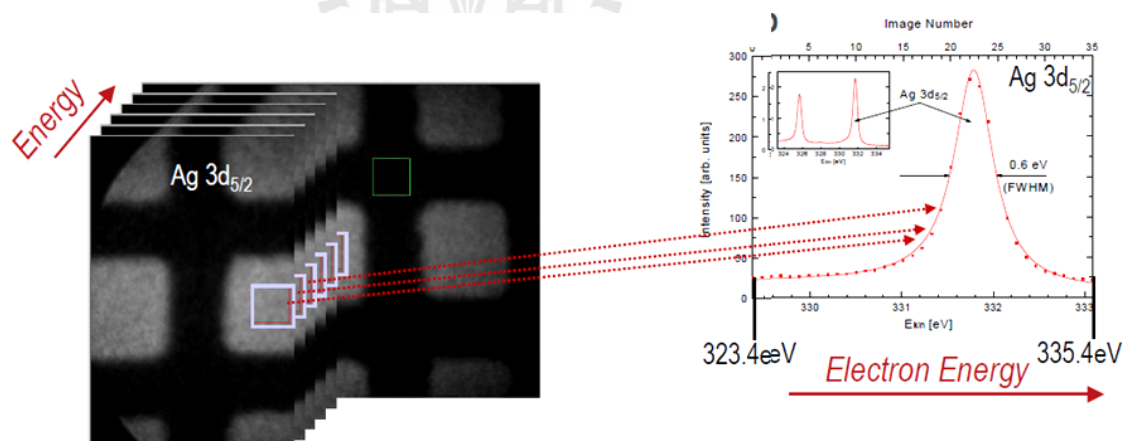
Figure 3.15 The PEEM integrated with Energy Analyzer data analysis of Ag

evaporated on Ta in miro-XAS mode. (Winkler, 2009)

Figure 3.17 (b) show the tangent to the parabolic electron trajectories have been extended backward to the intersection point resulted in a virtual image at distance l *=2 l from the anode. Thus l * is now the object of the aperture lens, with a focal length f = -4l which is shown in Figure 3.17 (b). Therefore, the virtual specimen distance is 4/3 l from the anode minified by 2/3. The virtual image shown in Figure 3.17 (b) is now the object for the objective lens.
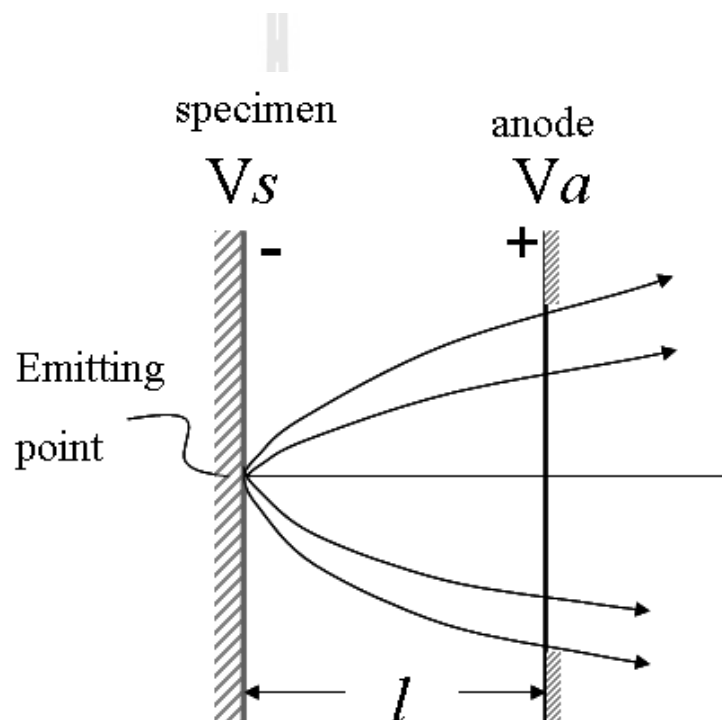
Figure 3.16 Trajectories of electron emitted from a specimen point on the axis showing the curved paths in the accelerating region and the diverging action of the aperture lens. (the beam size in the figure is exaggerated)
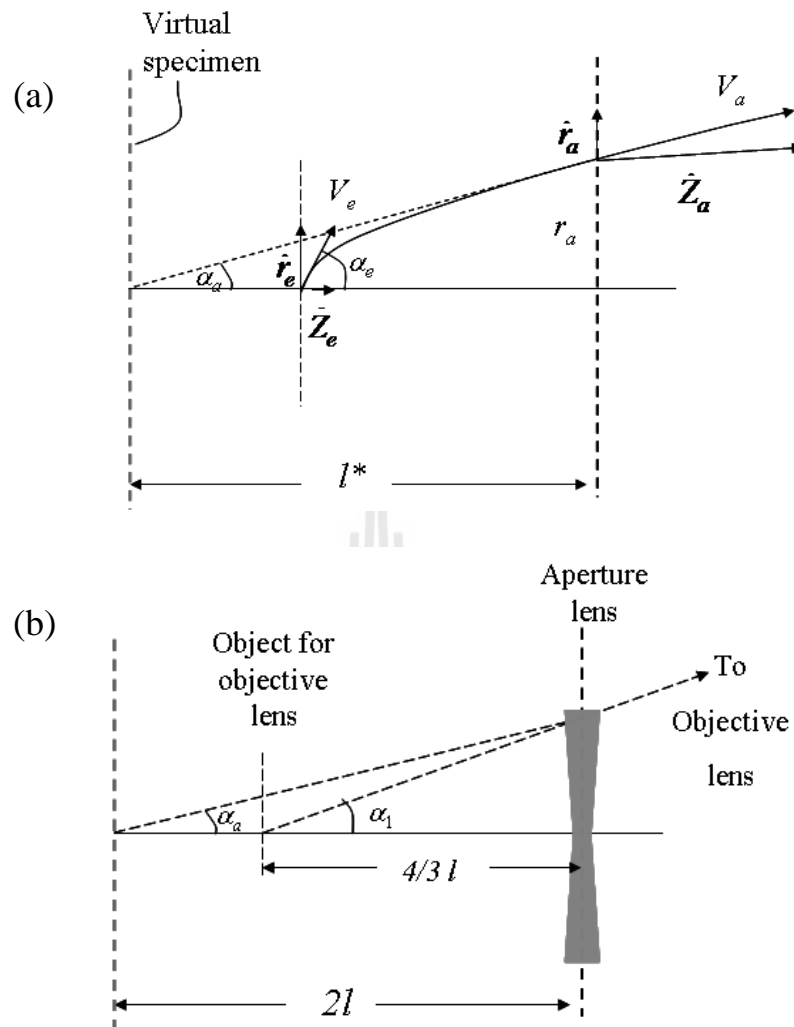
Figure 3.17 (a) Detail of the accelerating region showing a trajectory and a tangent ray defining the position of the virtual specimen at a distance l^* from the anode. The components of the emission velocity v_e are $\dot{r}_e$ and $\dot{z}_e$ while the components of the velocity v_a after acceleration are $\dot{r}_a$ and $\dot{z}_a$. The initial and final tangents make angles α_e and α_a respectively, with the axis. (b) Electron optical equivalent for the case of a uniform accelerating field combined with the diverging aperture lens. The focal length of the aperture lens for low emission energies is $f_A=-4l$. The virtual specimen is at a distance of $2l$ from the aperture lens. The aperture forms a virtual image of the virtual specimen at a distance of $4/3l$ and a magnification $M_A = 2/3$.

3.5.2   Image composition

3.5.2.1 Resolution

Consideration of the effect of electron emission velocity accelerated by the electron ejection voltage V_e , yields $eV_e = 1/2\, mv_e^2$. Thus the position of the virtual specimen formed by the accelerating field using the first approximation is given by

$$l* = \frac{2l}{(1 + \dot{z}_e / \dot{z}_a)} = 2l\left(1 - \left(\frac{V_e}{V_a}\right)^{1/2} \cos\alpha_e\right). \tag{3.5}$$

The subscript "*e*" refers to values at electron emission and the "*a*" to values after acceleration. Therefore, the chromatic and spherical aberrations of the accelerating field are proportional to $(V_e/V_a)^{1/2}$ and are due to the variation in $l*$. The parameters that are affecting resolution are the average electron emission energy, the width of emission energy distribution, and the aperture size. From Figure 3.17, the emission angle, α_e is related to tangent angle, α_a to the first order by

$$\alpha_a = \left(\frac{V_e}{V_a}\right)^{1/2} \sin\alpha_e . \tag{3.6}$$

Rempfer (1992), Rempfer and Griffith (1992), Rempfer and Mauch (1992) and Rempfer, Nadakavukaren and Griffith (1980), numerically studied the electrostatic objective lens for PEEM by including aberration of the accelerating field, aperture and diffraction limit. Except for the microscope designer, the resolution of emission microscope is usually calculated from the Recknagel formula which simply expresses the resolution for an axial point as V_e/E. Since $E=V_a/l$ resulting the resolution is

$$\rho = lV_e / V_a \tag{3.7}$$

when l = 3mm, V_e = 0.25 V and V_a = 30 kV, so the resolution will be 25 nm. The resolution calculation for the radius of least confusion for α_e = 90° and at the correct location, for the plane of least confusion $r_{le} = 0.6\, lV_e/V_a$ will be 15 nm. For experimental measurement the resolution for PEEM has been realized about 7 nm examined by Rempfer, Nadakavukaren and Griffith (1991).

3.5.2.2 Depth of field

Rempfer, Nadakavukaren and Griffith (1980) also calculated the depth of field in PEEM by a simple description of the concept as follows: Smooth, flat specimens are preferred in PEEM, because uniform illumination is difficult on a specimen with large surface relief. Topographical relief causes variation in the accelerating field at the surface. The difference in cathode-to-anode distance from the top to the base of a surface feature can affect the image due to emitted electron traveling slowly in the initial stages of acceleration. Hence, trough, depressions and bumps on surface appear to be several times deeper or higher in the image than their actual size. The **"dept magnification",** denoted by M^*, of surface relief by the accelerating field is proportional to $(l/\delta)^{1/2}$, where δ is the depth of the surface feature as shown in Figure 3.18. Generally, the δ is on the order of um, and l is usually several mm, the depth magnification can be large.

The dept magnification of planar region of the specimen is just 2, in virtual specimen space. The distance from the anode to the virtual specimen surface l^*, is $2l$, the distance to the bottom of the step of height is $l^* + \delta^* = 2\,l + 2\delta$. Therefore, yielding

$$\delta_p^* = M^*\delta = 2\delta . \tag{3.8}$$

As mentioned before that, if there is topographical relief, then $(l/\delta)^{1/2}$ must be included, yielding δ^*_{relief} can be much larger than the depth of field as expressed by

$$\delta^*_{relief} = (l/\delta)^{1/2} \, \delta = (l\delta)^{1/2} \,. \tag{3.9}$$

3.5.2.3 Depth of information

The depth of information in PEEM is determined by the escape depth of the photoelectrons. If the electron escapes from the finite depth in a material according to the low energy of photoemitted electron, the "bloom" area is usually less than in TEM or SEM. Since, PEEM forms a Gaussian image of the surface, so that electrons are collected from a specific depth while in SEM the total photoemitted electron at the illuminated area is collected. Thus, the depth of information is determined by the full escape depth of a wide energy range of secondary electrons both in the bloom area on surface and from the volume beneath the electron-beam probe. Veneklasen (1991) described that the photoemission processes contributing to the total electron yield usually divide in to four stops as follows:

i) The absorption of the photon is determined by the probability that a photon of energy *hv* is absorbed at a depth *z* in a thickness *dz* and is given by

$$dP_{ab} = \beta \exp(-\beta z)dz \,, \tag{3.10}$$

where β is the wavelength-dependent optical absorption coefficient.

ii) Photoinoization at a depth *z* in the specimen which depends on the quantum yield and is independent of *z*.
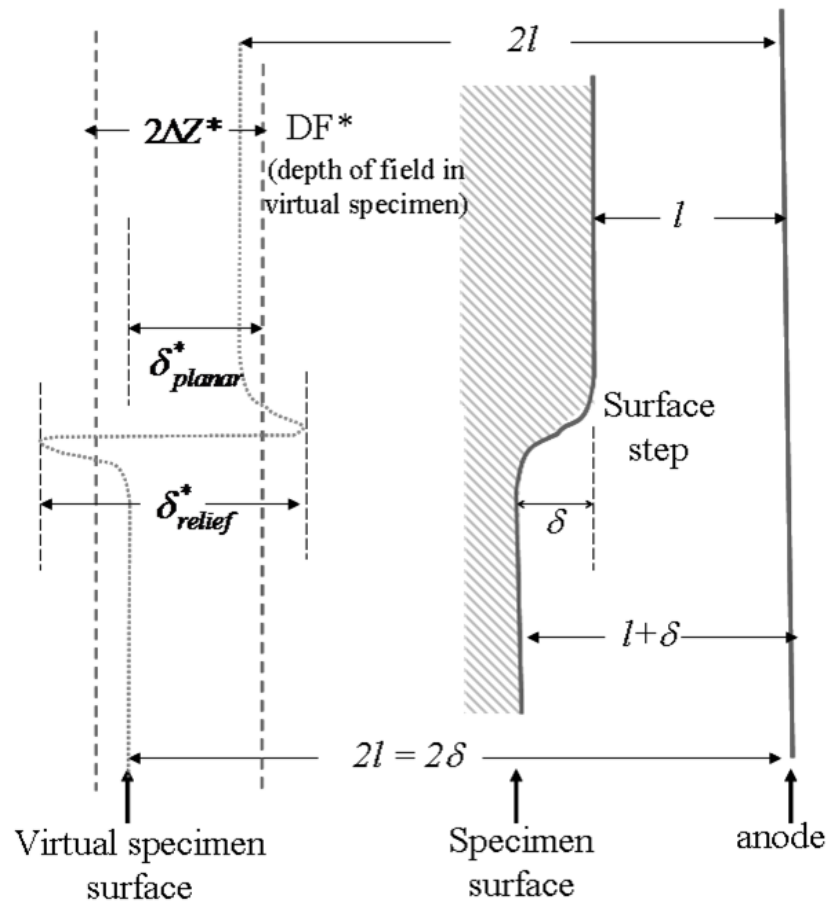
Figure 3.18 Rempfer, Nadakavukaren and Griffith (1980) demonstrated the diagram for a single-step sample and the qualitative representation of the virtual specimen surface (dotted line). The surface step height is δ. The virtual specimen surface shows the nature of the depth magnification, δ^*_{relief}, arise from the field perturbation in the vicinity of the step. The depth of surface feature far away from the step is $\delta^*_{plana} = 2\delta$. Hence, the depth of field in virtual specimen space is DF* = 2ΔZ*.

iii) Transport of the electron at the surface $z = 0$ which is a scattering process limited by an energy dependent mean free path, P_{trans} is given by

$$P_{trans} = \exp\left[-z/L(E)\right]. \qquad (3.11)$$

It also can be approximated by an energy-independent attenuation length, L.

iv) Escape into the vacuum. The escape probability at the surface does not depend on z.

Integration of all four probabilities from $z = $ d to $z = 0$, including the second and fourth process steps, in a constant prefactor C give the result that the total electrons yield can be written as

$$Y(d) = C\left\{1 - \exp\left[-\left(\beta + 1/L\right)d\right]\right\}. \qquad (3.12)$$

3.5.2.4 Intensity

Illumination intensity is a major limitation of the PEEM technique due to the ability to focus the image at the magnification chosen. The kinetic energy of photoelectron is given by the photoelectric effect equation as

$$E_{kinetic} = hv - \phi, \qquad (3.13)$$

where ϕ is the work function defied as the potential energy barrier between the highest occupied electron state in the solid and the vacuum outside of the solid. It usually depends on the surface termination or adsorbate.

The electron yield (photocurrent density, $j(v)$) is determined by the number of electrons ejected per photon which is proportional to the intensity of the illumination source above some threshold value, $v_t = \phi/h$. The photocurrent density is the result

from a photon flux $B(v)$ of wavelength between $v + dv$ and an electron yield $\varepsilon(v)$, is

$j(v)dv = \varepsilon(v)B(v)$; thus the integrated current is given by

$$J = \int\limits_{\phi/h}^{v_{max}} \varepsilon(v)B(v)dv. \qquad (3.14)$$

This shows that the photocurrent directly depends on the work function? From the assumptions explained by Rempfer (1992), Rempfer and Griffith (1992), it can be shown that small changes in the work function are directly proportional to small changes in the integrated photocurrent; yielding

$$\Delta J = -\Delta\phi. \qquad (3.15)$$

From this relationship, it can be sued to calibrated thickness- or coverage-dependent contrast/image brightness effect.

3.5.2.5 Contrast

As mentioned before, the contrast mechanism in PEEM can have various origins i. e., 1) variation in the electron yield, 2) deflection or focusing of electron into or out of the collection volume of the objective lens/aperture, most usually topographical relief, and 3) shadows cast by surface features. The contrast mechanisms are demonstrated in Figure 3.19.
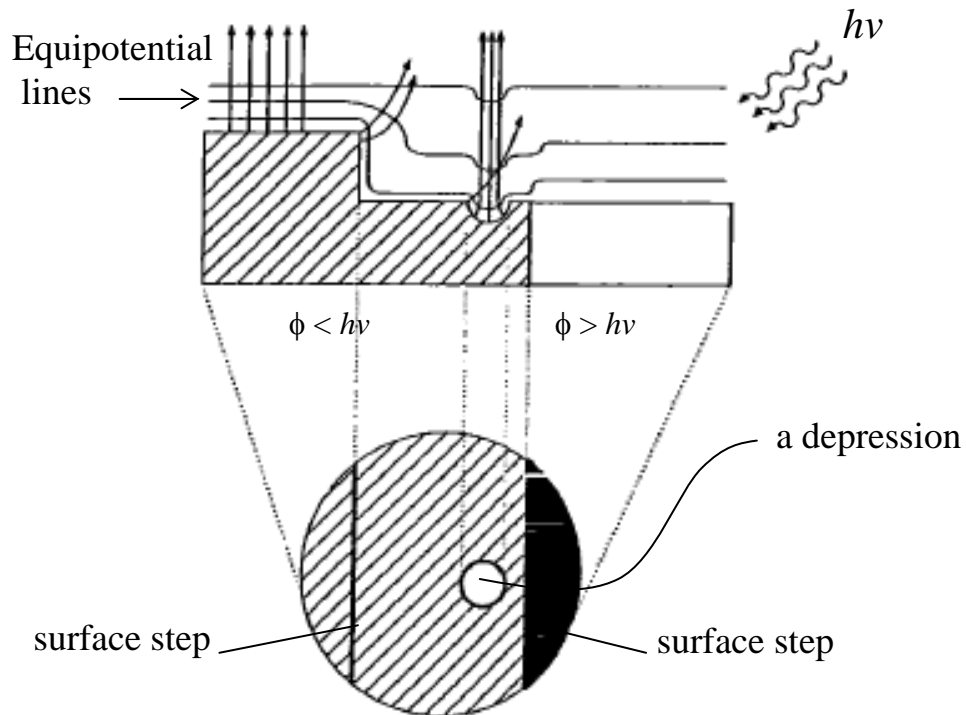
Figure 3.19 Diagram for contrast mechanism in PEEM for composite surface (denoted by equipotential lines) with the work function ϕ and illuminated by photon energy hv. The circle below represents the image obtained in PEEM where the dark area for $\phi > hv$, bright for $\phi < hv$. The topography contrast arises from a step and a depression in the surface as shown on the left half on the image (Kordesch, 2006).

3.6 Low Energy Electron Diffraction (LEED)

Conventional LEEM is a powerful technique for observing the atomic arrangement at the surfaces of crystalline materials. The basic principle of LEED may be explained by the wave nature of a collimated beam of low energy electron (20-200 eV) incident on crystalline materials. The electron wave reflected from the periodic structure at the surface from the diffraction pattern on a fluorescent screen as illustrated in Figure 3.20.

The wavelength of the corresponding de Broglie wave for an electron is given by

$\lambda = \dfrac{h}{\sqrt{2mE}}$, or it can easily be rewritten as a function of electron energy as

$$\lambda[\overset{\circ}{A}] = \sqrt{\frac{150}{E[eV]}} \,. \tag{3.16}$$

The corresponding wavelength of 20 eV electrons and 200 eV electrons are as follows:

20 eV - electrons: $\qquad \lambda[\overset{\circ}{A}] = \sqrt{\dfrac{150}{20}} = 2.74 \ \overset{\circ}{A} \,. \tag{3.17}$

200 eV - electrons: $\qquad \lambda[\overset{\circ}{A}] = \sqrt{\dfrac{150}{200}} = 0.87 \ \overset{\circ}{A} \,. \tag{3.18}$

It is obvious that the corresponding wavelength of the electrons used in the LEED technique is comparable to the repeat distance in the surface structure. LEED patterns provide information of crystalline structures from the surface to the depth of about 10 $\overset{\circ}{A}$, depending on materials and the energy of the electron beam. This is because of the short inelastic mean free path of low-energy electrons in matters. It is always convenient to treat the diffraction of the low-energy electron beam of crystals

in the reciprocal space. In 3 dimensions, the real primitive vector {a, b, c} is used to describe the real 3D lattice. In the reciprocal lattice, the primitive reciprocal vector are relayed to the real primitive vector as following

$$\mathbf{a}^* = \frac{2\pi(\mathbf{b}\times\mathbf{c})}{\mathbf{a}\cdot(\mathbf{b}\times\mathbf{c})}, \qquad \mathbf{b}^* = \frac{2\pi(\mathbf{c}\times\mathbf{a})}{\mathbf{a}\cdot(\mathbf{b}\times\mathbf{c})}, \qquad \mathbf{c}^* = \frac{2\pi(\mathbf{a}\times\mathbf{b})}{\mathbf{a}\cdot(\mathbf{b}\times\mathbf{c})} . \qquad (3.19)$$

The reciprocal vector G is given by

$$\mathbf{G}_{hkl} = h\mathbf{a}^* + k\mathbf{b}^* + l\mathbf{c}^* , \qquad (3.20)$$

where h, k, l are a set of integer numbers. The incident and scattered electrons can conveniently be described as plan waves with wave vectors $\mathbf{k}_0 = 2\pi/\lambda_0$ and $\mathbf{k} = 2\pi/\lambda$. The condition for constructive interference of scattered electron waves is governed by the Laue condition, i.e.,

$$\mathbf{k} - \mathbf{k}_0 = \mathbf{G}_{hkl}, \qquad (3.21)$$
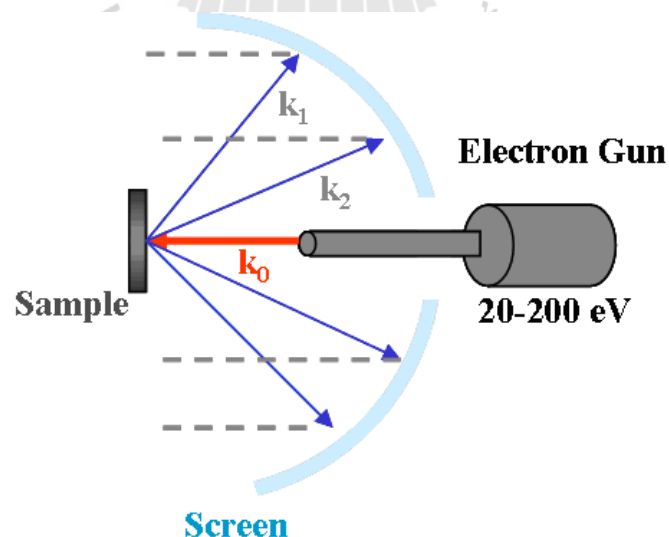
Figure 3.20 A typical LEED experimental set-up.
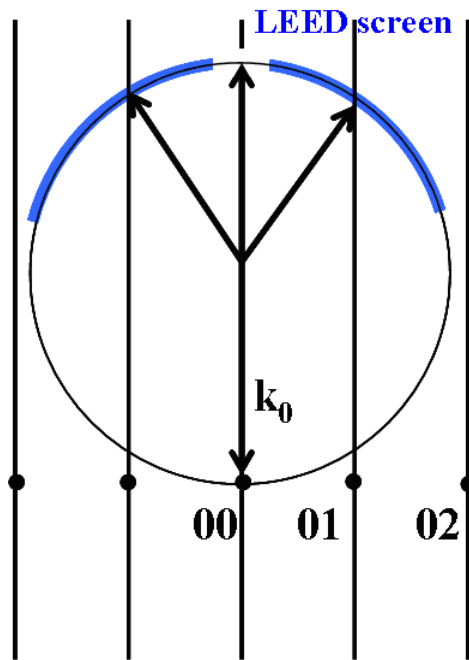
Figure 3.21 Ewald's sphere construction for the case of a normal incidence of the primary electron. The allowed diffraction spot on the LEED screen are the points where the Ewald's sphere intersects with the reciprocal lattice rods.

A simple graphical illustration of the diffraction can be visualized by using the Ewarld's sphere construction as shown in Figure 3.21. Since the elastic scattering is considered, the magnitudes of the incident and outgoing wave vectors are equal. As the inelastic electron men free path is only a few atomic layers, the scattering electrons considered are from the surface. Thus it is the diffraction from a 2 dimensional surface structure, and Equation (3.21) can be reduced as

$$\mathbf{k}^{\Box} - \mathbf{k}_0^{\Box} = \mathbf{G}_{hk} = h\mathbf{a}^* + l\mathbf{b}^*, \tag{3.22}$$

where $\mathbf{k}_0^{\Box}$ and $\mathbf{k}^{\Box}$ refer to the components of incident and scattered wave vectors parallel to the sample surface respectively, $\mathbf{a}^*$ and $\mathbf{b}^*$ are the primitive translation vectors of the 2D reciprocal lattice of the surface. Equation (3.22) is the 2D Laue

condition and is demonstrated in Figure 3.21. The complete constructive interference occurs at every intersection between a reciprocal rod and the Ewald's sphere of radius k_0 with its center at the origin.

It should also be emphasized that LEED is a very surface sensitive technique. LEED patterns provide information on the arrangement of atoms at the surface vicinity, from the surface down to a few monolayers, depending on the atomic composition of the crystals. To obtain a LEED pattern with good signal-to-noise ratio, the surface of the sample must be clean and well-ordered. In actual LEED experiment, an ultra-high vacuum environment is essential to prevent any surface contaminations.

3.7 References

Altman, M. S., Chung, W. F. and Liu, C. H. (1998). LEEM Phase Contrast. **Surf. Rev. Lett.** 5(6): 1129-1141.

Bauer, E. (1994). Low energy electron microscopy. **Rep. Prog. Phys.** 57(9): 895-938.

Bauer, E. (1998). Reviews: LEEM Basic. **Surf. Rev. Lett.** 5(6): 1275-1286.

Bauer, E. and Telieps. W. (1988). **Emission and low energy electron reflection microscopy.** In Howie, A. and Valdre, U. (ed.). Surface and interface characterization by electron optical methods. Plunum, New York.

Elettra synchrotron. (2010). **Microscope procedures**. [On-line]. Available: http://www.elettra.trieste.it/experiments/beamlines/nano/htdocs/microscopeproc/ microscopeproc.html.

Griffith, O. H. and Rempfer, G. F. (1987). **Advances in Optical and Electron Microscopy.** Barer. R., Cosslett, V. E. Eds. Academic Press: London. 10: 269-337.

Heun, S. and Salviati, G. (2000). Nano-scale spectroscopy and its applications to semiconductors. **Notiziario Neutroni e Luce di Sincrotrone** 5(1): 23-33.

Heun, S., Schmidt, Th., Ressel, B., Bquer, E. And Prince, K. C. (1999). Nanospectroscopy at Electtra. **J. Synchrotron Rad.** 6: 957-963.

Hibino, H., Kageshima, H., Maeda, F., Nagase, M., Kobayashi, Y. and Yamaguchi, H. (2008). Microscopic Thickness Determination of Thin Graphite Films Formed on SiC from Quantized Oscillation in Reflectivity of Low-energy Electrons. **Phys. Rev. B** 77: 075413-075425.

Hubbard, A. T. (1995). **The Handbook of Surface Imaging and Visualization.** CRC Press, Inc. USA.

IBM research. **Low energy electron microscopy**: Measurement and analysis. (n.d.). [On-line]. Available: http://www.research.ibm.com/leem.

Kordesch, M. E. (2006). Photoelecetron Emission Microscopy of Surface. **Encyclopedia of surface and colloid science**. 4572-4583.

Locatelli, A. and Bauer, E. (2008). Recent advances in chemical and magnetic imaging of surfaces and interfaces by XPEEM. **J. Phys. Condens. Mater.** 20: 093002 1-22.

Rugmai, S., Dasri, T., Siriwattanapaitoon, S., Kwankasem, A., Sooksrimuang, V., Chachai, W., Suradet, N., Juthong, N., and Tancharakorn, S. (2007). Soft X-ray undulator for the Siam Photon Source. Ninth International Conference on Synchrotron Radiation Instrumentation: **AIP Conference Proceedings**. 879: 335-338.

Rempfer, G. F. (1990). A theoretical study of the hyperbolic electron mirror as a correcting element for spherical and chromatic aberration in electron optics. **J. Appl. Phys.** 67: 6027-6040.

Rempfer, G. F. (1992). Methods of calculating resolution in electron microscopy: Scherzers equation, circles of least confusion and the intensity distribution approach. **Ultramicroscopy**. 47: 241-255.

Rempfer, G. F. and Griffith, O. H. (1989). The resolution of photoelectron microscopes with uv, x-ray, and synchrotron excitation sources. **Ultramicroscopy**. 27: 273-300.

Rempfer, G. F. and Griffith, O. H. (1992). Emission microscopy and related techniques: resolution in photoelectron microscopy, low energy electron microscopy and mirror electron microscopy. **Ultramicroscopy**. 47: 35-54.

Rempfer, G. F. and Mauck, M. S. (1992). Correction of chromatic aberration with an electron mirror. **Optik**. 92: 3-8.

Rempfer, G. F. Skoczylas, W. P. and Griffith, O. H. (1991). Design and performance of a high resolution photoelectron microscope. **Ultramicroscopy**. 36: 196-221.

Rempfer, G. F., Fyfield, M. S. and Griffith, O. H. (1998). Lenses for electron microscopy and microanalysis: shadowgraph method of determining focal properties and aberration coefficients. **Microsc. Microanal**. 4: 34-49.

Rempfer, G. F., Nadakavukaren, K. K. and Griffith, O. H. (1980). Depth of field in emission microscopy. **Ultramicroscopy**. 5: 449-457.

Schemidt, Th., Heun, S., Slezak, J., Diaz, J., Prince, K. C., Lilienkamp, G. and Bauer, E. (1998). Review: SPELEEM: Combining LEEM and Spectroscopic Imaging. **Ultramicroscop**y. 5(6): 1287-1296.

Stohr, J. and Anders, S. (2000). X-ray spectro-microscopy of complex materials and surfaces. **IBM J. Res. Devlop.** 44: 535-552.

Synchrotron Light Research Institute (Public Organiztion). **Beamline 3.2.** [On-line]: Available: http://www.slri.or.th/en/.

Tong-on, A. (2010). **Development of the optical system of the first undulator beamline for the Siam Photon Laboratory.** Ph.D. Dissertation, Suranaree University of Technology.

Veneklasen, L. H. (1991). Design of a spectroscopic low-energy electron microscope. **Ultramicroscopy**. 36: 76-90.

Winick, H. (1994). **Synchrotron Radiation Sources A Primer**. Singapore: World Scientific Publishing.
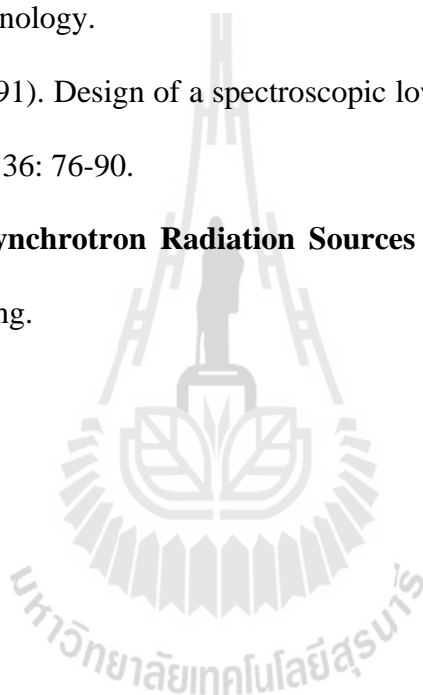
CHAPTER IV

DEVELOPMENT OF PEEM EXPERIMENTAL STATION

This chapter provides the description for the design considerations and the design of the PEEM experimental station for the BL3.2b beamline of SLRI, which was developed along the course of this thesis work. The PEEM experimental station is one of the ideal systems that provide possibilities to synthesize and in-situ characterize epitaxial graphene by thermal decomposition of SiC (Bertolo, 2003).

4.1 Design considerations

The main goal for setting up a PEEM experimental station at BL3.2b is for spectroscopic studies of solid materials with nanometer spatial resolution. The primary excitation source is synchrotron light produced from a planar undulator. The photon energy ranges available at BL3.2, 40-160eV and 220-1040 eV, cover the *K* energy level of light elements such as C, N, O and F and the *L* energy level of the transition metals. The required measurement techniques that are available at the experimental station are the followings:

- **PEEM**: This mode of operation of the experimental station is to provide images of samples with resolution of less than 100 nm (Wichtendahl, 1998). The excitation source are both, a Hg UV lamp and the synchrotron light source. The advantage of using synchrotron light is the possibility to tune photon energy to required values;

- **Nano/imaging XAS**: With the tuneability of photon energy of synchrotron light, PEEM images shall be obtained with series of excitation photon energy and thus imaging XAS. The XAS measurement shall be able to obtained from deduction of an area of interest with dimension of less than 100 nm from the energy-scan PEEM images;

- **Micro/imaging XPS**: This mode of measurement can easily be obtained if an electron energy analyzer is employed. Expected energy resolution of 250 meV is required. The spatial resolution shall be in sub-micron range;

- **LEEM**: The microscope is equipped with an electron gun to provide possibility to use the microscope for LEEM imaging, as well as VLEED observation.

In addition to various measurement techniques mentioned above, the experimental station is equipped with sample preparation system(s). A sample transfer system to transport samples between the sample preparation system(s) and the microscope is necessary to allow *in-situ* experiment, preventing surface contaminations. Certainly, a load-lock system is necessary to prevent breaking a UHV environment during the introduction of the sample into the experimental station. The sample holder is also be equipped with a heating system to allow the sample to be heated up to about 1700 °C.

More importantly, one need to keep in mind that the experimental station is be connected to the BL3.2 beamline. This put a constraint for designing the support or the table for the experimental station that shall be able to move the whole experimental station so that the synchrotron light beam hits the field-of-view of the microscope. The field-of-view for PEEMs is normally between a few microns to

hundreds microns. Thus the movements of the manipulator of the support is was required of micron accuracy.

4.2 Design of the PEEM experimental station

There are two types of commercially available PEEM systems, i.e. electrostatic and electromagnetic type (Rempfer, 1997). During the design of the PEEM experimental station, well-established technology to integrate PEEM with electron illumination column only existed in an electromagnetic PEEM system. Thus an electromagnetic LEEM-PEEM system was selected as a microscope for the experimental station.
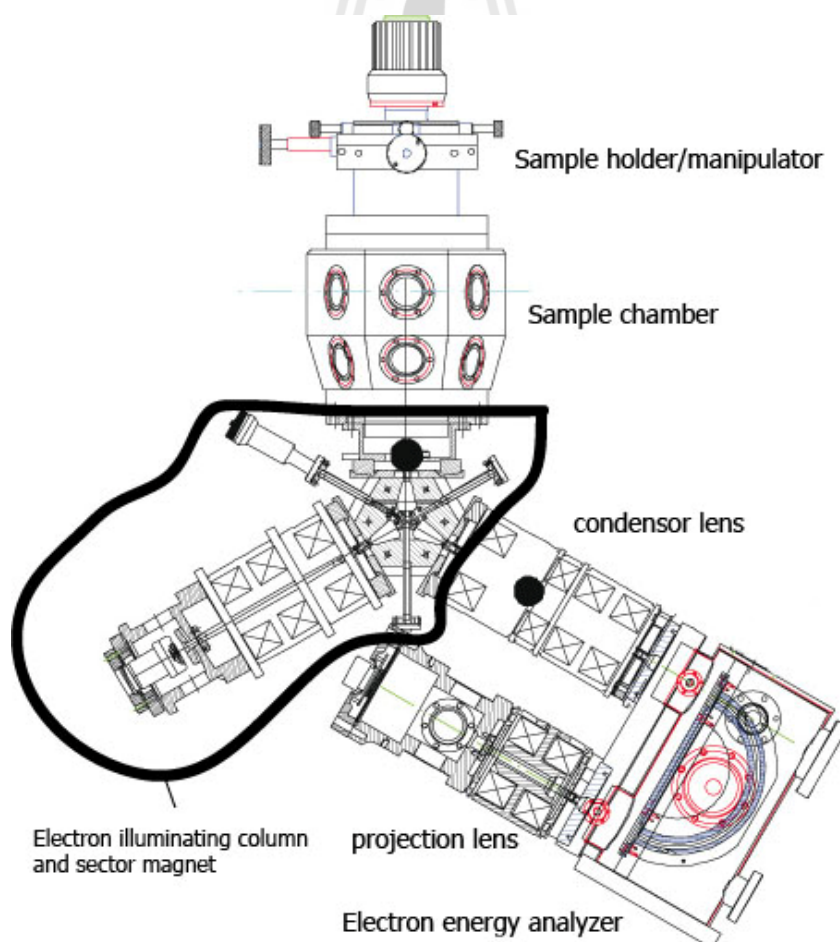
Figure 4.1   The schematic drawing of the ELMITEC LEEM III microscope.

An ELMITEC LEEM III system was chosen as an electron microscope of the experimental station of BL3.2b. The microscope is equipped also with an electron energy analyzer. Figure 4.1 shows the schematic drawing of the ELMITEC LEEM III, illustrating only the main components. The sample is held on a sample holder which is attached to the sample manipulator, allowing the sample to be oriented in required orientations. With a sector magnet, two electron optical axes originating from the sample are possible. One is for the electrons from the illuminating column. The illuminating column provides an electron beam for LEEM and LEED observations. The other electron optical line is for the imaging column. This column consists of the condenser and projection lenses. The energy analyzer is also inserted between the two lenses to select electrons with required kinetic energies. A combination of an MCD (multi channel plate) and a fluorescence screen is used to form the image. The electrons projected from the projection lens on the MCD are multiplied thru the micro-channels of MCD. An image is formed when the multiplied electrons hit on the fluorescence screen. A low-noise optical VDO camera is used to record the image on the fluorescence screen. The technical and performance specifications of the ELMITEC LEEM III with the energy analyzer are given in Table 4.1.

Only the microscope was purchased from ELMITEC. Thus, the main task of this thesis work was to design and integrate the sample preparation system, load-lock system, sample transfer system and the support to be a PEEM experimental station, and then connected to the BL3.2b beamline.

Table 4.1   Technical and performance specifications of the PEEM experimental station of BL3.2b.

Excitation sources:	Synchrotron light:
	40-160eV & 220-1040eV
	Hg UV discharged lamp
	LaB_6 electron gun
Measurement techniques:	UV & Synchrotron light PEEM
	Bright/Dark field LEEM
	MEM (mirror electron microscopy)
	Imaging/micro XPS
	Nano XAS
	Micro LEED
Spatial resolution in PEEM mode:	<20 nm
Spatial resolution in LEEM mode:	<10 nm (16% / 84% criteria)
Electron energy at the sample:	-5 to 1000 eV
Illumination area:	up to 80 micron in LEEM mode
	up to 150 micron in PEEM mode
Energy resolution	250 meV
Isochromatism in spectroscopic imaging mode	<0.5 eV/10 micron
Width of the energy dispersive plane	>10 eV
Deviation from linearity of energy dispersive curve	<5%
Sample temperature	between room temp. & 1700 °C

In a normal set up of the ELMITEC LEEM III system, the imaging column and the electron column of the LEEM III are laid on the horizontal plane, i.e. the electron optical axis of both columns is on the horizontal plane. Such orientation provides good stability for the LEEM system, and thus it is less sensitive to mechanical vibrations that might degrade the performance of the LEEM system. There is a stringent constrain for using the LEEM for PEEM observations because of the very short distance between the objective lens and the sample, which is about 2 mm. Thus, UV light or Synchrotron light used for excitation is designed for grazing geometry. The angle between the optical axis of the exciting light and the sample surface is only 17°. There is no difficulty to use a UV lamp for PEEM observation when the electron optical axes of the LEEM III system are on the horizontal plane since UV light from the lamp can be well-focused on the sample. Alignment of the lamp can be manually adjusted easily.

When the LEEM III has to be connected to a synchrotron light beamline, there are a few considerations that must be kept in mind. Firstly, the beamline cannot be moved and thus the microscope shall be able to move to allow the field-of-view of the microscope to be illuminated with synchrotron light. Secondly, the dimension of the synchrotron light beam on the sample is defined by the electron beam dimension and the optical system of the beamline. Normally, the vertical beam size is smaller than the horizontal beam size, and thus the light beam is elliptical with the a minor axis in the vertical direction. That is also true for the Siam Photon Source of SLRI. As already mentioned above, the synchrotron light beam impinges on the sample with an angle of 17° with respect to the surface of the sample. In order to maximize the number of photons in the field-of-view of the microscope, or minimum beam size

projected ontothe sample surface, the plane of incidence for the synchrotron light must be in the vertical plane. This constraint results in the design of the microscope installed as illustrated in Figure 4.2. It is noted that the synchrotron light delivered by the BL3 beamline is in the horizontal axis. Thus, the microscope is installed with the optical axis the electron column, the imaging column and the axis of the synchrotron light are in the vertical plane, as shown in Figure 4.2. The optical axis of the objective lens of the microscope is tilted 17° with respect to vertical angle.
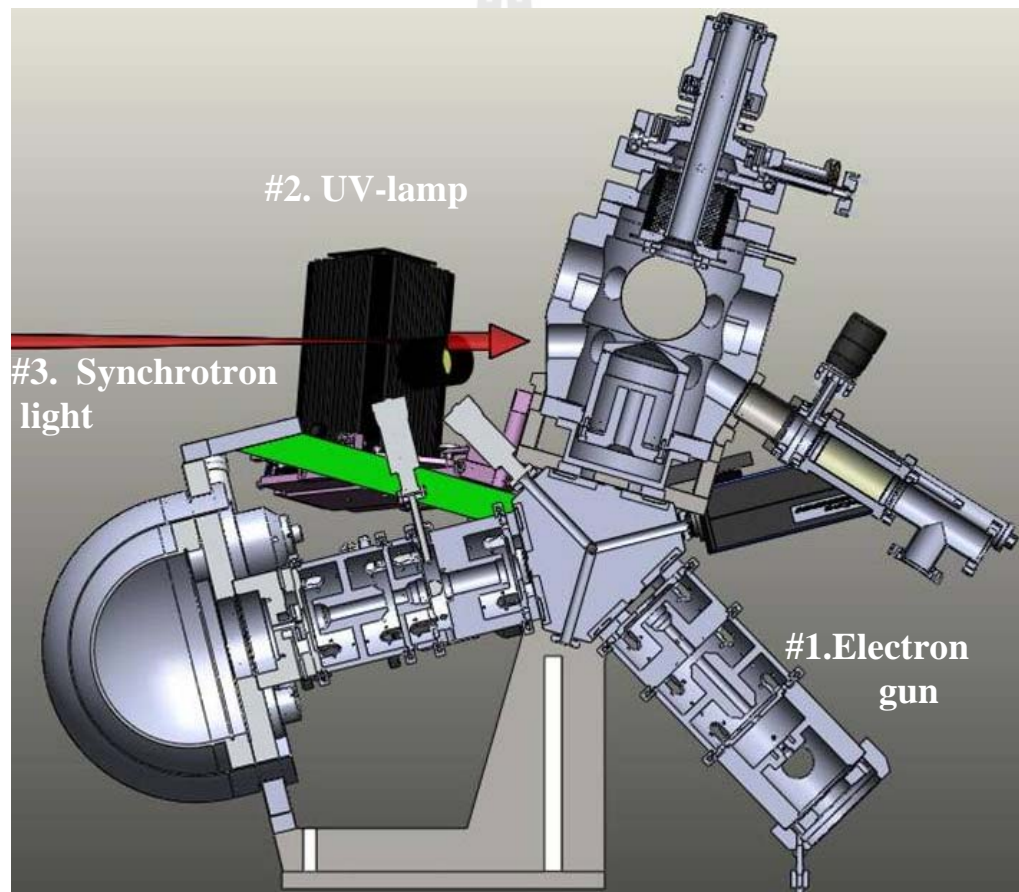
Figure 4.2   The set up of the ELIMTEC LEEM III showing the orientation of the microscope with respect to synchrotron light beam (red arrow).

The main chamber of the microscope, where the sample is located, is connected to two sample preparation systems and the beamline. The vacuum condition of the microscope is isolated from the beamline and the two sample preparation chambers by three gate valves, one for each connection. The imaging column, electron column and the energy analyzer of the microscope are evacuated by a combined 300 l/s and titanium sublimation pump and a 4000 l/s NEG (non-evaporated getter) pump. The main chamber, however, is evacuated thru the preparation chamber

The main chamber of the microscope is sandwiched by the two sample preparation chambers with vacuum-isolated gate valves. Viewing along the synchrotron light, the preparation system on the right side is currently in used. The preparation system is attached with a sample load-load system to prevent breaking of a UHV condition during the introduction of the sample. A magnetic linear drive is used to transfer the sample from the load-lock chamber to the parathion chamber. The sample carousal in the preparation chamber can accept up to three samples. Out gassing of the sample by electron bombardment heating can be carried out in the preparation chamber. In the future, an ion gun bombardment will be installed to provide a possibility for cleaning the surface of the sample. A magnetic linear drive is also used for transferring the sample from the preparation chamber to the sample holder in the main chamber of microscope. Since the chamber of the preparation chamber is rather small, a 20 l/s ion pump is sufficient to maintain a UHV condition in this chamber.

The preparation on the left side of the main chamber of the microscope is designed for future uses. This chamber is evacuated by a combined 500 l/s ion pump and titanium sublimation pump. This section is currently used as the vacuum reservoir

for the main chamber of the microscope. The gate valve between this preparation chamber and the main chamber of the microscope is normally kept open since the main chamber is pumped by the same pumping system. In the future, evaporation sources, and ion sputter gun, a sample manipulator and transfer system will be equipped to this preparation system.

The isometric and top views of the PEEM experimental station are shown in Figures 4.3 and 4.4, respectively. All mechanical components of the experimental station are installed on a table with 10-cm aluminum top. The top is quite heavy, providing a stable foundation of the microscope. In addition, this aluminum top is sitting on an anti-vibration system. The table is, in principle, an optical table allowing the experimental station to be rotated and translated to provide a maximum intensity of the synchrotron light beam in the field-of-view of the sample.
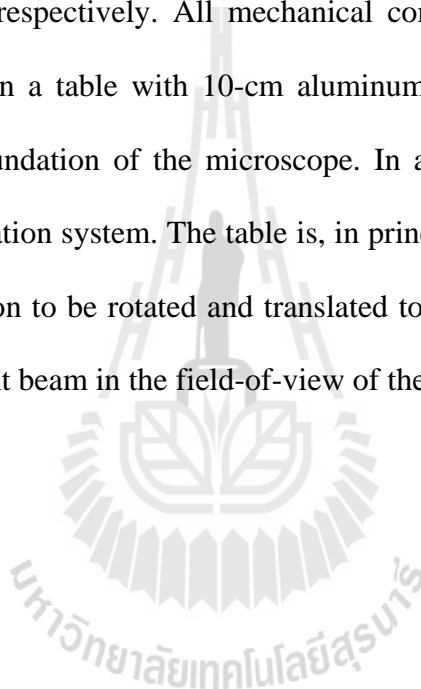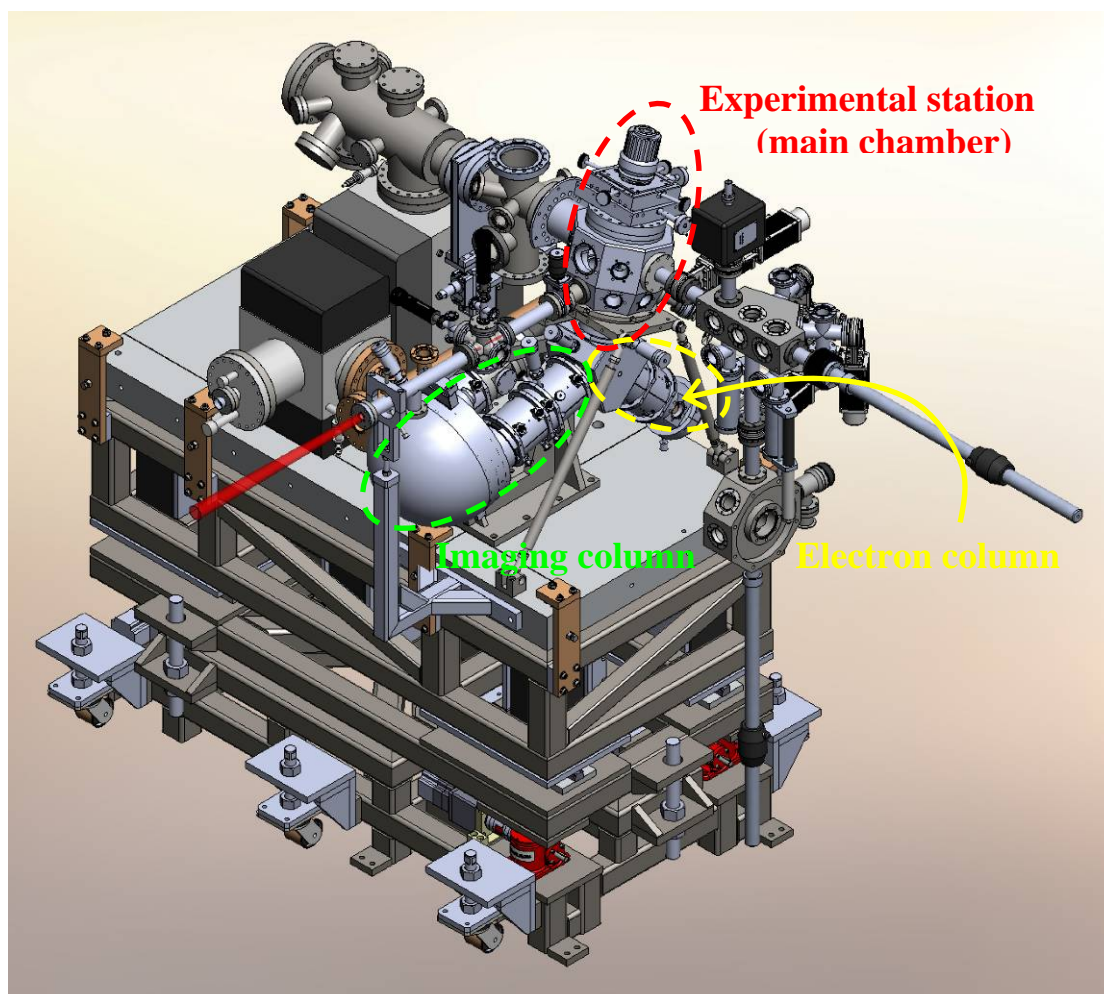
Figure 4.3 The 3D drawing of the PEEM experimental station of BL3.2b. Synchrotron light beam is indicated by the red arrow.
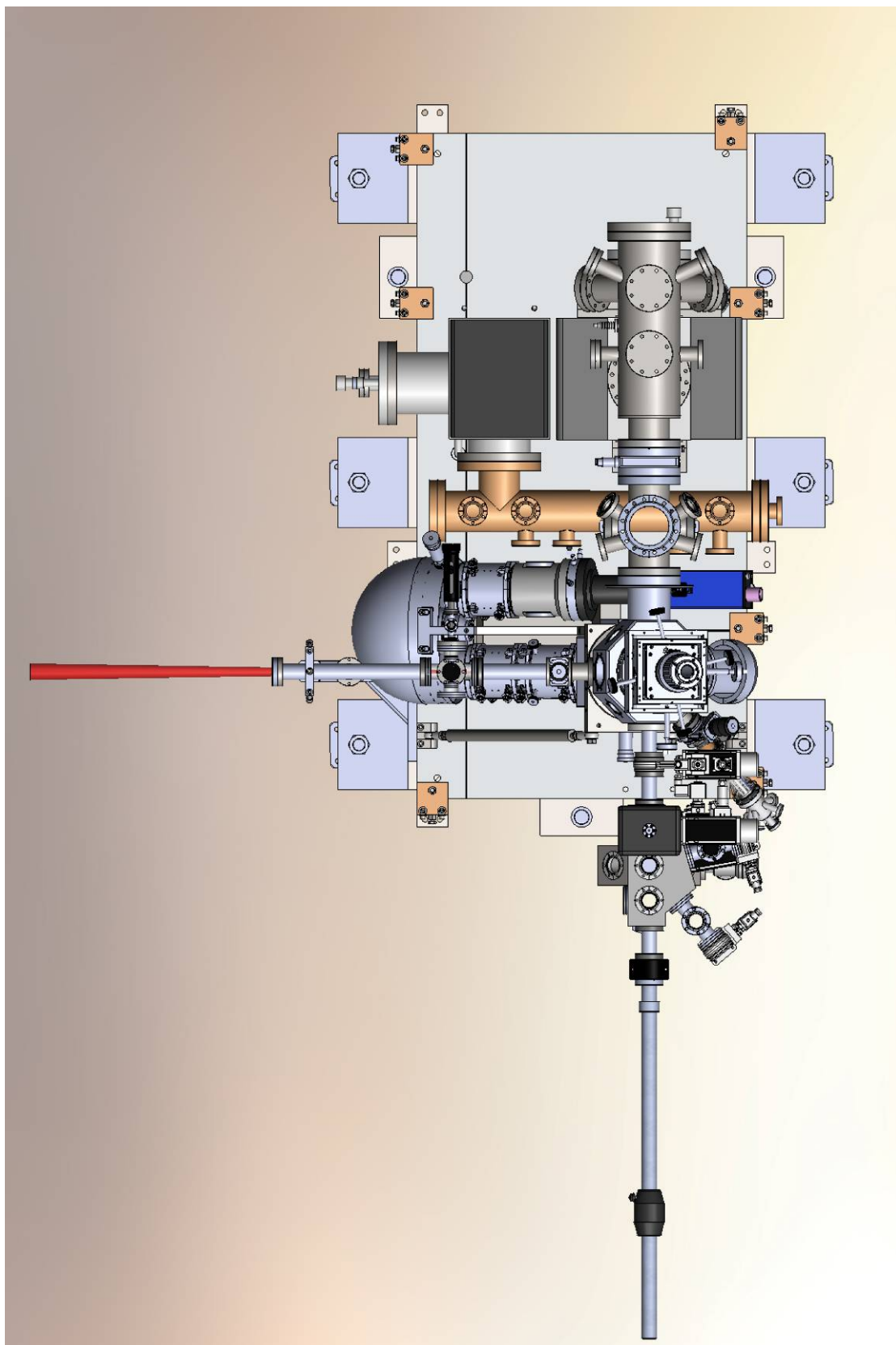
Figure 4.4   Top view of the PEEM experimental station of BL3.2b.

4.3 Commissioning results

Figures 4.5 and 4.6 show the photos of the PEEM experimental station before and after installing at the BL3.2b. A flexible tube, a 40DN corrugated bellow, is used at the connection between the beamline and the PEEM experimental station. This allows the experimental station to be moved to align the microscope in a correct orientation with respect to the synchrotron light beam. This is not the case when a UV lamp is used since it is easier to do the alignment by moving the UV lamp.
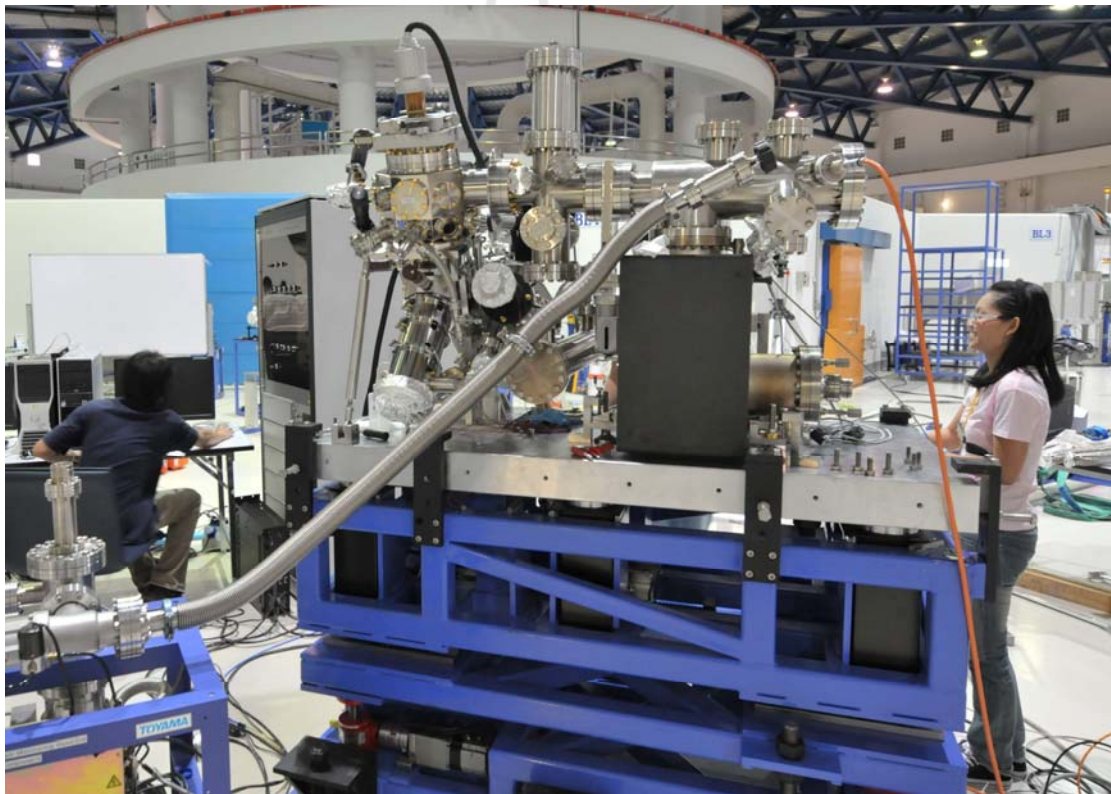
Figure 4.5 Photo of the PEEM experimental station before connecting to the beamline.
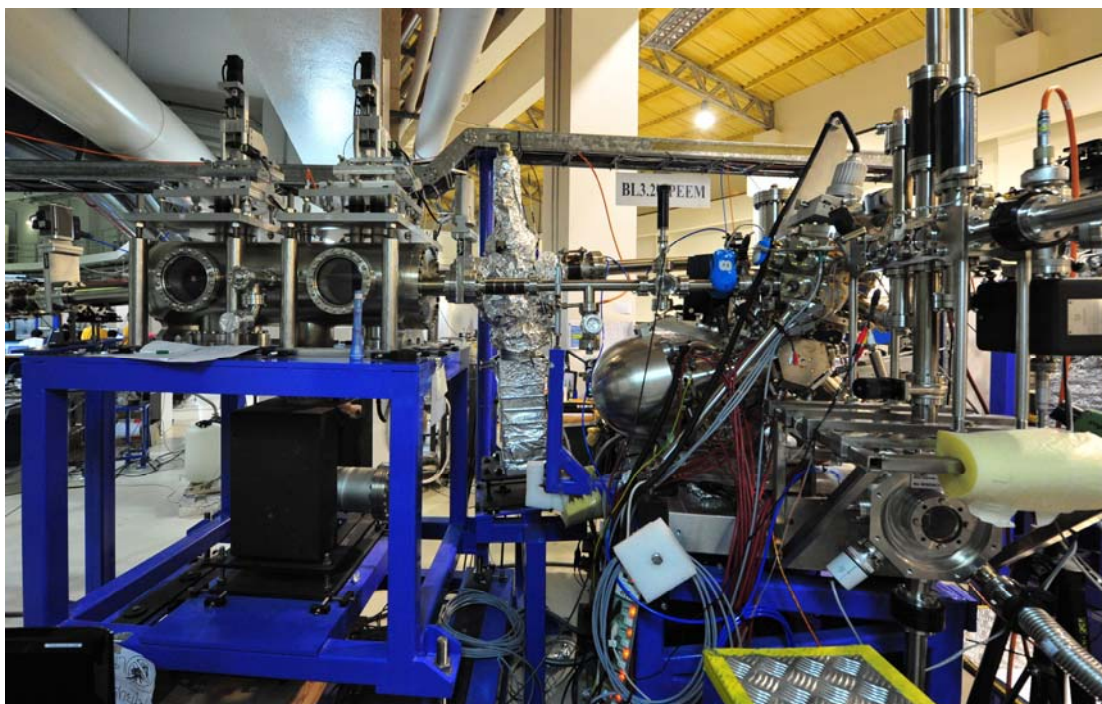
Figure 4.6   Photo of the PEEM experimental beamline installed at BL3.2b.

The base pressure in the main chamber of the microscope is less than 2×10^{-10} Torr. During PEEM observation, when the sample is biased with high voltage of -20 kV, the pressure is raised to about 1×10^{-10} Torr for the sample with low outgassing rate. Higher pressure is expected for samples with high outgassing rate. Normally, the gate valve between the main chamber of the microscope and the big preparation chamber is kept opened so the main chamber can be evacuated. The base pressure in the small preparation system is typically 1×10^{-8} Torr. It can be higher during degassing samples.

The introduction of the sample thru the load-lock system has been tested. The sample can be transferred from the load-lock chamber to the sample preparation chamber without breaking a UHV condition in the preparation chamber. Since the pressure in the preparation is already low, typically 1×10^{-8} Torr, transferring the

sample into the main chamber can be done without worrying about breaking the UHV conditions in the main chamber.

Figure 4.7 shows the drain current measured by a gold mesh located in front of the PEEM experimental station. The drain current is proportional to the photon flux delivered by BL3.2. The photon flux for the low energy region of the BL3.2 monochromator, 40-160 eV, is about 2-5 orders of magnitude higher that the high energy region of the BL3.2 monochromator. This is mainly due to the fact that this low energy region is from the 1st order radiation of the U60 planar undulator. For the high energy region, it is necessary to employ higher harmonic light.

The drain current measurements also show that, obviously, there are contaminations on the optical elements of the beamline. The structures near the photon energy of 570 eV correspond to Cr L_2 and L_3-edges (583.8 and 574.1 eV). These chromium atoms are widely known to be present in the coating of the optical elements. Carbon contamination in beamlines is found in all beamlines. This is also true for BL3.2, in which the contamination can be seen clearly as a big dip in the drain current measurements at about 285 eV. Carbon contamination on the gold mesh is also expected, and that might lead to an inaccurate value of the drain current. To get accurate value photon flux of this beamline, extensive work is still required.

The support of the PEEM experimental station was found to be very station. Because of a solid foundation of the experimental hall of the Siam Photon Laboratory, mechanical vibration noises, e.g. vibration from surrounding pumps, were not observed during PEEM and LEEM measurements. The anti-vibration system of the table was found to be not necessary. The moments of the table for aligning the microscope to the synchrotron light beam works as designed.
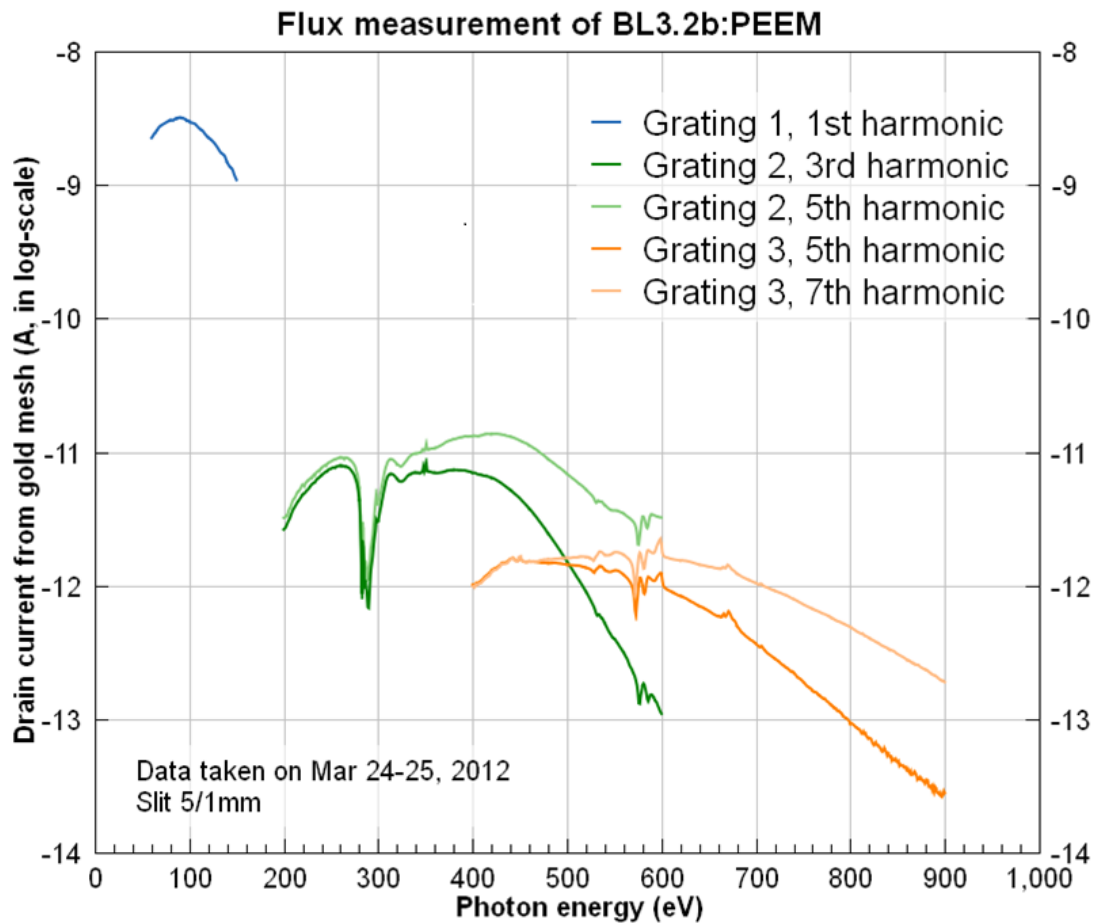
Figure 4.7 The drain current measured from a gold mesh located in front of the PEEM experimental station. It is used for monitoring the monochromatic light beam entering into the microscope.

4.4 References

Bertolo, M., Gregoratti, L., Heun, S., Kaulich, B. and Kiskinova, M. (2003). X-ray spectromicroscopy with synchrotron radiation: Approaches and Applications. **Science, Technology and Education of Microscopy**: an Overview. (pp 676-686). Editor A. Mendez-Vilas FORMATEX.

Mathieu, C., Barrett, N., Rault, J., Mi, Y. Y., Zhang, B., de Heer, W. A., Berger, C., Conrad, E. H. and Renault, O. (2011). Microscopic correlation between chemical and electronic states in epitaxial graphene on $SiC(000\bar{1})$. **Phys. Rev. B** 83: 235436 1-11.

Rempfer, G.F., Desloge, D. M., Skoczylas, W. P. and Griffith, O. H. (1997) Simultaneous correction of spherical and chromatic aberrations with an electron mirror: An electron optical achromat. **Microanal** 3: 14-27.

Wichtendahl, R., Fink, R., Kuhlenbeck, H., Preikszas D., Rose, H., Spehr, R., Hartel P., Engel, W., Schlögl, R., Freund, H. J., Bradshaw, A. M., Lilienkamp, G., Schmidt Th., Bauer E., Benner, G. and Umbach, E. (1998). SMART: An Aberration-Corrected XPEEM/LEEM with Energy Filter. **Surf. Rev. Lett**. 6: 1249-1256.

CHAPTER V

EXPERIMENTAL RSULTS AND DISCUSSIONS

This chapter presents the first experimental results from the PEEM experimental station of BL3.2b. Epitaxial graphene was synthesized by thermal decomposition of a single crystalline SiC in the PEEM experimental station. The experimental station was an ideal for such study since the sample annealing at high temperatures could be achieved in this system. In addition, surface reconstruction of SiC and the graphene could also be monitored by electron diffraction pattern. IV-LEEM also provides a method to determine the number of graphene layers easily. Detailed experimental results and discussions are given below.

5.1 Surface topography of SiC: AFM observation

In this work, single crystalline SiC(0001) samples were used as starting material for synthesizing expitaxial graphene. The surface topography of the SiC samples was examined by AFM. Figure 5.1 shows AMF images of the as-received 6H-SiC(0001) taken in a tapping mode illustrated in four differenct types of imaging techniques (Height, Phase, Ampliture, and Zsensor imaging). The area of the scanning is 1×1 μm^2. The images were taken with a scanning rate of 1 kHz. The scratches on the SiC surface are clearly visible in all four types of imaging techniques.
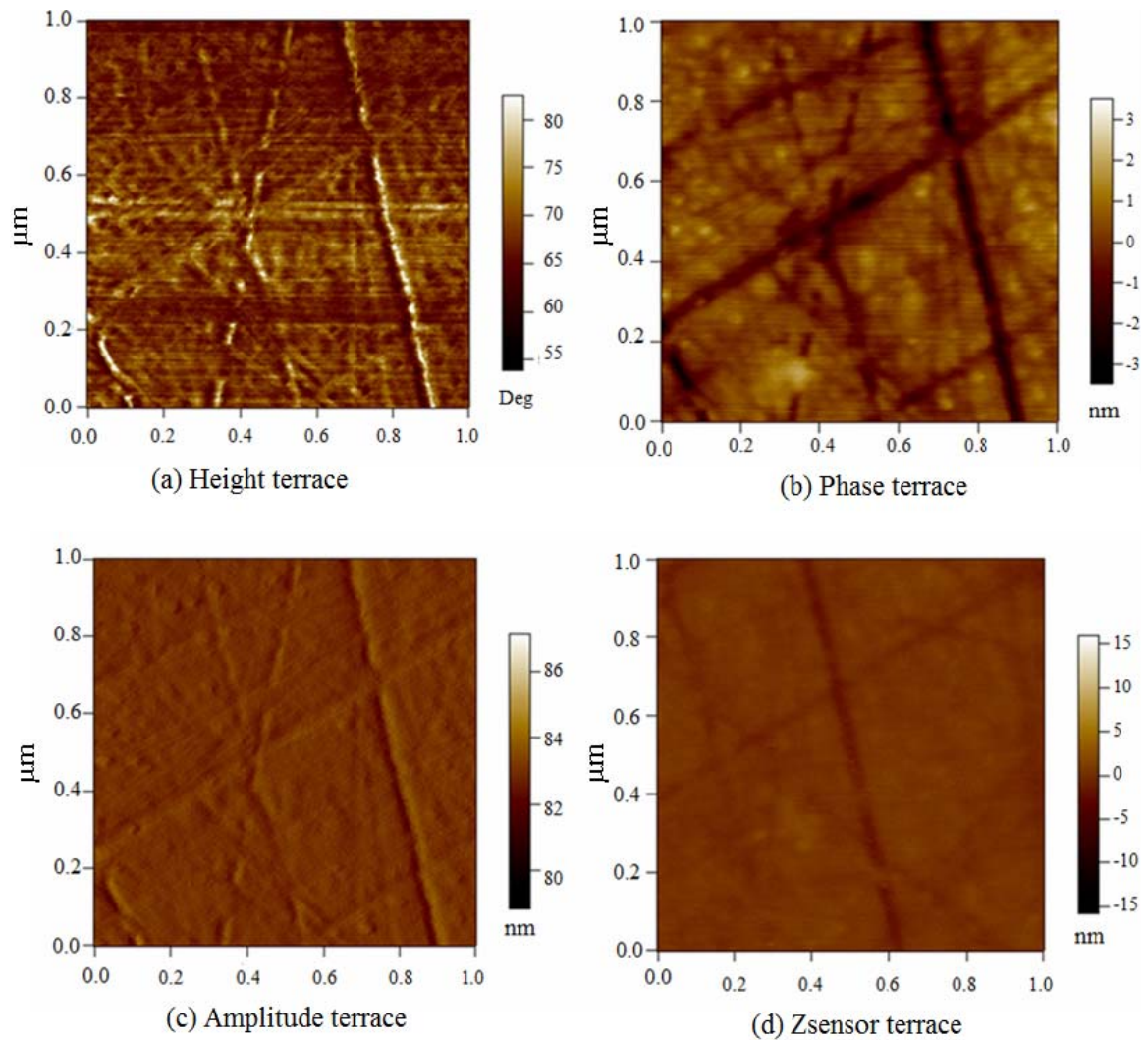
Figure 5.1 AFM topography of a SiC(0001) sigle crystal taken in a tapping mode. The area of the images is 1×1 μm².

From a larger scanning area, the grooves and the roughness of the as-received SiC sample were analyzed. Figure 5.2 shows the line scan of the SiC sample with an area of 10×10 μm². The mximum depth of the grooves was found to be as deep as 5 nm. The RMS roughness over the entire image was estimated to be about 1.3 nm.
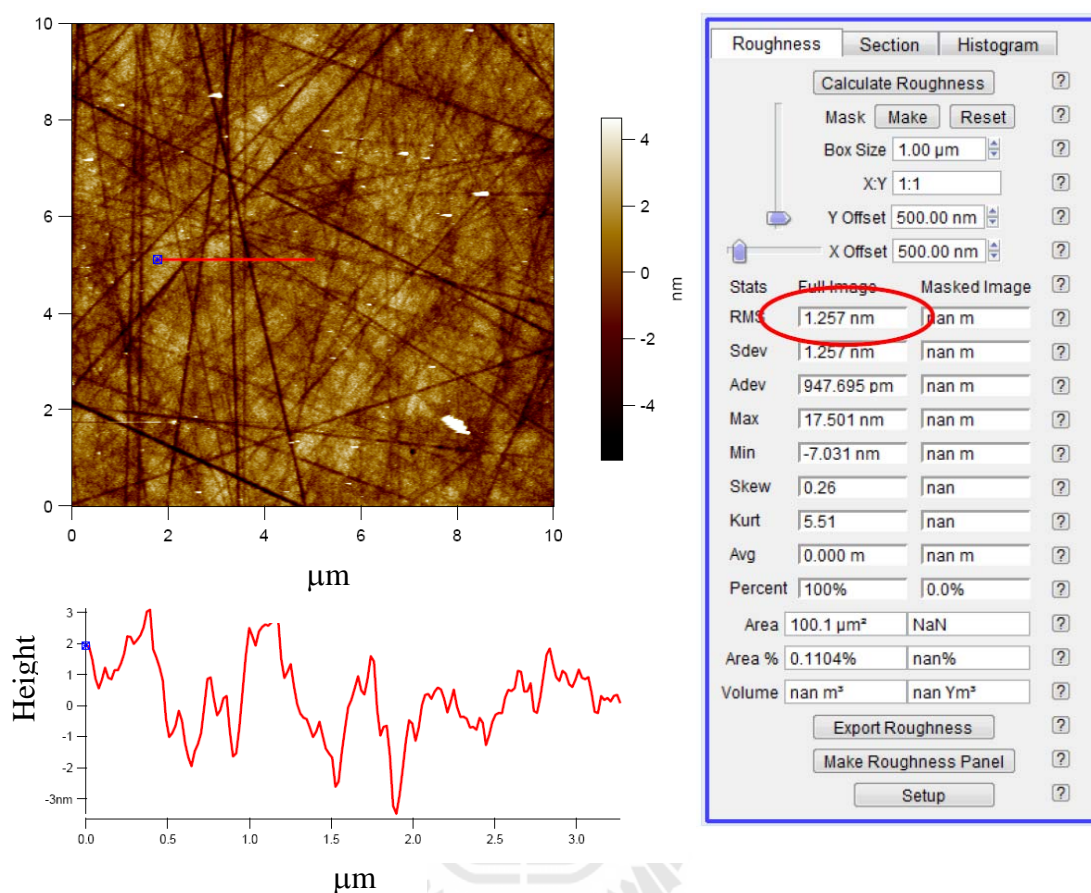
Figure 5.2 The line scan of 10×10 μm² measurement indicates the surface grooves with a maxumum depth of 5 nm. The RMS roughness over the entire image was about 1.3 nm.

5.2 Thermal decomposition of SiC

After chemical cleaning procedures, a single-crystalline 6H-SiC(0001) sample was introduced into the PEEM experimental station through the load-lock system. The sample was then degassed at 500 °C overnight. The temperature during the heat treatment was monitored by the infrared pyrometer together with the WRe thermocouple (C-type) welded to the sample cartridge. Removing of oxide layer was

carried out by flashing the sample at flashing temperature above 1000 °C. It should be noted that flashing introduced large amount of gas molecules giving rise to the increase of vacuum pressure in the microscope. Thus to actually obtain flashing at 1200 °C to remove oxide layer, several flashings were required. LEEM images of the sample were taken after flashing, and shown in Figure 5.3. These LEEM images in Figure 5.3 were capture by apply the current 1388.8 mA to the objective lens for the appropriated focus images and bias the objective lens and the sample with the start voltage 2.03, 1.53, 1.73, 1.73, 1.85 and 1.48 V for 77, 50, 25, 15, 10 and 7.5 µm FOVs, respectively. LEEM images in a mirror mode are also illustrated at the second row in Figure 5.3.
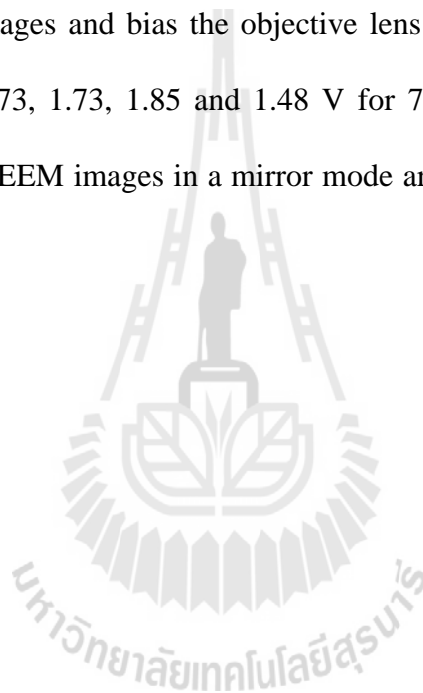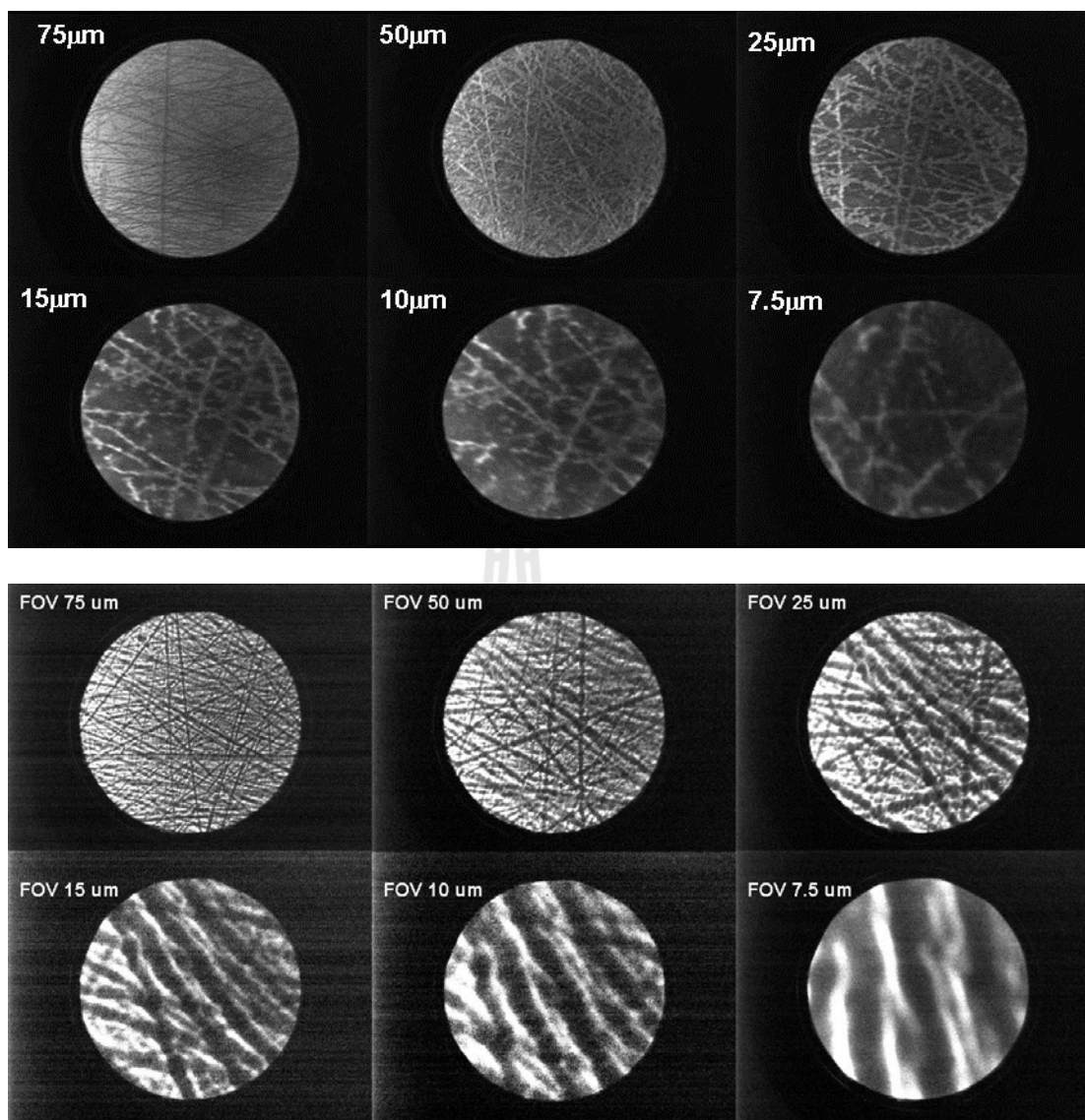
Figure 5.3   The two top rows show LEEM images of SiC(0001) surface at different field-of-views (FOV) after flashing SiC(0001) at 1200 °C. The two bottom rows are examples for LEEM images in a mirror mode obtained by setting the start voltage to be a negative value close to zero V.

After removing the oxide overlayer, thermal decomposition of SiC to form graphene were carried out done by annealing the substrate around 1300 °C for 1 minute. As mentioned before in Chapter II, the surface reconstruction of SiC in the early stage for graphitization can be monitored by observing LEED pattern (Bostwick, 2008), thus LEED pattern observations were carried out after each heat treatment. Figure 5.4 (a)-(d) shows the LEED patterns taken from the SiC sample after a sequent flashing at 1000 °C, 1200 °C, 1300 °C and 1400 °C, respectively.
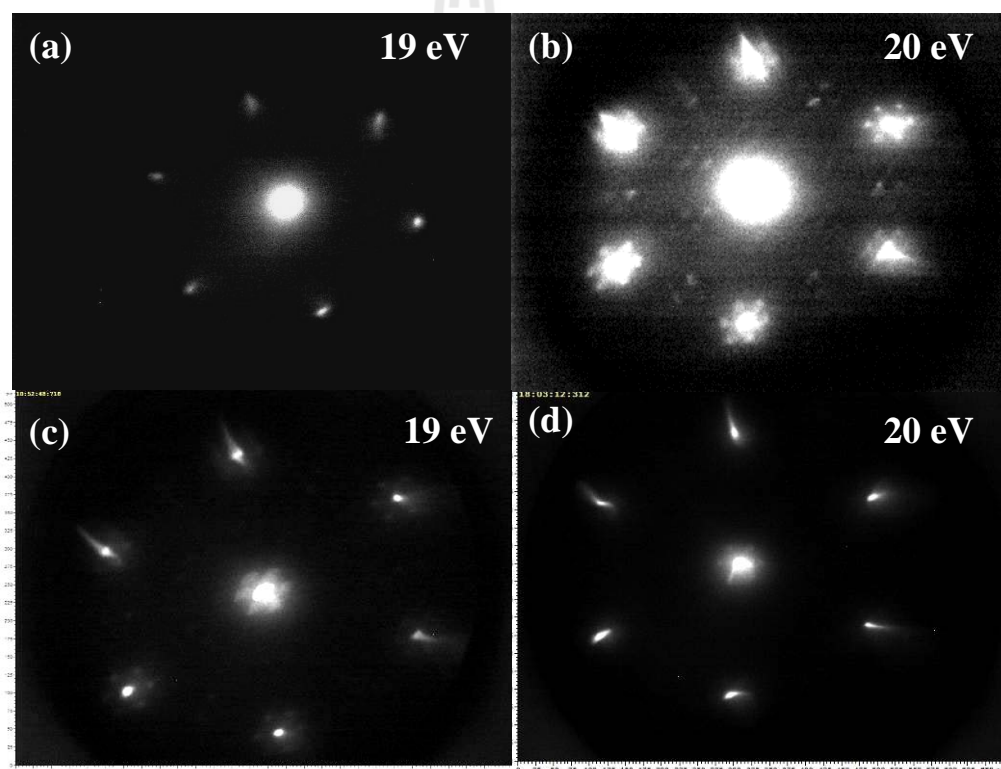
Figure 5.4 LEED images of the SiC sample in a sequent flashing process: (a) after flashing at 1000 °C (b) followed by flashing at 1200 °C (c) followed by flashing at 1300 °C (d) followed by flashing at 1400 °C, respectively.

Early LEED study on the path way to from graphite by thermal decomposition of 6H-SiC(0001) by Bostwick, et al. (2008) suggested the evolution of the LEED pattern caused by surface reconstruction/decomposition upon thermal treatment as described following; for the clean surface of 6H-SiC(0001), the LEED pattern exhibits a Si-rich (3×3) structure. Further annealing around 1050 °C, Si atoms are removed and thus the ($\sqrt{3}$×$\sqrt{3}$) R30° structure is formed. Before the epitaxial graphene growth, the LEED pattern observed the carbon rich ($6\sqrt{3}$×$6\sqrt{3}$) R30° structure at 1150 °C (so-called 'the buffer layer') which is the precursor to graphene growth. Further annealing leads to growth of graphene and few layers graphene (FLG) with (1×1) periodicity of graphite. When the annealing temperature is above 1400°C, the graphite is formed.

In this work, a clean and well-ordered surface structure of the 6H-SiC(0001) sample was obtained after flashing at 1000C, indicating the LEED pattern of Si-rich ($\sqrt{3}$×$\sqrt{3}$) R30° structure, as shown in Figure 5. 4(a). The early stage (buffer layer) before first graphene layer was grown on the substrate could be observed after flashing the SiC sample to 1200 °C, as shown in Figure 5.4 (b). The graphene was expected after flashing at 1300 °C. Further flashing at 1400 °C would lead to the increase of the number of graphene layers and thereby the formation of graphite as shown in Figures 5.4 (c) and (d).

LEEM images of the SiC sample were taken after flashing at 1300°C. The images with different FOVs are shown in Figure 5.5. The LEEM images were captured with the current for the objective lens of 1602 mA and with the start voltages of 0.39, 0.03, 0.08, 0.36, 0.50 and 0.77 for the 75, 50, 25, 15, 10 and 7.5 μm FOVs,

respectively. Figure 5.6 shows also the LEEM images of the SiC after flashing at 1400 °C. The scratches are clearly visible in both heat-treated conditions. It should be noted that flashing of the sample was performed with care, so that the pressure rise did not exceed 5×10^{-8} Torr .
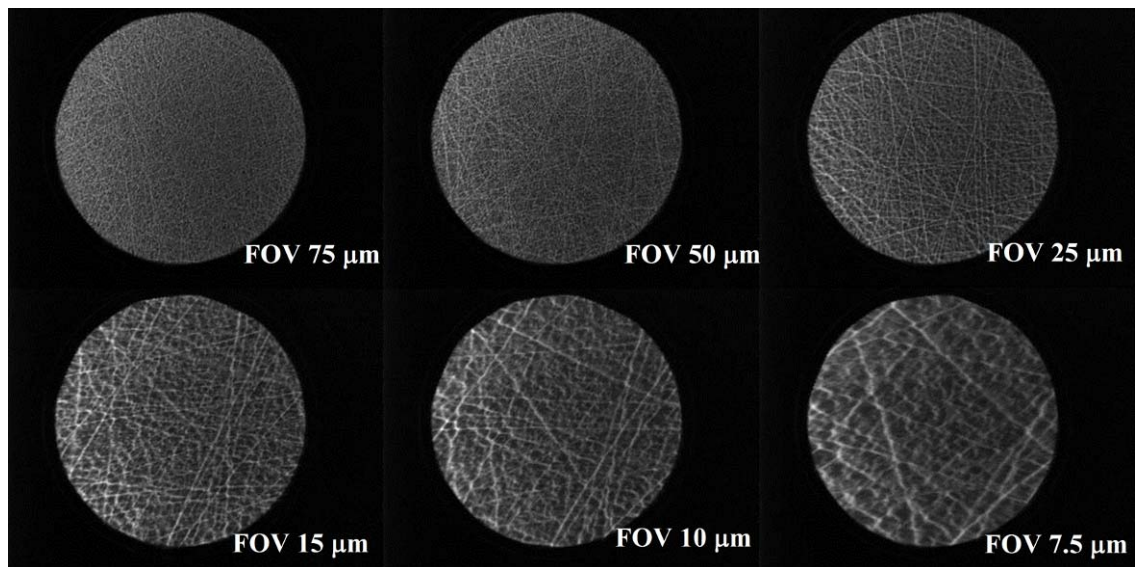
Figure 5.5 LEEM images after annealing 6H-SiC(0001) at 1300 °C for 1 min (FOV = 75, 50, 25, 15, 10 and 7.5 μm).
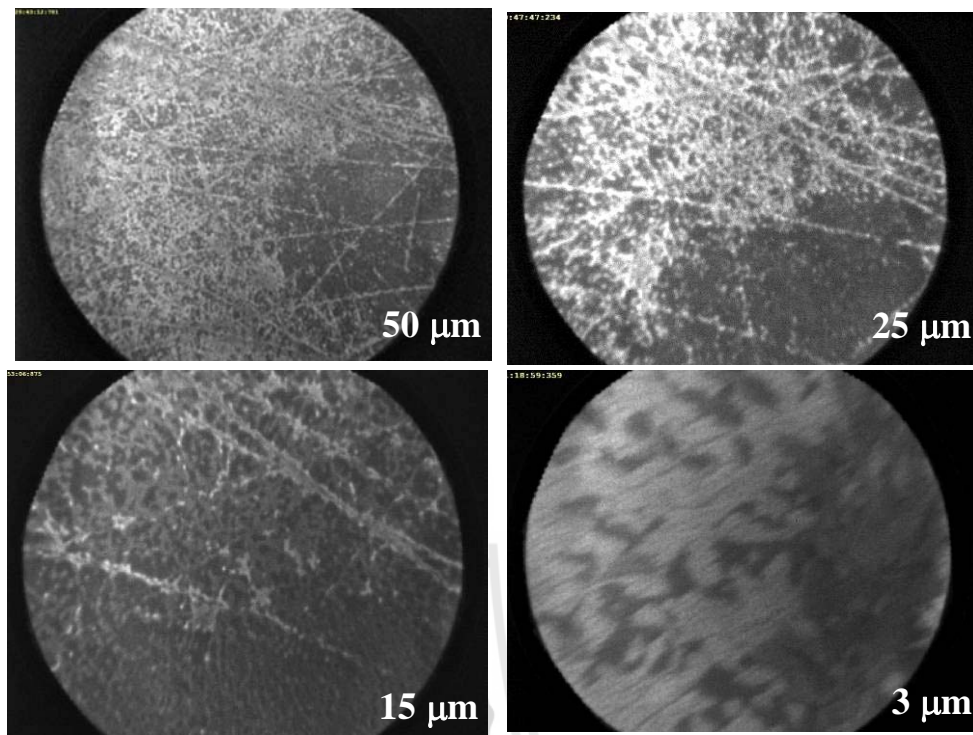
Figure 5.6 LEEM images of 6H-SiC(0001) after flashing at 1400 °C exhibiting more contrast between the scratch lines and other non-scratch areas (FOV = 50, 25, 15 and 3 μm).

5.3 Determination of number of graphene layer by IV-LEEM

The oscillations in the LEEM reflectivity at low electron energies can be used to identify the number layers of graphene as reported by several groups i.e., Chung et al. (2003), Hibino et al. (2008), and Ohta et al. (2008). The information on the number of graphene layers is contained in the oscillating intensity of reflecting electron as a function of the bias voltage of the sample, or known as IV LEEM analysis. The electrons with certain discrete energy levels are allowed inside the quantum well potential as describe by Hibino et al. (2008) and Virojanadara et al. (2008, 2010). According to these discrete energy levels, incident electrons with various energies

will get reflected differently, creating an oscillating I-V spectrum related with the particular graphene thickness. Hibino et al. point out that the conduction band of graphite along the Γ-A direction is continuous though a few layer graphene should have discrete states related from the reflectivity oscillation of electron structure of the thin films provided the quantized conduction band states. A supporting theory is given by Mathieu et al. (2011) based on a tight-binding calculation of the resonant energies analogous with the experimental minima positions.

In this work, a series of LEEM images were taken with a variation of electron energies to determine the number of graphene layers. It is noted that the electron energy can be varied by changing the bias voltage of the sample in the LEEM system. Figure 5.7 (a) shows a 10-μm-FOV LEEM image of the SiC sample after flashing at 1400 °C. The intensity of regions of interest (ROI) indicated by the labels S1, S2, L211, White and Dark deduced from the series of the images was plotted against the electron energy in Figure 5.7 (b). The numbers of dips in the IV-LEEM curves in Figure 5.7 (b) are the number of graphene layer. It was found that the numbers of graphene layers formed varied from 2 to 4 layers.
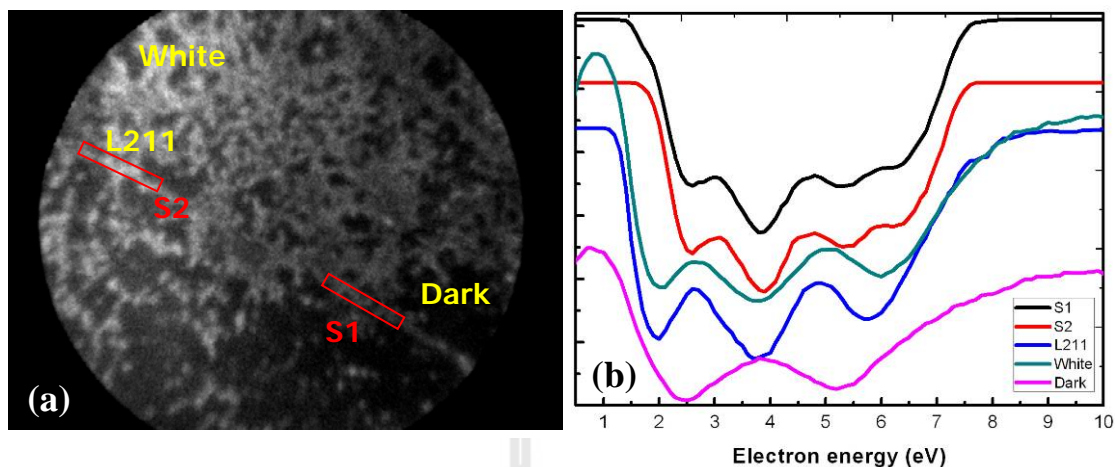
Figure 5.7 (a) The 10-µm-FOV LEEM image of graphene/6H-SiC(0001) and, (b) the IV-LEEM curves showing the oscillation dip of the intensity deduced from different regions on the sample surface, as indicated by.S1, S2, L211, White and Dark.

It is interesting to point out that there is a variation of the number of graphene form on a SiC sample. Figure 5.8 (a) shows that the number of graphene layers was found to be 2 in the dark regions of the LEEM image. In the bright regions of the LEEM image, the number of graphene layer was found to be either 3 or 4 layers, as shown in Figure 5.8 (b).

It is interesting to find out the variation of the number of graphene layers and its cause. To carry out more detailed investigations, IV LEEM curves were carefully extracted from various regions of interest. It was found out that the scratch on the sample surface might be the cause for the variation. Careful analysis of LEEM images was carried out. Figures 5.9 (a)-(f) show the LEEM images of graphene formed on the SiC substrate after the thermal decomposition at 1400 °C. By varying the "start voltage" or the energy of the electrons arriving at the sample surface, LEEM images

exhibited the contrast between the scratch surfaces represented as the bright/white area while the other represented as the dark area (flat surface).
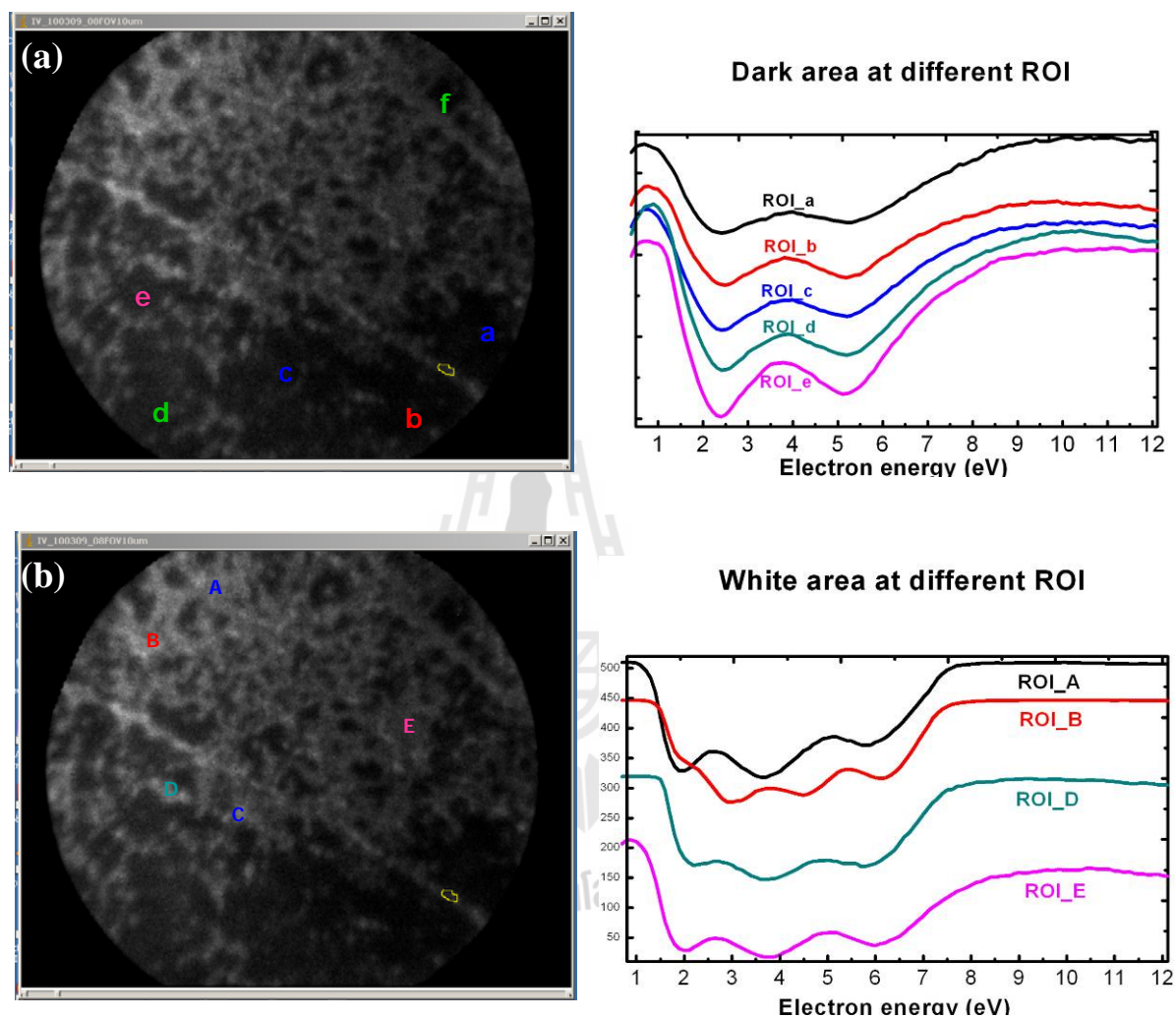
Figure 5.8 (a) LEEM image and LEEM-IV curves deduced from the dark regions indicated by letter a, b, c, d and e in the LEEM image (b) LEEM image and LEEM-IV curves deduced from the white regions indicated by letter A, B, D and E in the LEEM image.
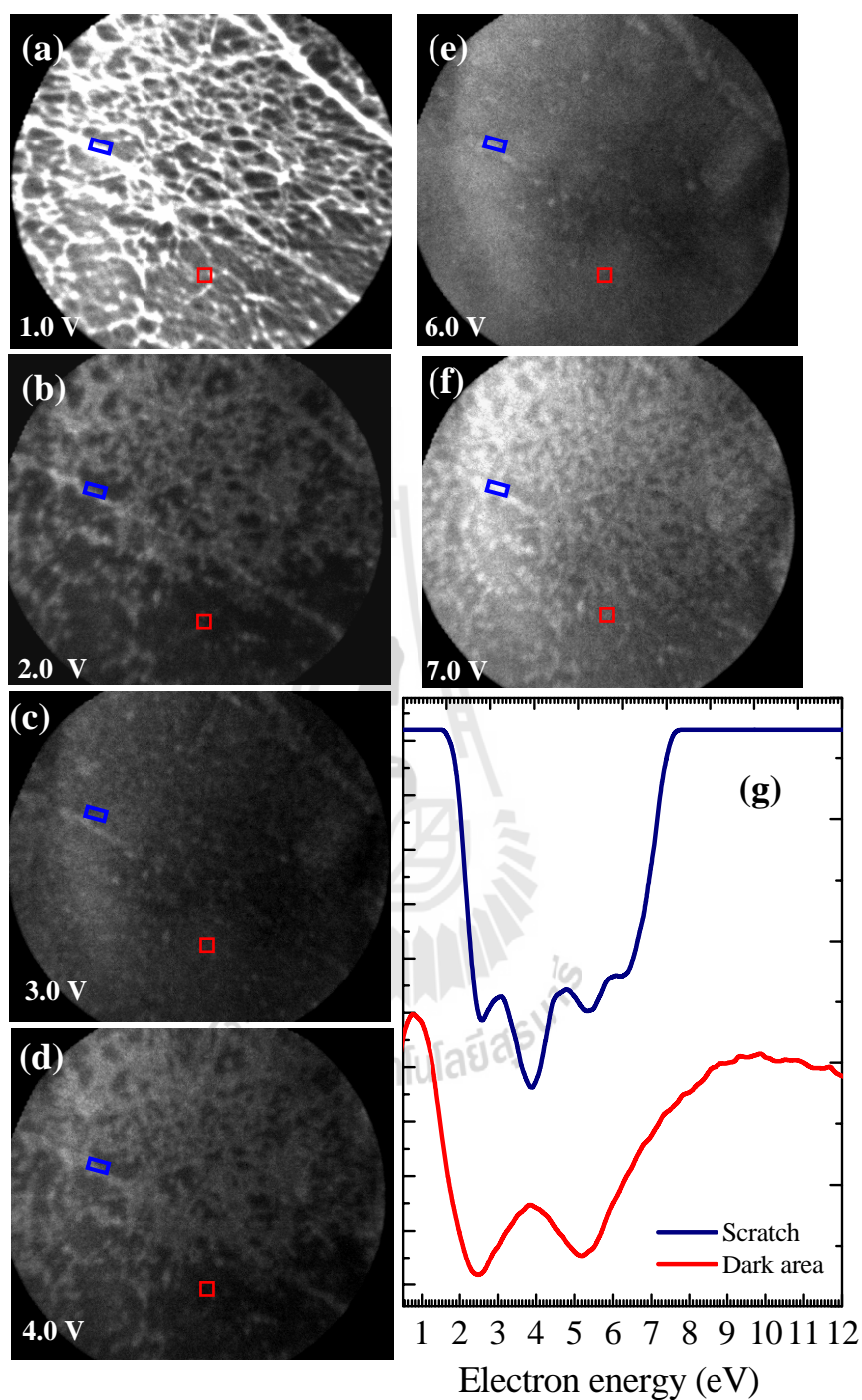
Figure 5.9 25-μm-FOV LEEM images of the graphene grown on the scratched SiC substrate at bias voltages varying from 1.0 - 7.0 eV for Figures (a)-(f), respectively. The corresponding LEEM-IV curves for the region of interested indicated by a square symbols marked with blue and red color are shown in Figure (g).

However, these high and low intensities of the LEEM images do not originate from the topography contrast, as to the LEEM technique also picks up the contrast from the electronic structure at the surface. Figure 5.9 (b) show that the scratch marks are mostly visible along high-intensity lines and the flat regions are mostly in low-intensity areas. As the electron energy is varied, the contrast of the LEEM image changes dramatically; at some energy i.e., 3 eV in Figure 5.9 (c), some of the scratch marks are barely visible. This can be explained by the quantum well states of graphene layer on SiC substrate since the change of the image intensity as a function of bias voltage is set by the electronic structure as mentioned above. Figure 5.9 (g) is the intensity oscillations when the bias voltages vary in the same range with Hibino, et al. (2008) collect from the two selected spots (blue and red squares in panel (a) – (f)). The number of dip in this oscillation indicated the number of graphene layers at that spot. The scratch line, blue spot, has s 4 dips oscillations, while the flat area, red spot, indicating the 2 dips regarding with the 4(2) layers of graphene on the selected blue(red) spot. Therefore, the smooth areas are mostly covered with two layers of graphene as demonstrated by the IV-LEEM express mostly only two dips. This is confirmed by a good agreement with Norimatsu and Kusunoki (2010), Choi, Lee and Kim (2010) and Tanaka et al. (2010) that scratches on the SiC surface can promote the enhanced growth of graphene and these studies also demonstrated that the graphitization process usually starts near the step of a surface rather than flat terraces. Moreover, Tanaka, Morita and Hibino (2010) also describe "step" on substrates as the kicker of graphene nucleation by providing Carbon atoms. It is note that although this study, the IV-LEEM analysis, can not tell whether the additional layers are on top or underneath the buffer layer, but it is speculated that the additional layers are

underneath based on the model described by Norimatsu et al. (2010). From this reason, the AFM is performed to measure the width of the scratches on the as received SiC substrate as well as the graphene width from along the scratch line will be investigated in detailed.

5.4 Effect of surface scratch on graphene width

In order to investigate the effect that substrate scratch have on the spatial variation of graphene layers form on 6H-SiC(0001) surface, the native scratch width are examined by AFM. Figure 5.10 shows the selected regions on the surface where the width of the scratches were analyzed by Igor Pro software. An example for the scratch width analysis by Igor Pro software is demonstrated in Figure 5.10 (a). It is noted that the image is rotated so that the scratch line is in the vertical direction as shown in Figure 5.10 (b). There are 8 regions of interest marked by "afm1", "afm2", "afm3", …., "afm8". These regions of interest are selected for surface width analysis by Igor Pro software as illustrated in Figure 5.10 (a). Before analyzing the scratch width, the images are magnified as shown in the small panel between (a) and (b). Figure 5.10 (c) is an example for scratch width measurement by pick up 4 lines selected from the region marked by "afm2" in Figure 5.1 0(a), and the corresponding width of the scratch are presented in Figure 5.10 (d). Both the depth profiles along the perpendicular direction of the scratch line and the full width of these profiles are measured. In addition, the Gwyddion software also used to measure the scratch width as demonstrated in Figure 5.11 (a)-(d). Figure 5.11 (a) shows the scratch line and the corresponding line profile obtained from by using the Gwyddion software as indicated

by 1-13. Figure 5.11 (b) presents the step height fit function used for fitting the scratch width. Figure 5.11 (c)-(d) are examples for the scratch width for line profile 4, and 11, respectively. The corresponding widths analyzed by Gwyddion software are 0.1017 μm, 0.1632 μm. The results from both software analysis indicated that the scratch width collected in many lines is about 0.20 ± 0.05 μm.
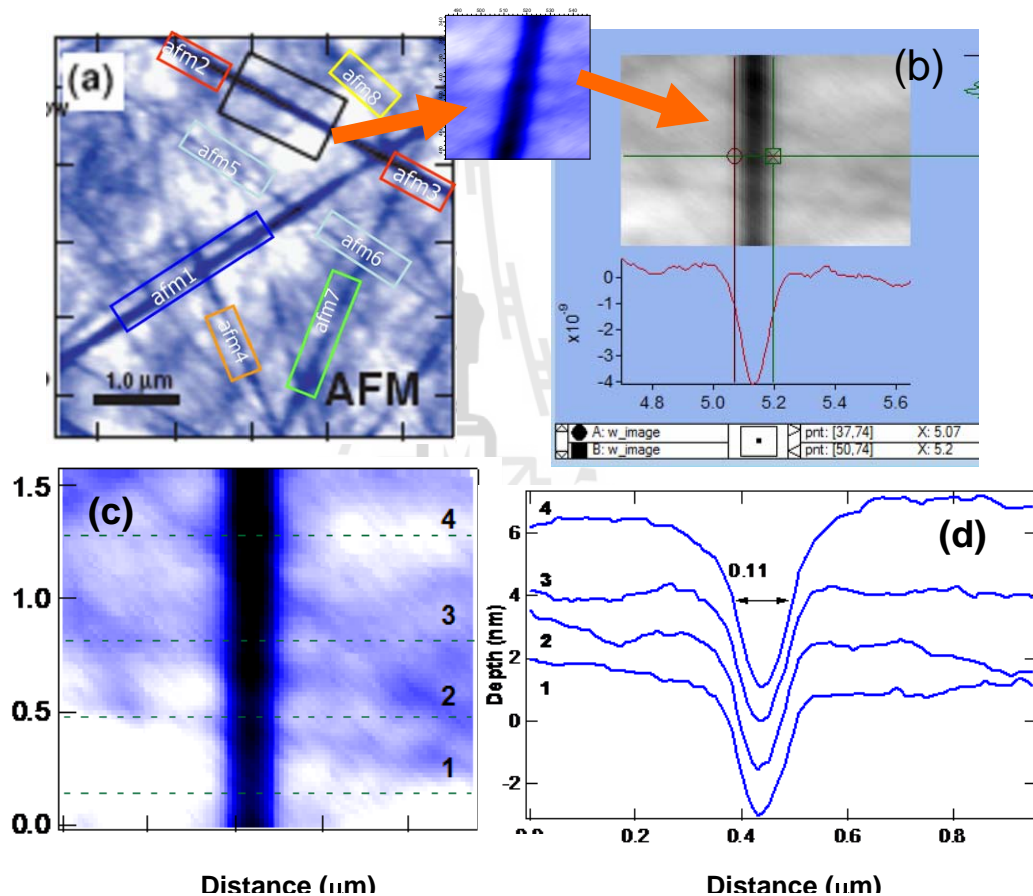
Figure 5.10 AFM image of a single crystalline SiC (as-received, before any chemical and heat treatment) showing the scratches and their width. (a) selected areas analyzed by Igor Pro software (b) enlarged image from the area of interested showing measurement of the width (c) enlarged image from area "afm8" (d) the scratch width taken from area "afm8" at different locations
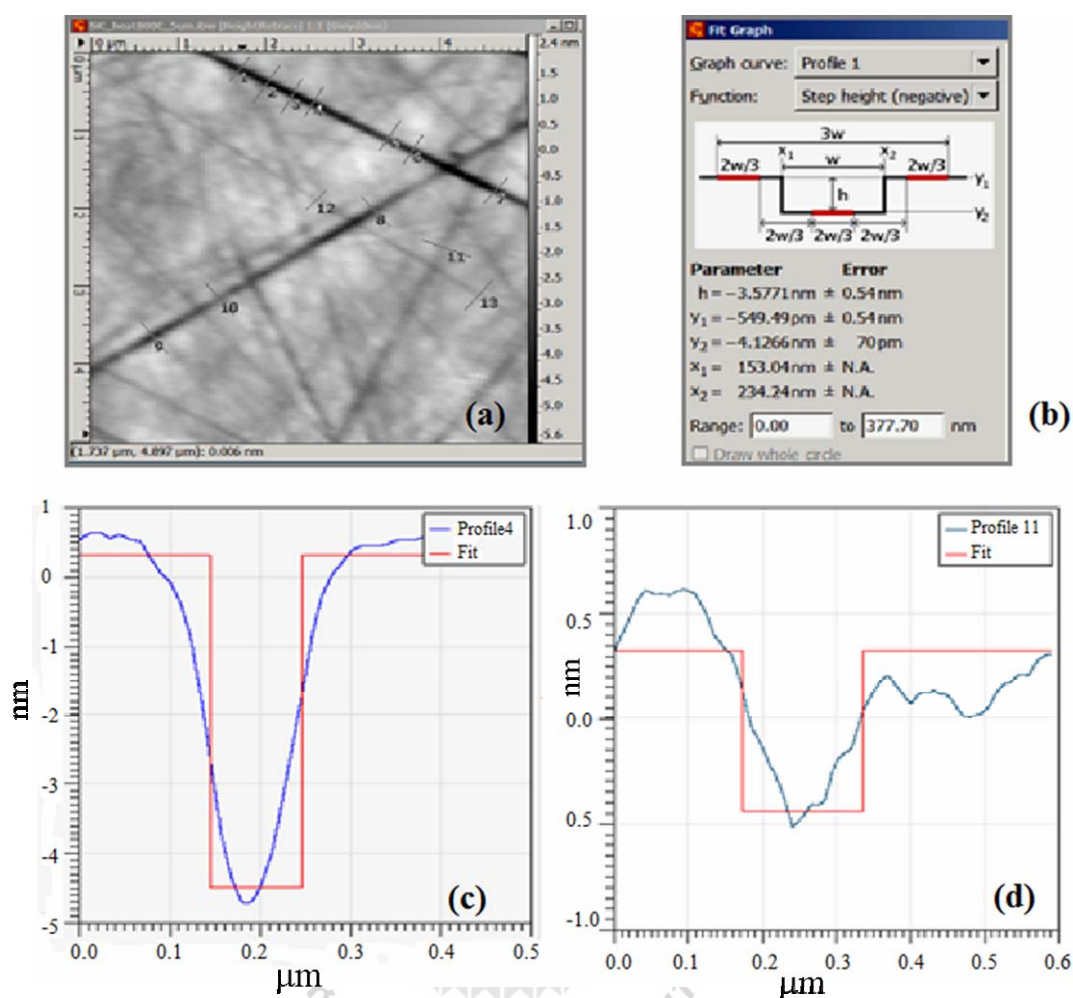
Figure 5.11 Scratch width measurement from Gwyddion software (a) the selected scratch line, (b) function to fit the scratch width, (c) and (d) the examples for scratch width profile and the related step height fit.

From the analysis of AFM images using Igor Pro and Gwyddion software implies that the scratch lines have a wedge shape as illustrated in Figures 5.10 and 5.11. The same software and procedures were used for the analysis of LEEM images after the thermal decomposition. In LEEM observation, maximum image contrast between the graphene domains in the vicinity of the scratches and the flat area was

obtained when the bias voltage was about 1.6 V as shown in Figures 5.12 (a) and 5.13 (a). These graphene layers were already examined with the IV-LEEM and found to be 3-4 layers along the scratch direction. Figure 5.12 (a) and Figure 5.13 show the widths of the graphene extracted from the contrast profile analyzed by using Gwyddion and Igor Pro software. Figure 5.12 (a) shows the LEEM image and the selected profile line for Gwyddion measurement indicated by number 1-10. The step height function fit for graphene width measurement is presented in Figure 5.12 (b) that provided the graphene width of 0. 4593 μm for the line profile 9, and graphene width for the line profiles 8 and 5 are 0.4420 and 0.7963 μm are shown in Figure 5.12 (c) and (d), respectively. The results obtained from Igor Pro software are also presented in Figure 5.13. The average value of this width is 0.52±0.07 μm, which is approximately 2.6 times larger than the average scratch width from Figures 5.10 and 5.11. By comparing these extracted widths between the scratch lines and the graphene formed along its scratch, it is obvious that the enhanced growth of graphene can extend much further from the edge of a scratch, which is simply shown by the schematic picture in Figure 5.14.
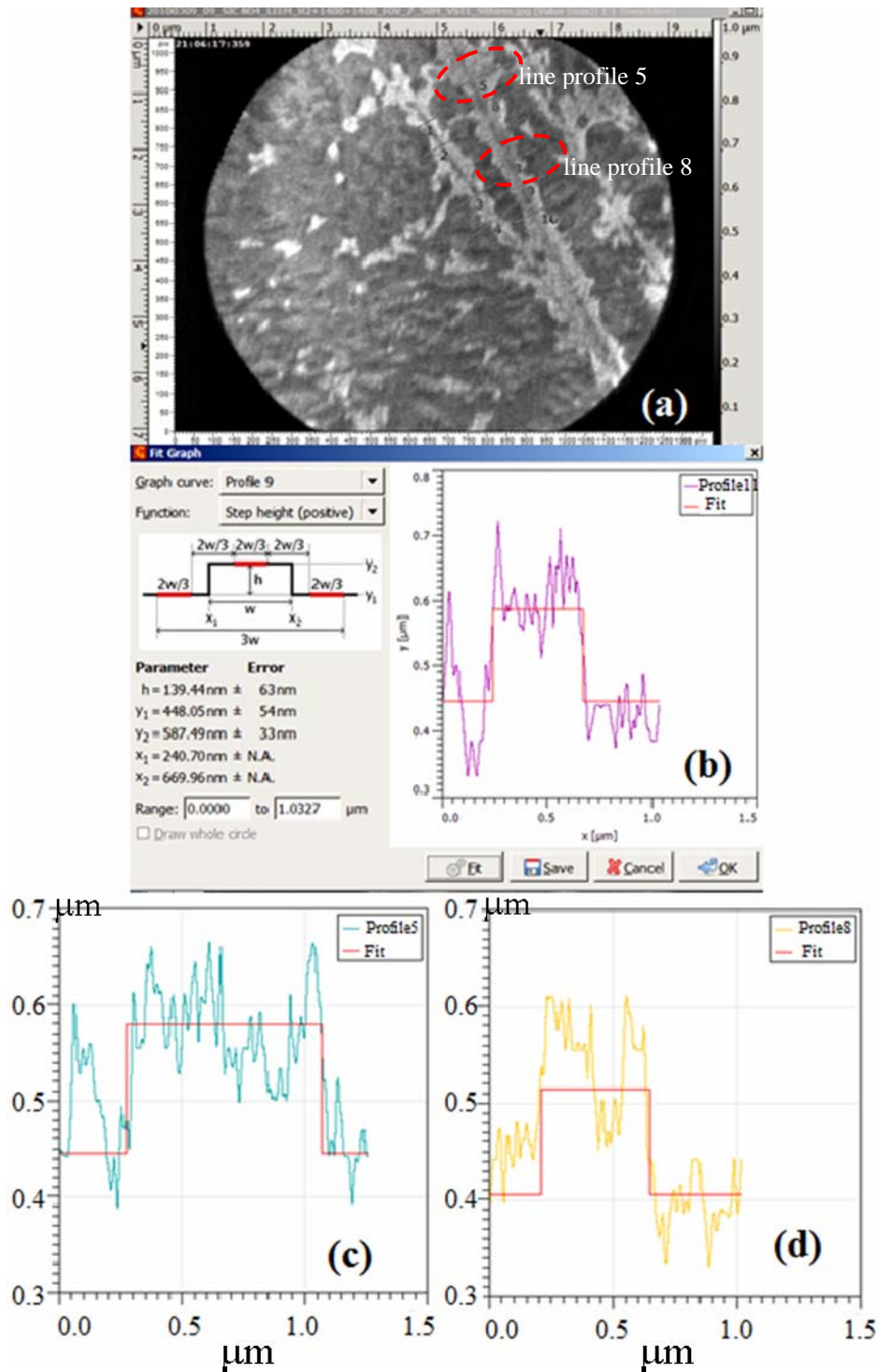
Figure 5.12 Graphene width measurements by using Gwyddion software, (a) LEEM image of graphene formed along the scratch line, (b) the step height function for fit the graphene width, (c) and (d) the line profiles 5 and 8 as shown in (a).
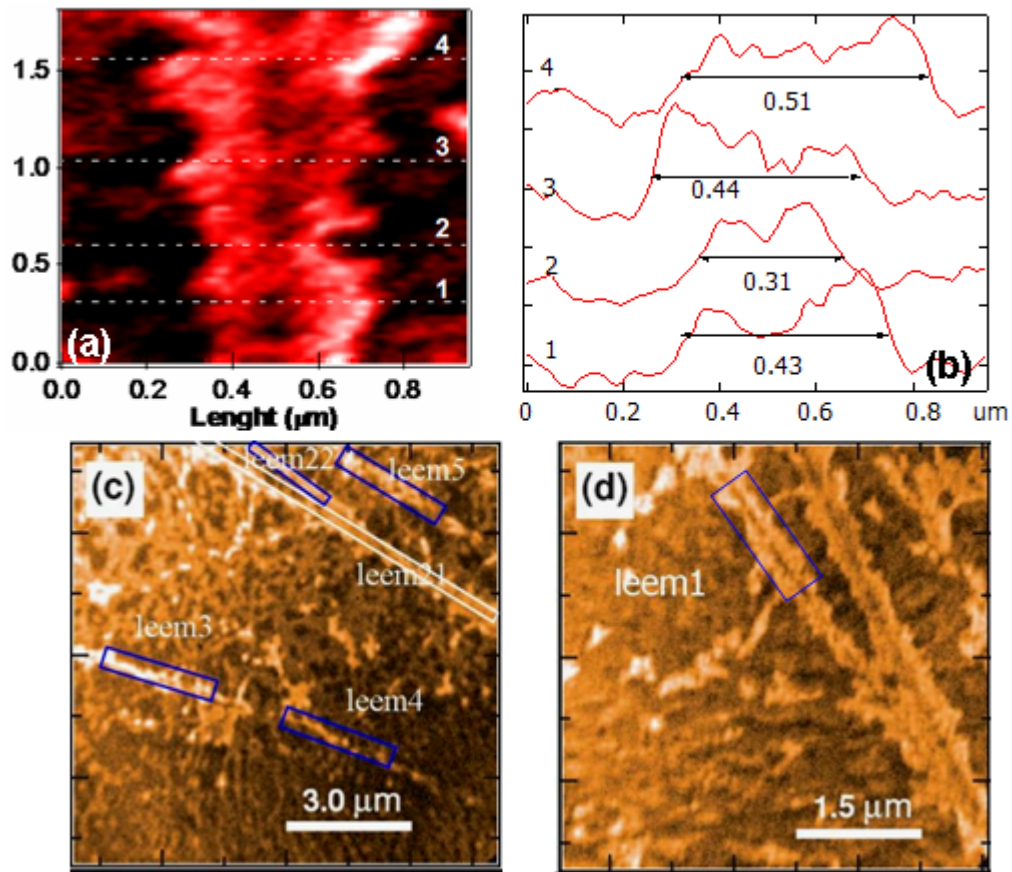
Figure 5.13 The LEEM image and corresponding graphene width analysis by Igor Pro software, (a) the 4 lines graphene width extract from blue square mark in (d) and the corresponding width in (b), (c) and (d) the LEEM images for graphene showing the lines of interest for analysis.
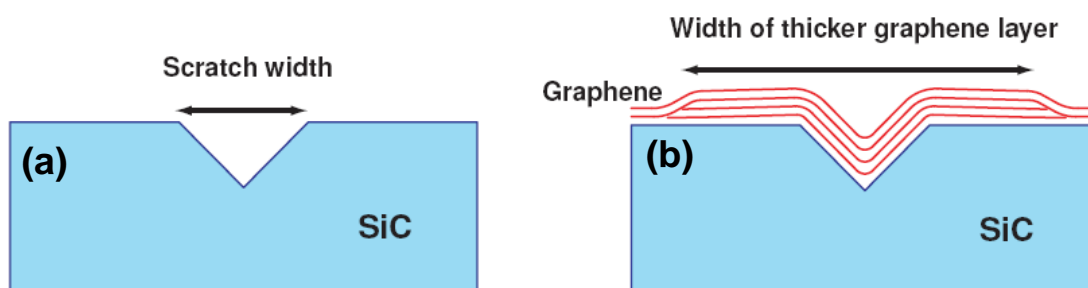
Figure 5.14 Schematics for a wedge shape of the surface scratch of the substrate in (a), and the graphene layers formed on substrate surface in (b).

5.5 Chemical analysis at PEEM experimental station

5.5.1 XPS measurements

This section describes an attempt to chemically analyze the epitaxial graphene prepared by thermal decomposition, as elaborated above. There are two possible chemical analytical techniques at the PEEM experimental station of BL3.2b, i.e. XAS and XPS. Synchrotron light from the U60 undulator was used for the excitation for both techniques. The ability to tune photon energy covering the absorption edge of carbon $1s$ allows carbon K-edge absorption spectra to be taken. The electron energy analyzer can be used for imaging/micro XPS measurements.
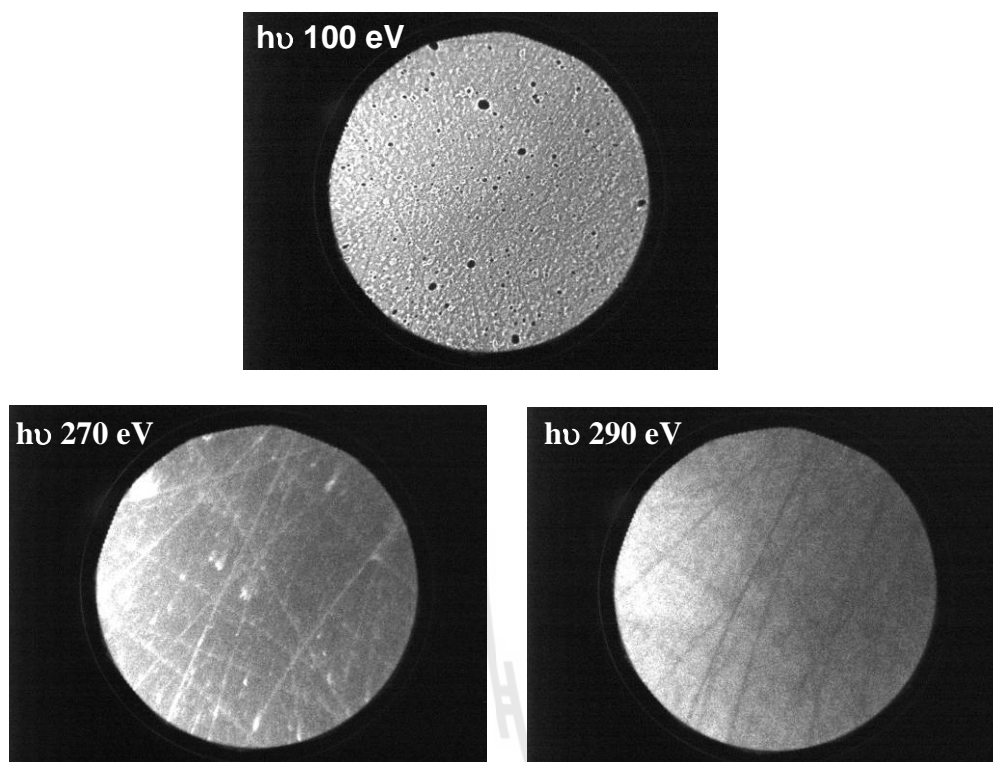
Figure 5.15 PEEM images illuminated with photon energy of 100, 270 and 290 eV.
(FOV = 75 μm)

Figure 5.15 shows PEEM images of the SiC sample after thermal decomposition at 1400 °C. The images were taken with three different excitation energies. The photon energy was chosen far below, near and above the absorption K-edge of carbon (i.e. at 100eV, 270eV and 290eV). The results are only for demonstrating the technical capability of the experimental station. It should be noted also that there is still problems associated with carbon contaminations in the beamline. The photon flux around the C K-edge is reduced due to the absorption by carbon atoms on the optical elements of the beamline. Even the gold mesh used for measuring the drain current might also suffer from carbon contamination on the mesh. This gives additional reduction of the measured photon flux.
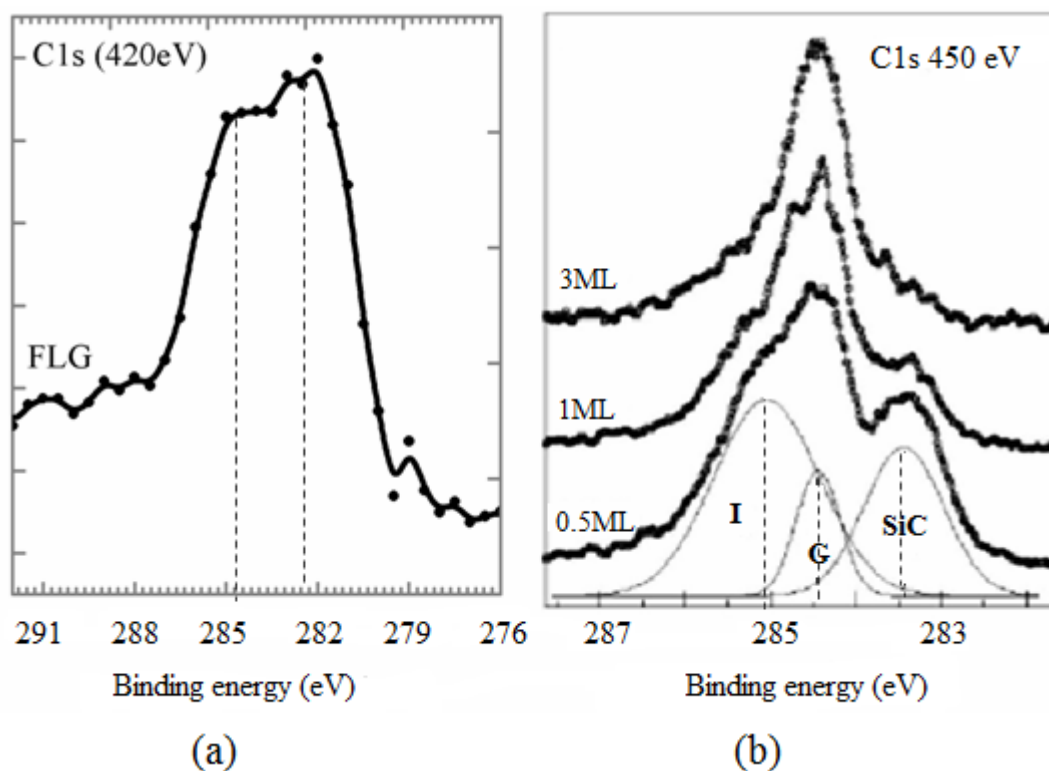
Figure 5.16 Micro-XPS spectra of epitaxial graphene prepared by thermal decomposition (a) this work and (b) reported by Virojanadara et al. (2008)

Imaging–XPS or micro-XPS can be carried out at the PEEM experimental station. However, one shall keep in mind that the energy resolution is not comparable to dedicated high resolution photoemission system. Figure 5.16 shows XPS spectrum taken from the SiC after flashing at 1400 °C (this work) and the high-energy resolution XPS spectrum of graphene reported by Virojanadara et al. (2008). The excitation energy for both experiments is given in the Figure; 420eV in this work and 450eV in Virojanadara's work. The carbon 1s peak in the XPS spectrum obtained in this work is rather broad, arising from overlapping of 2 or 3 peaks. There are 2 main peaks (A and B) located around 284.3 and 282.6 eV. It was reported by Virojanadara

that carbon 1s peak originated from bulk SiC, graphite/graphene, and the interface buffer layers can be found at binding energy of 283.4, 284.4, and 284.9 eV, respectively. The broadening of the carbon 1s peak obtained in this work may be caused by surface contamination and/or the variation of number of graphene layer. As observed from LEEM measurements, the number of graphene layer on the SiC sample was varied from 2 to 4 layers. The XPS spectrum was average spectrum of different number of graphene layer.

5.5.2 XAS measurements

A series of PEEM images were taken with a scan of photon energy around the absorption edge of C 1s. By doing so, absorption spectra on various areas of the sample are obtained. The elemental sensitivity of XANES is due to the characteristic binding energies of core electrons giving rise to X-ray absorption thresholds. The XANES spectra exhibit resonant electronic transitions from core levels into unfilled valence states, governed by well established selection rules. Figure 5.17 illustrated the sequence of X-ray micrographs taken at different photon energies across the carbon K-edge by aligning the image sequence in a photon energy stack and extracting the spectrum from a region of interest. The XANES spectrum in the absorption edge of the graphene prepared in this work is similar to those reported earlier. It was found that the optical elements of the BL3.2 are severely suffering from carbon contamination. This certainly affects measurement of absorption spectra of C 1s. The method to reduced carbon contamination on the optical elements shall be implemented in the future. Although there is the difficulty in obtaining absorption spectra of C 1s, it is possible to measure XANES spectra to distinguish between carbon atoms in SiC and in graphene, as shown in Figure 5.18.
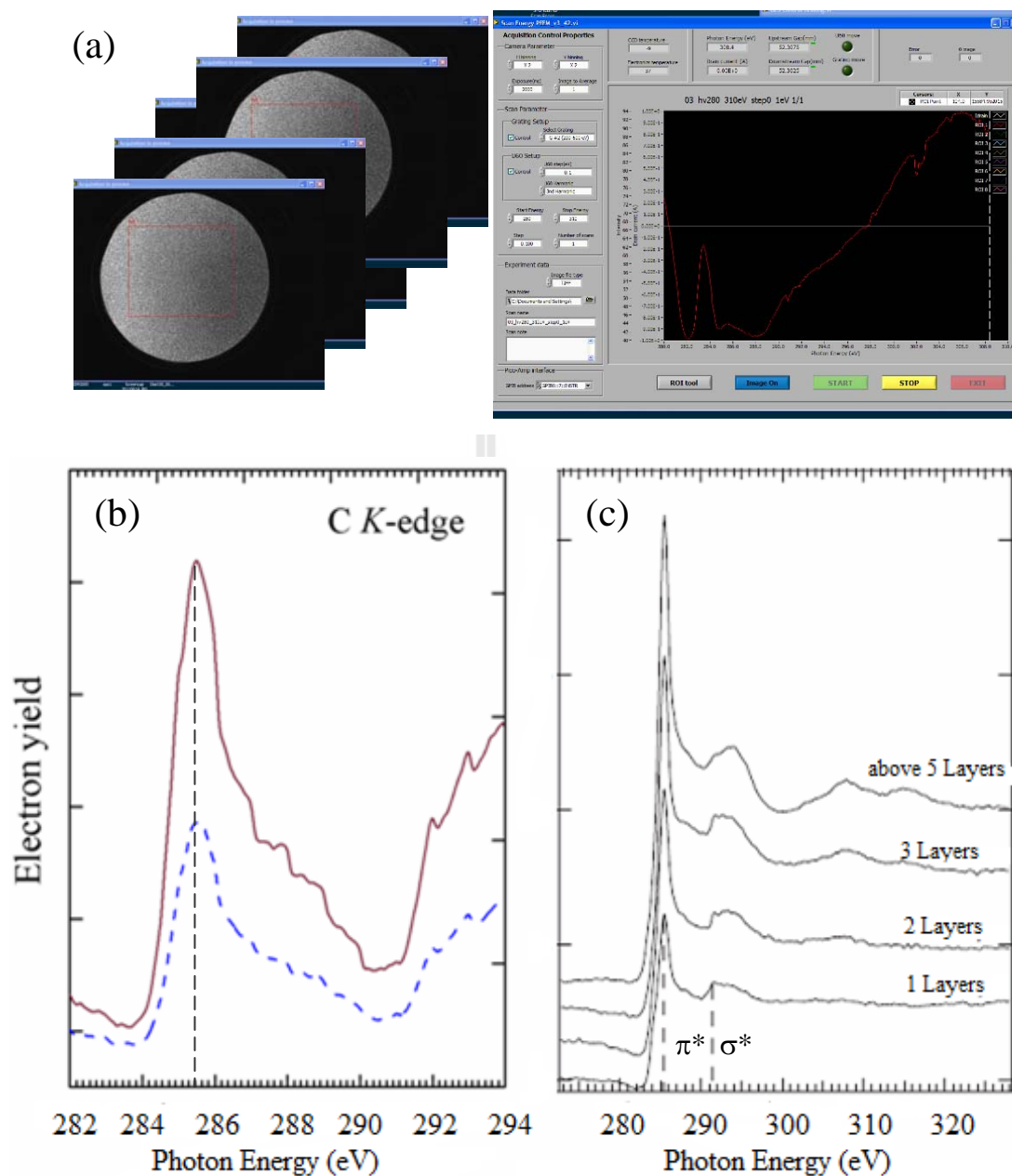
Figure 5.17 (a) The sequence of X-ray micrographs taken at different photon energies across the Carbon K-edge by aligning the image sequence in a photon energy stack and extracting the spectrum from a region of interest. (b) The corresponding Carbon K-edge of 2 area of interest in the PEEM image (c) NEXAFS of FLG grown by micromechanical cleavage of Highly Ordered Pyrolytic Graphite (HOPG) from Pacile et al. (2008).
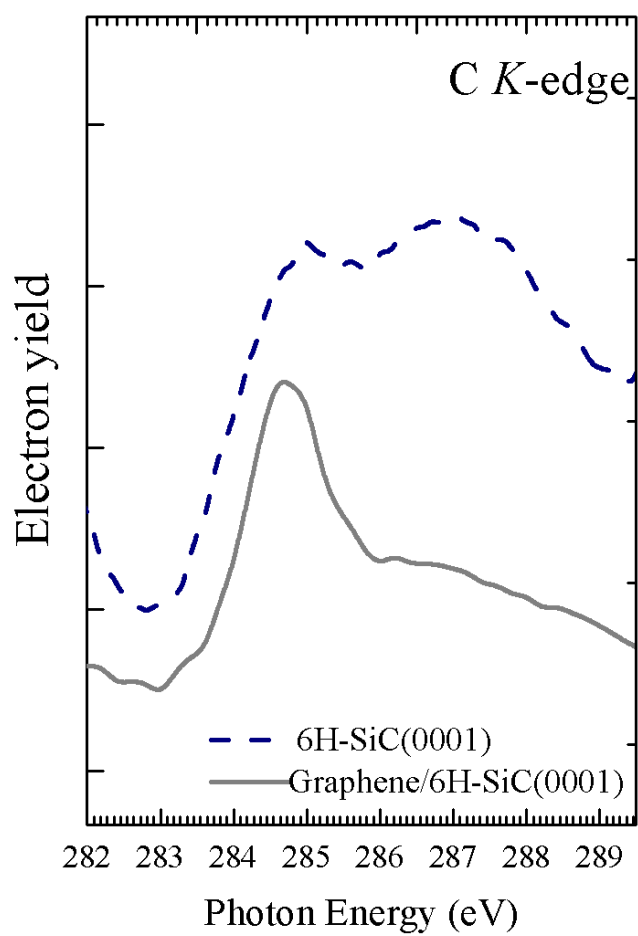
Figure 5.18 Absorption spectra of C K-edge taken from the 6H-SiC(0001) sample before (dash line) and after thermal decomposition to form graphene (solid line).

5.6 References

Bostwick, A., Emtsev, K. V., Horn, K., Huwald, E., Ley, L., McChesney, J. L., Ohta, T., Riley, J., Rotenberg, E., Speck, F. and Seyller. Th. (2008). Photoemission studies of graphene on SiC: Growth, Interface, and Electronic Structure. **Adv. in Solid State Phys.** 47: 159-170.

Choi, J., Lee, H. and Kim, S. (2010). Atomic-scale investigation of epitaxial graphene grown on 6H-SiC(0001) using scanning tunneling microscopy and spectroscopy. **J. Phys. Chem. C** 114: 13344-13348.

Chung, W. F., Feng, Y. J., Poon, H. C., Chan, C. T., Tong, S. Y. and Altman, M. S., (2003). Layer Spacings in coherently strained epitaxial metal films. **Phys. Rev. Lett.** 90: 216105 1-4.

Hibino, H., Kageshima, H., Maeda, F., Nagase, M., Kobayashi Y. and Yamaguchi, H. (2008). Microscopic thickness determination of thin graphite films formed on SiC from quantized oscillation in reflectivity of low-energy electrons. **Phys. Rev. B** 77: 075413 1-7.

Mathieu, C., Barrett, N., Rault, J., Mi, Y. Y., Zhang, B., de Heer, W. A., Berger, C., Conrad, E. H. and Renault, O. (2011). Microscopic correlation between chemical and electronic states in epitaxial graphene on $\text{SiC}\left(000\overline{1}\right)$. **Phys. Rev. B** 83: 235436 1-11.

Norimatsu, W. and Kusunoki, M. (2010). Formation process of graphene on SiC(0001). **Physica E** 42: 691-694.

Ohta, T., Gabaly, F. E., Bostwick, A., McChesney, J. L., Emtsev, K, V., Schmid, A. K., Seyller, Th., Horn, K. and Rotenberg, E. (2008). Morphology of graphene thin film growth on SiC(0001). **New J. of Phys**. 10: 023034 1-8.

Pacile, D., Papagno, M., Rodriguez, A. F., Grioni, M., Papagno, L., Girit, C. O., Meyer, J. C., Begtrup, G. E. and Zettl, A. (2008). Near edge x-ray absorption fine structure investigation of graphene. **Phys. Rev. Lett.** 101(6): 066806 1-4.

Tanaka, S., Morita, K. and Hibino, H. (2010). Anisotropic layer-by-layer growth of graphene on vicinal SiC(0001) surfaces. **Phys. Rev. B** 81: 041406 (R).

Virojanadara, C., Syvajarvi, M., Yakimova, R. and Johansson, L. I. (2008). Homogeneous large-area graphene layer growth on 6H-SiC(0001). **Phys. Rev. B** 78: 245403 1-6.

Virojanadara, C., Yakimova, R., Zakharo, A. A. and Johansson, L. I. (2010). Large homogeneous mono-/bi-labyer graphene on 6H-SiC(0001) and buffer layer elimination. **J. Phys. D: Appl. Phys.** 43: 374010 1-13.
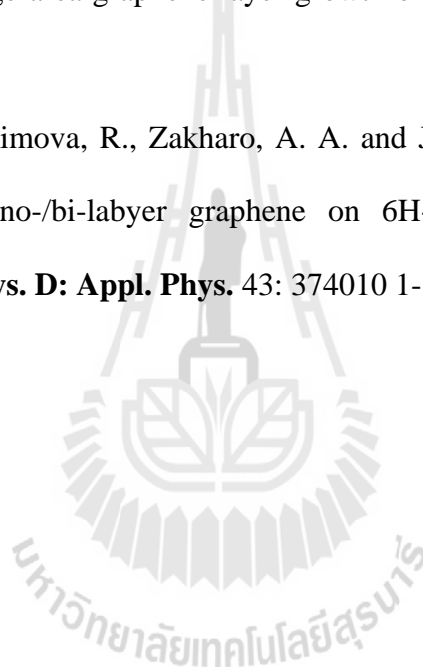
CHAPTER VI

CONCLUSION

The thesis is divided into two parts, i.e. the construction and commissioning of the PEEM experimental station of BL3.2b and the experiments on the formation of expitaxial graphene by thermal decomposition of SiC. The first part of the thesis involved the design, development and commissioning the PEEM experimental station of BL3.2b in which I participated in a development team of SLRI. The PEEM experimental station combines both spectroscopy and imaging that will be a very useful research facility for investigations of materials with nano/micro spatial resolution. The ability to tune photon energy of synchrotron light greatly enhances the capability of the experimental station.

From PEEM and LEEM observation, there was no observable effect of floor/mechanical vibrations on the image quality. The microscope can be positioned with respect to the synchrotron light beam, i.e. the whole FOV of the microscope can be illuminated with synchrotron light. The whole PEEM experimental station weights about 1,500 kg and requires an accuracy of a few microns in translation. More importantly, the microscope shall not be vibrating from the surroundings.

It has been demonstrated that PEEM images using synchrotron light could be obtained. Imaging XAS, a series of PEEM with series of photon energy, can be carried out at the experimental station. However, it was found that carbon

contamination on the optical elements of the beamline was significant. The method to

reduce the carbon contamination shall be developed and implemented at the beamline so that useful information can be extracted from carbon-containing materials.

Imaging XPS technique has also been demonstrated. The imaging XPS spectrum could be obtained by taking a series of PEEM images with different sample bias voltage, or electron energy. Additional data manipulation using image-processing software is required to generate XPS spectra at areas of interest. The practical spatial resolution is of hundred nanometers. An alternative XPS mode is micro-XPS in which an area of interest on the sample is selected by an area selection aperture, which is a physical aperture in the electron microscope column. The dimension of the area to be analyzed is defined by the dimension of the aperture. There are three area apertures with diameter of 1250, 400 and 100 microns.

The second part of the thesis is the investigation of epitaxial graphene synthesized by thermal decomposition of single crystalline SiC samples at high temperature. The experiments were ideal for this PEEM experimental station. Thermal decomposition of SiC was carried out in the microscope. The sample manipulator allows the sample to be heated up to 1700 °C. It was found that synthesizing epitaxial graphene from SiC requires temperature only upto 1400 °C. The experimental station provides various in situ techniques such as LEED, LEEM, PEEM including imaging/micro XPS and imaging XAS. The scientific part of this thesis work focused on observations of the spatial variation of number of graphene layer thermally decomposed from SiC. The numbers of graphene layers observed varied from 2 to 4 layers. Careful analysis of LEEM images found that there might be effects of scratches on the formation of graphene. It was pointed out that the number of graphene layers is usually greater near scratched areas of the SiC substrate. These

thicker areas of graphene occur not only within the scratch itself but also extend significantly outwards from the edges of a scratch.
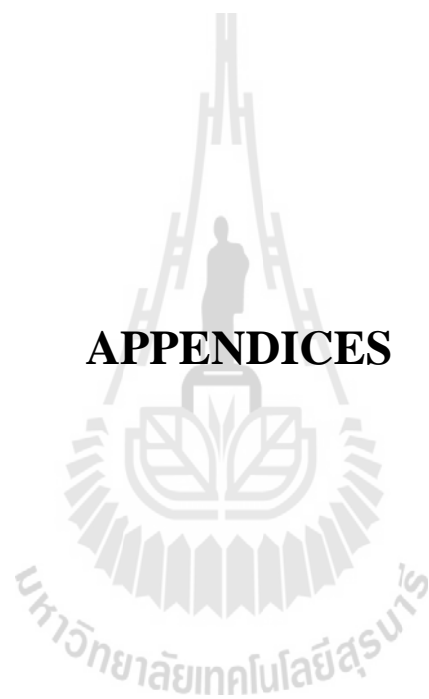
**APPENDICES**

APPENDIX A

HYDROGEN PLASMA ETCHING STSTEM

Along the course of this thesis work, a simple hydrogen plasma etching system was designed, constructed and tested. The system employed an existing vacuum chamber with additional new components fabricated at the SLRI machine shop. The system is planned to be for getting rid of scratches on the surface of single crystalline SiC samples. The plasma etching system is illustrated in Figure. A.1. The system is evacuated by a molecular pump backed by an oil-free scroll pump. The base pressure of this chamber is around 1×10^{-7} mbar. The sample can also be heated up to 1000 °C by a resistive 0.3-mm-thick tantalum foil boat. Water cooling is necessary to maintain the vacuum condition of the system. Hydrogen flow is controlled by a manual leak valve. A DC power supply is operated at 300 watt at maximum, which is sufficient for generating DC hydrogen plasma. The boat of the sample was heated by direct current with a current of 26.25 Amperes at 3.34 Volts. Detailed descriptions of the system are given in the caption of the Figures A.2-A.4. The engineering drawings of the components are also given in Figures A.5-A.12. Further improvement can simply be done by replacing the main chamber with bigger size to keep the distance between the wall of the chamber and the electrodes larger than the spacing between the electrodes.
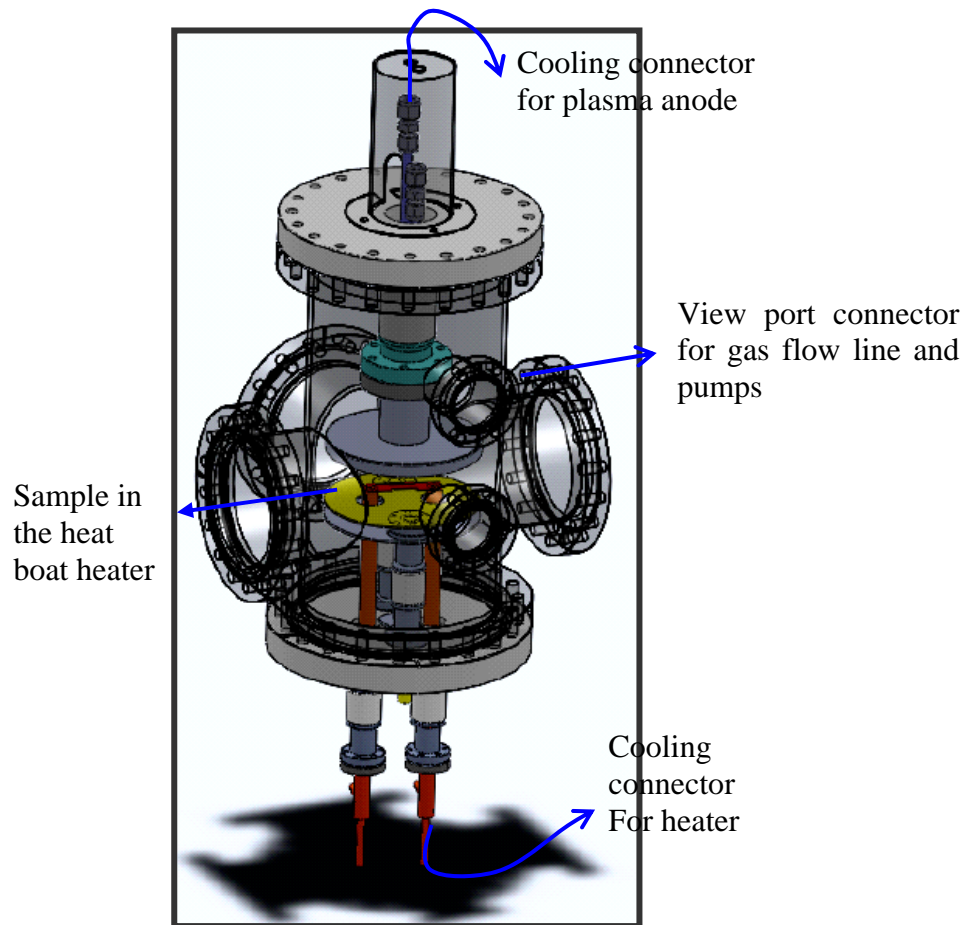
Figure A.1   Schematic of hydrogen plasma etching chamber.
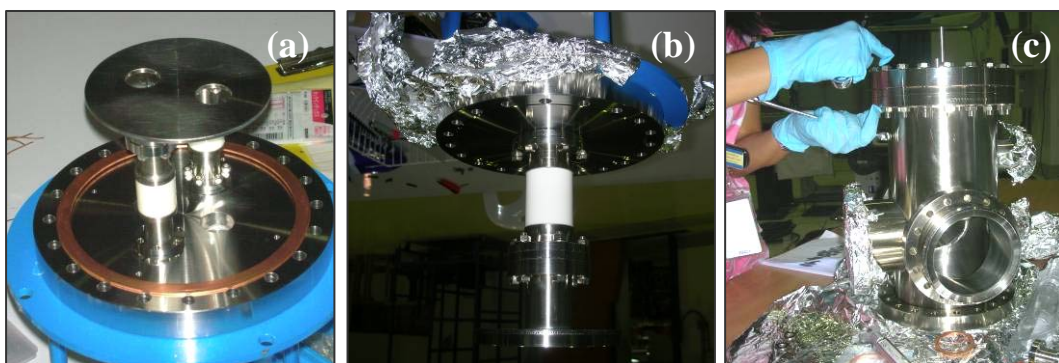
Figure A.2   The electrodes and the main chamber of the plasma etching system. (a) (a) the cathode with two holes for the boated heater, (b) the anode and (c) the chamber.
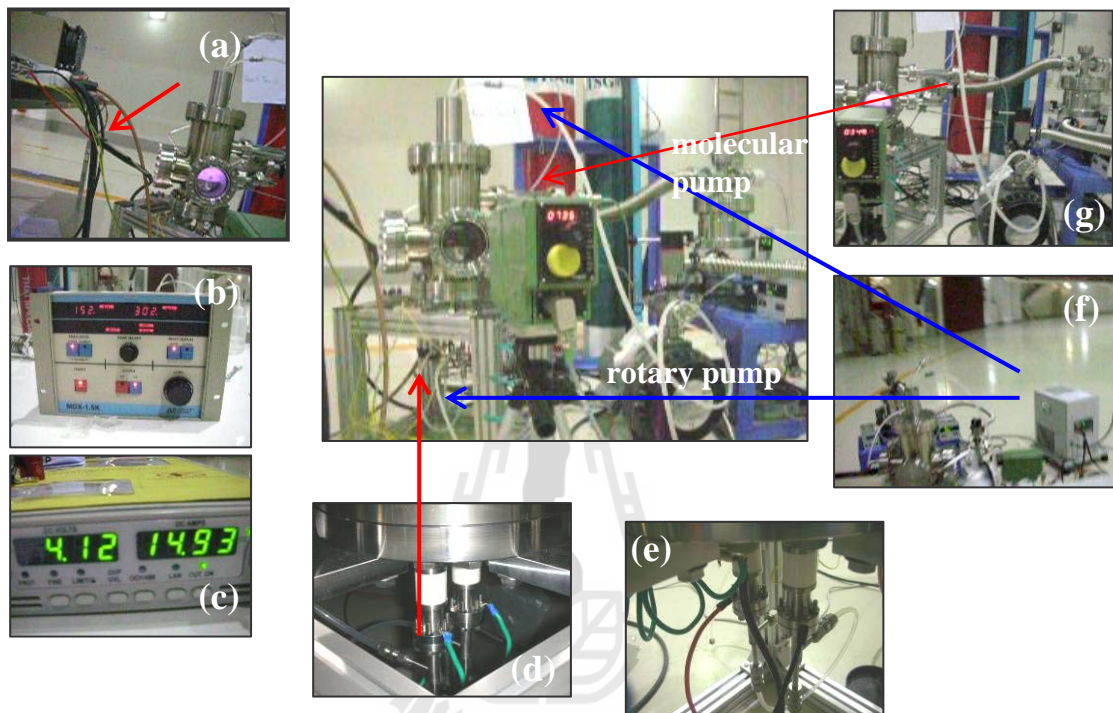
Figure A.3 Photos of the whole plasma etching system showing various part of the system: (a) the electrical cables connected to the plasma generator and power supply for the heater, (b) a DC plasma generator, (c) a power supply for the heater, (d)-(e) connector for the heater and plasma generator, (f) cooling tank connect to the (top) anode of the plasma chamber, (below) heater, (g) the four-way connector for the leak valve to control the inlet gas.

Figure A.4 Photos illustrate the procedures to remove the scratch on the SiC sample by plasma etching: (a) heating the sample up about 1000 °C, (b) flow pure hydrogen gas through the leak valve, while the DC power supply for the electrodes are on at 300W, until the plasma is formed as shown in (c). The operating pressure is $\sim 2\times 10^{-2}$ Torr.

Figure A.5 Exploded view drawing of the hydrogen plasma etching chamber.
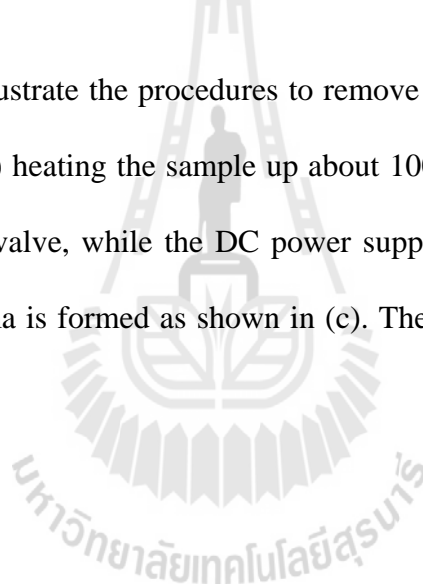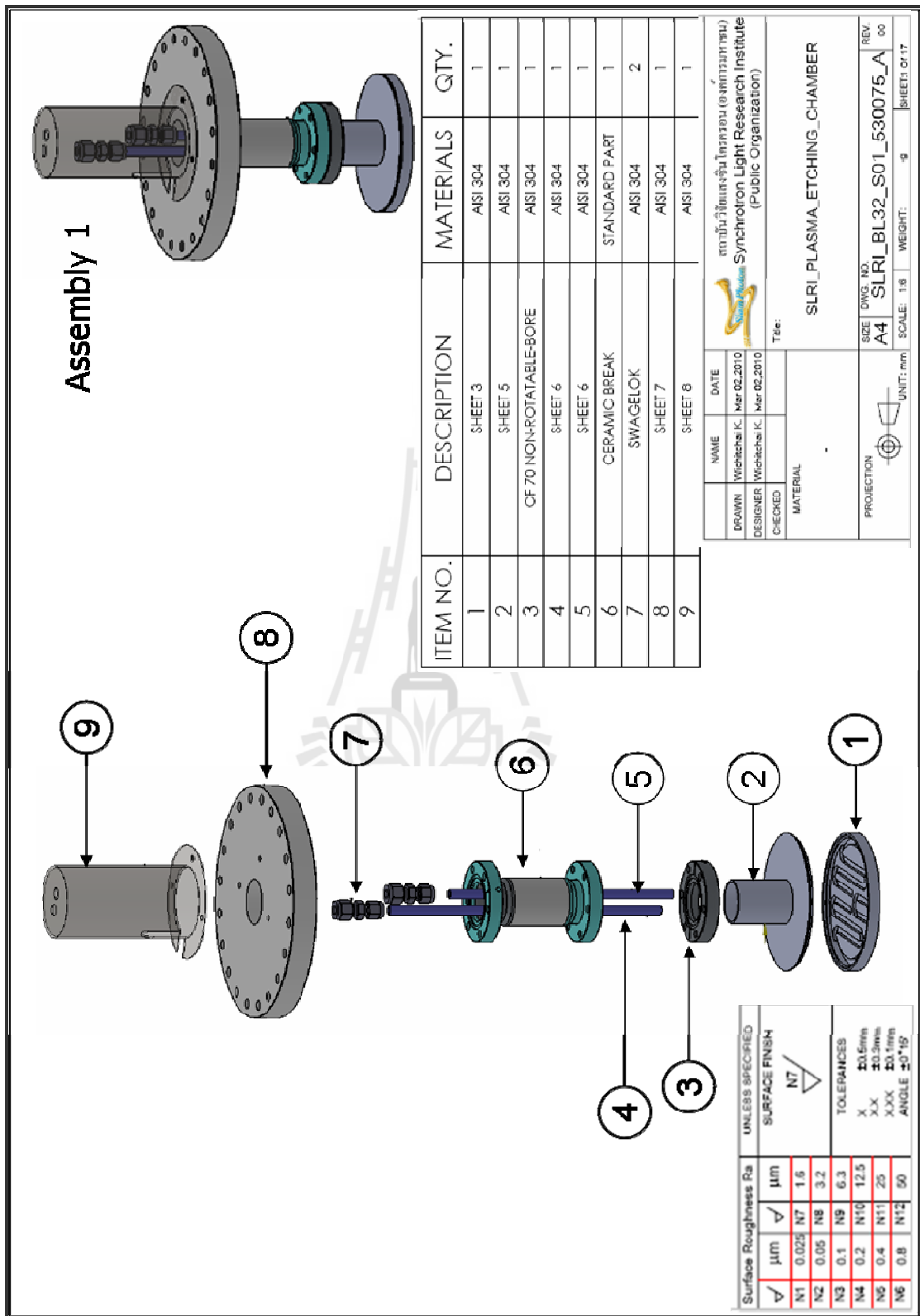
Figure A.6 Exploded view drawing of the Assembly 1: the cathode part of the plasma etching system.
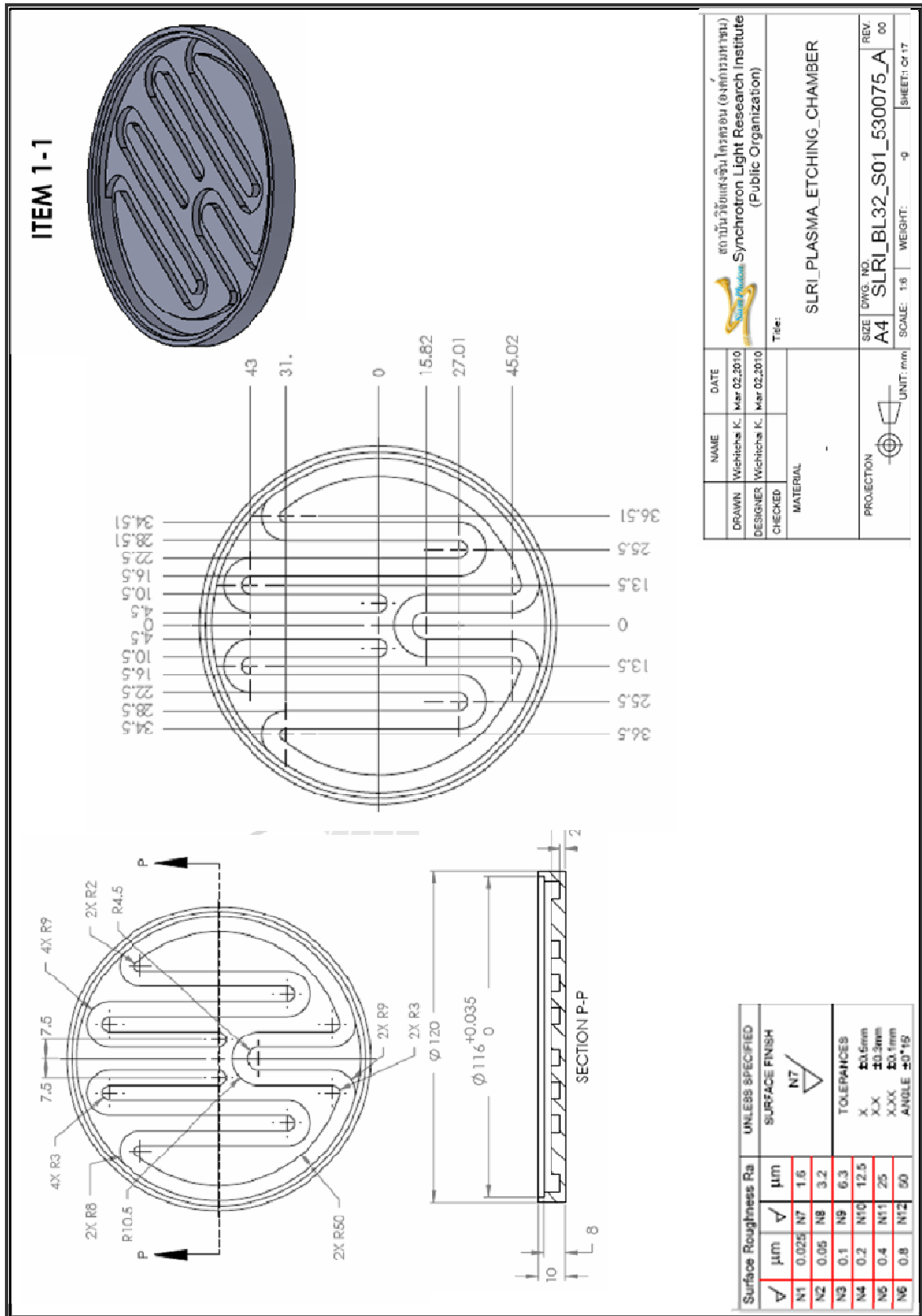
Figure A.7 Drawing of the water cooling tube for cathode (item 1 of assembly 1).
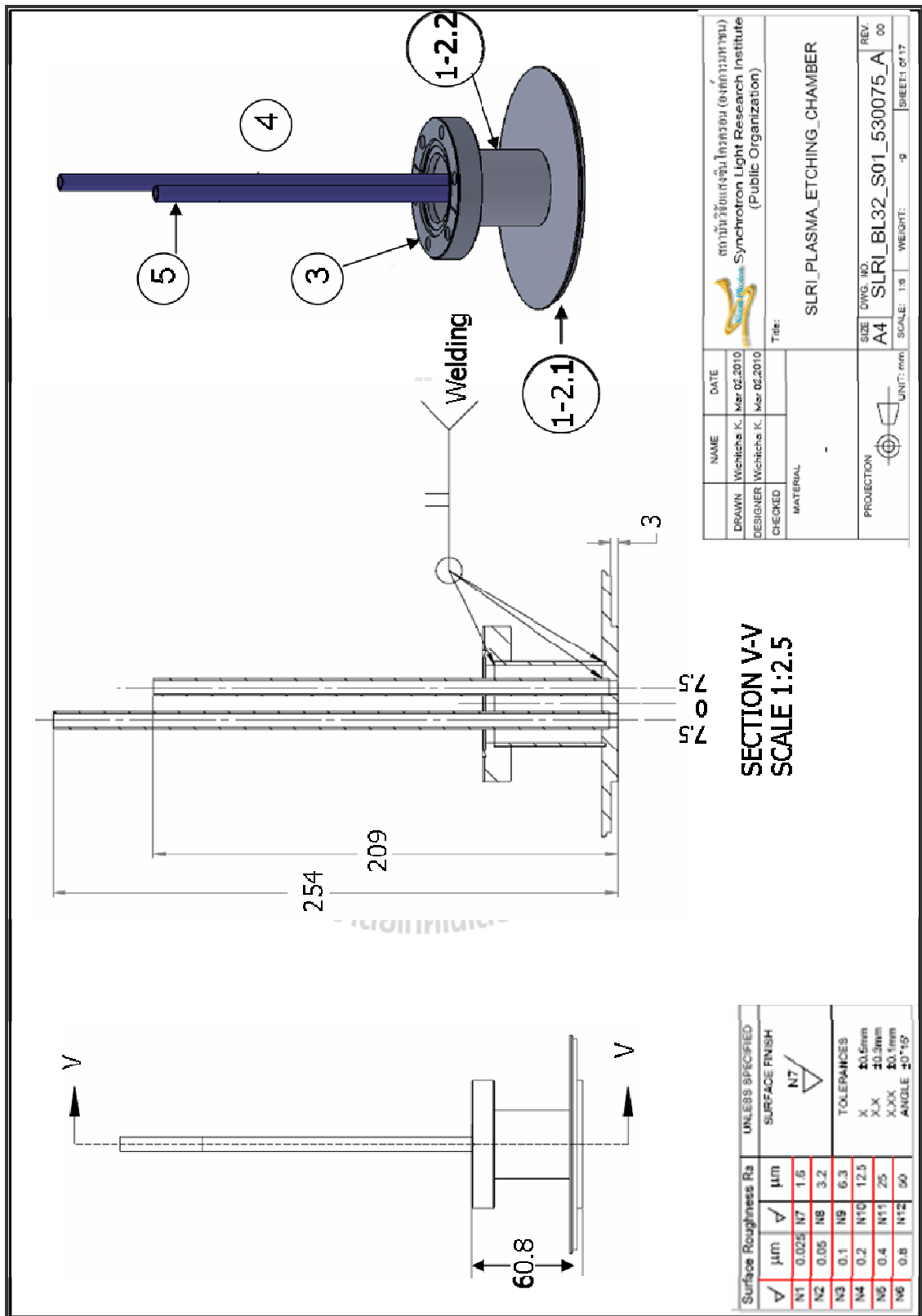
Figure A.8 Drawing of the cathode of the plasma etching system.
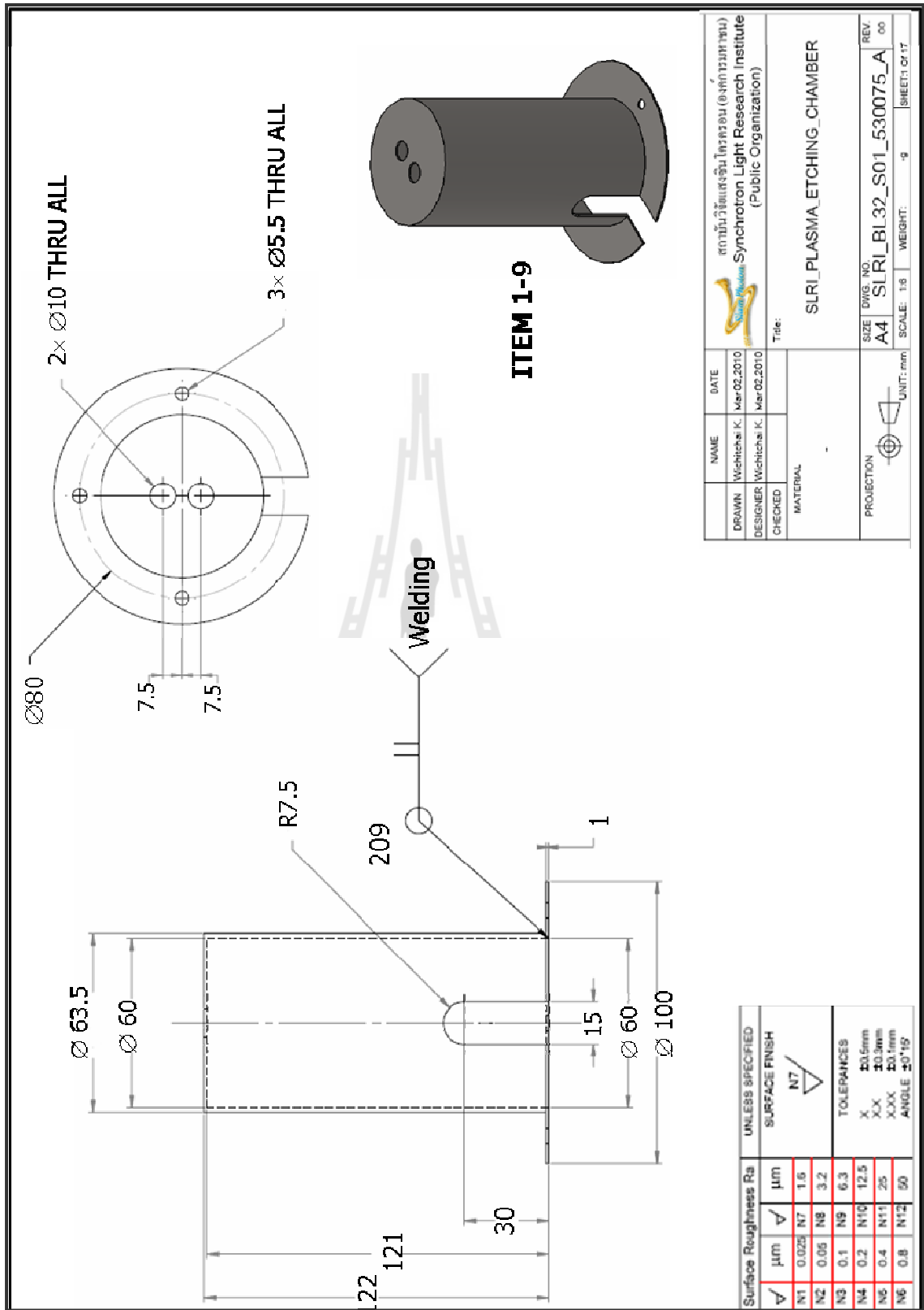
Figure A.9 Drawing of the cover cap for the cathode connector.

Figure A.10 Exploded view drawing of Assembly 3: the heater for heating sample around 1200 °C in vacuum system.
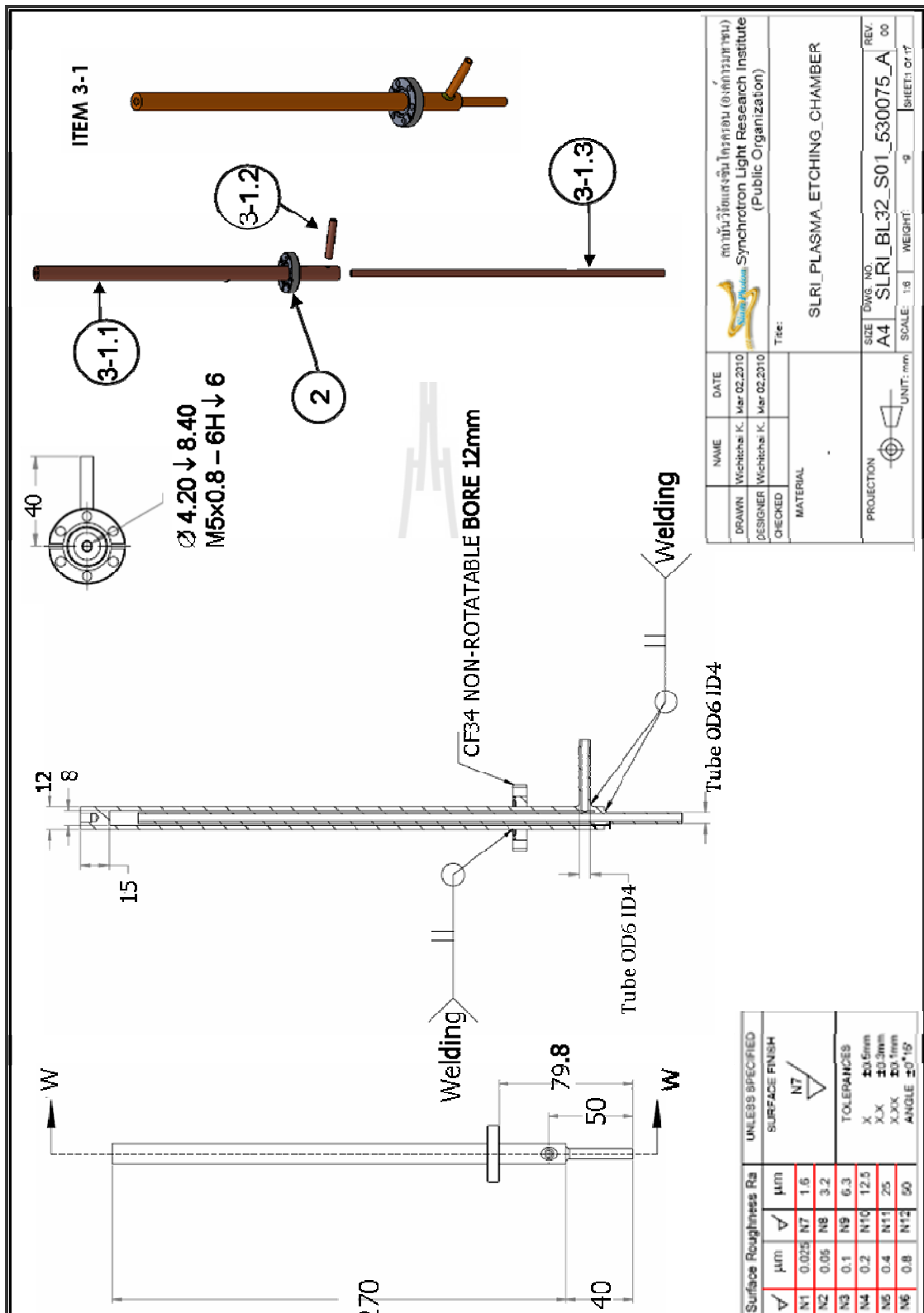
Figure A.11 Drawing of the water-cooled electrical feedthru of the boat heater (item 1 of Assembly 3).
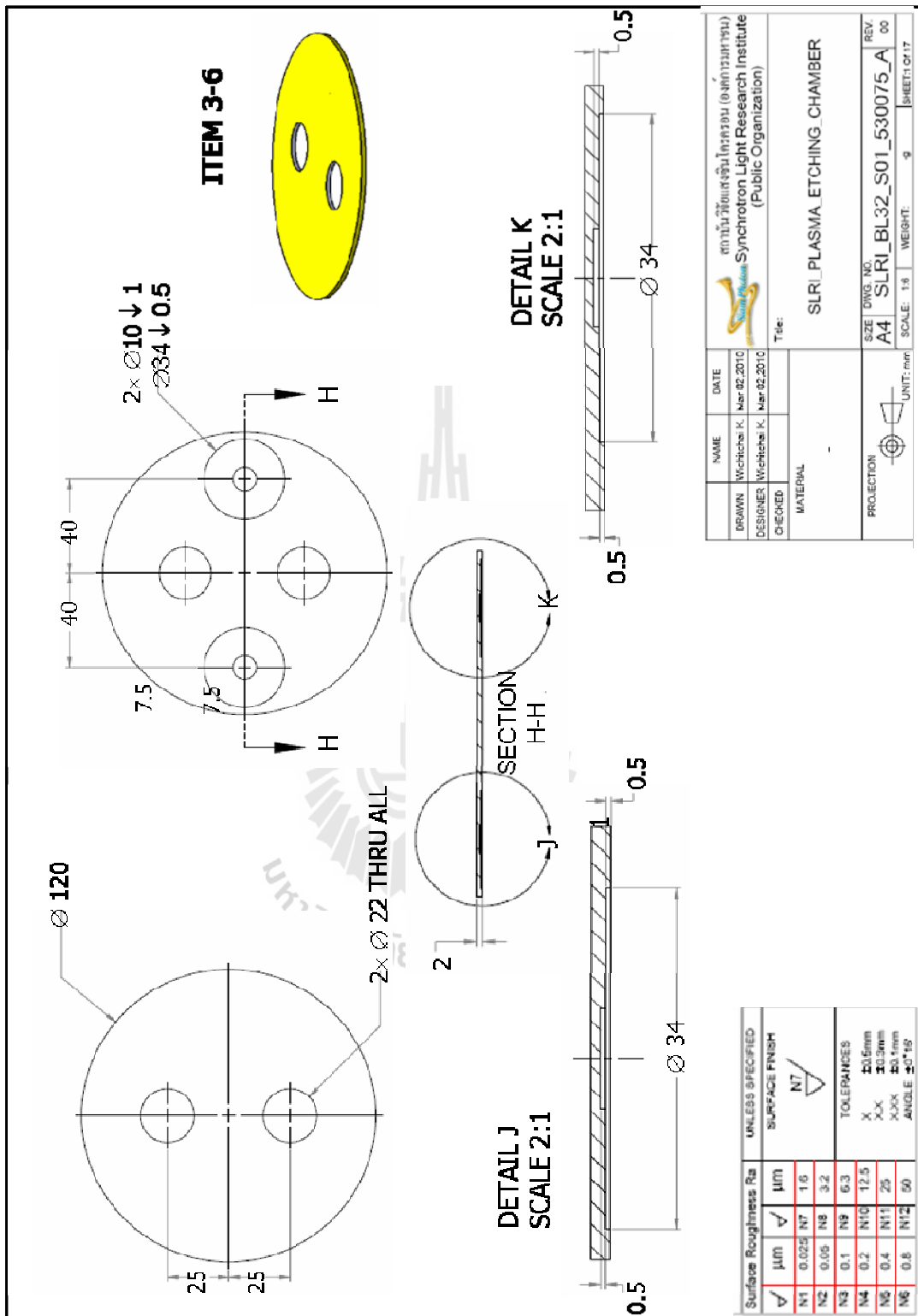
Figure A.12 Drawing of the electrode plates (item 6 of Assembly 3),

APPENDIX B

PUBLICATIONS AND PRESENTATIONS

B.1   List of Publication

Osaklung, J., Euaraksakul, C., Meevasana, W. and Songsiriritthigul, P. (2012). Spatial variation of the number of graphene layers formed on the scratched 6H-SiC (0001) surface. **Appl. Surf. Sci.** 258: 4672-4677.

B.2   List of Oral Presentation

Euaruksakul, C., Jearanaigul, N., Busayaporn, W., Osaklung, J. and Songsiritthigul, P. (March 2011). Photoemission Electron Microscopy Beamline of Synchrotron Light Research Institute. In **Siam Physics Congress 2011**. Chonburi: Thai Physics Society.

B.3   List of Poster Presentations

Osaklung, J., Nakajimal, H., Meevasana, W. and Songsiriritthigul, P. (2008). Elimination of Charging Effects in Total-electron-yield XAS Measurements. In **Siam Physics Congress 2008**. Nakhon Ratchasima: Thai Physics Society.

Rattanachai, Y., Osaklung, J., Puntheeranurak, T., Nakajima, H. and Songsiriritthigul, P. (2009). Low-energy Ion Bombardment of Nafion® Membrane. In **Siam Physics Congress 2009**. Phetchburi: Thai Physics Society

Osaklung, J., Euaruksakul, C. and Songsiriritthigul, P. (2010). LEEM investigations of epitaxial graphene formed by thermal decomposition of 6H-SiC(0001). In **Siam Physics Congress 2010**. Kanchanaburi: Thai Physics Society.

Osaklung, J., Euaruksakul, C., Meevasana, W. and Songsiriritthigul, P. (2011). Spatial variation of graphene layers formed on scratched 6H-SiC(0001) surface. In **Siam Physics Congress 2011**. Chonburi: Thai Physics Society.
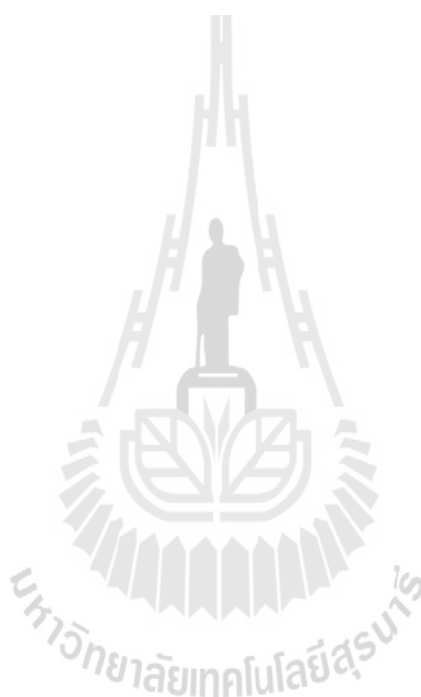
Manuscript accepted for publication in Applied Surface Science 258 (2012) 672-4677

Spatial variation of the number of graphene layers formed on the scratched 6H–SiC(0 0 0 1) surface

J. Osaklung[a,b], C. Euaruksakul[c,d], W. Meevasana[a,c,d,*], P. Songsiriritthigul[a,c,d]

[a] School of Physics, Suranaree University of Technology, Nakhon Ratchasima 30000, Thailand
[b] Department of Physics, Faculty of Science, Kasetsart University, Bangkok 10900, Thailand
[c] Synchrotron Light Research Institute, Nakhon Ratchasima 30000, Thailand
[d] Thailand Center of Excellence in Physics, CHE, Bangkok 10400, Thailand

ABSTRACT

The unique properties of graphene can vary greatly depending on the number of graphene layers; therefore, spatial control of graphene thickness is desired to fully exploit these properties in promising new devices. Using low energy electron microscopy (LEEM), we investigate how scratches on the surface of 6H-SiC(0 0 0 1) affect the epitaxial growth of graphene. Oscillations in the LEEM-image intensity as a function of electron energy (I–V LEEM analysis) show that the number of graphene layers clearly differs between regions of scratched and smooth substrate. The extent of the thicker graphene layers formed above scratches is found to be significantly larger than the width of the scratch itself. This finding can be implemented as an additional technique for spatially modulating graphene thickness.

© 2012 Elsevier B.V. All rights reserved.

1. Introduction

After Geim and Novoselov discovered graphene, a single atomic layer of graphite, in 2004 by exfoliating highly oriented pyrolytic graphite[1], many unique electronic properties of graphene have been reported, including extremely-high mobility [2], ambipolar behavior [2], the room-temperature quantum hall effect [3], and plasmarons [4]. These unique properties and the abundance of carbon materials promise carbon-based electronic devices with superior performance and novel functionalities over current semiconductor devices.

As the properties of graphene are largely dependent on the number of layers, (e.g. bandgap opening [5,6] and plasmaron coupling [4]), many recent studies have focused on methods for growing a precise number of graphene layers. There are various methods for creating graphene such as the drawing technique (mechanical exfoliation of graphite crystals) [7], epitaxial growth on semiconductor [2] and metal [8,9] substrates, and chemical vapor deposition (CVD) [10,11]. Epitaxial graphene prepared on silicon-carbide (SiC) is a method which produces a particularly high quality graphene. By using this method, many interesting results such as the relativistic electronic structure (so-called "Dirac cone")

[12], bandgap opening [13], and anomalous quantum Hall effect [14,15] have been reported. However, to exploit these properties for industrial purposes, graphene growth over a decently large area and the ability to pattern the graphene with different numbers of layers is still under development. So far, the in-plane size of uniform graphene by using this method is limited to around $3\,\mu m \times 50\,\mu m$ as reported by Emtsev et al. [16], and $50\,\mu m^2$ as reported by Virojanadara et al. [17]. One of the factors limiting growth beyond this size could be the roughness of or scratches on SiC surfaces [18]. Note that the graphene grown using the CVD technique [10] can actually be much larger in the order of centimeters; however, the quality of this graphene can be inferior to epitaxial graphene as the reported carrier mobility of CVD-grown graphene appears to be much lower than that of epitaxial graphene (e.g. approximately 7 times lower comparing Ref. [10] and Ref. [19]).

To better understand the formation and shape of epitaxially grown graphene, in this paper, we look into the effect that substrate scratches (~0.2 μm in width) have on the spatial variation of graphene layers formed on a 6H–SiC(0 0 0 1) surface. By using low-energy electron microscopy (LEEM), we extract the number of graphene layers over selected surface areas using a I–V (Intensity–Voltage) analysis of the LEEM images [20]. The number of layers is observed to be higher near the scratched areas and importantly the thicker graphene layers can have a width as large as 2.5 times of the scratch width itself (see Fig. 4).

* Corresponding author at: School of Physics, Suranaree University of Technology, Nakhon Ratchasima 30000, Thailand. Tel.: +66 44 224 291; fax: +66 44 224 651.
E-mail address: worawat@g.sut.ac.th (W. Meevasana).

Manuscript accepted for publication in Applied Surface Science 258 (2012) 672-4677
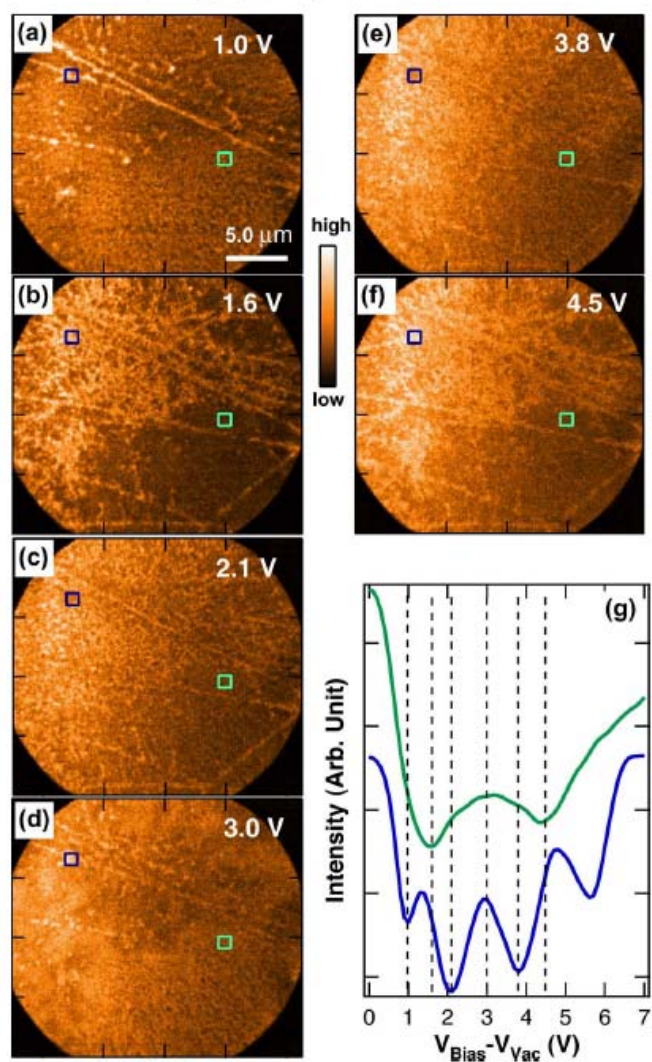
Fig. 1. LEEM images of the graphene grown on the scratched SiC substrate at various adjusted bias voltages ($V_{Bias} - V_{Vac}$) of the incident electron: (a) 1.0, (b) 1.6, (c) 2.1, (d) 3.0, (e) 3.8 and (f) 4.5 V. (g) shows the plots of intensity at the two selected spots (blue and green squares in (a)–(f)) as a function of bias voltage (I–V LEEM plot); note that the two plots are offset by the two intensities at $V_{Bias} - V_{Vac} = 0$ V. (For interpretation of the references to color in this figure legend, the reader is referred to the web version of the article.)

2. Materials and methods

In this study, the epitaxial graphene layers were grown on a 6H–SiC(0 0 0 1) substrate by thermal decomposition in an ultra-high vacuum environment. The n-type doped 6H–SiC(0 0 0 1)(MTI Corporation) is one side polished. The dimension of the substrate is 5 mm × 5 mm × 0.3 mm with the axis of orientation (0 0 0 1). The surface topography of the substrate was examined by atomic force microscopy (AFM) in AC mode. An AFM image was taken after chemical cleaning (shown in Fig. 3a). Another one was then taken after a short annealing process (not shown) but it does not show a significant difference. Both were taken before the

Manuscript accepted for publication in Applied Surface Science 258 (2012) 672-4677

Fig. 2. IV-LEEM analysis of the graphene grown on the scratched SiC substrate at various positions labeled by numbers. (a) and (c) show the various analyzed positions on the scratch and away from the scratch respectively. (b) and (d) show corresponding IV plots of each labeled positions in (a) and (c) respectively. The IV oscillations indicate that there are mostly, 3–4 graphene layers on scratched locations and 2 graphene layers otherwise. The dashed lines in (d) are at the bias voltages where the image contrast between 2 graphene layers and higher number of layers is high.

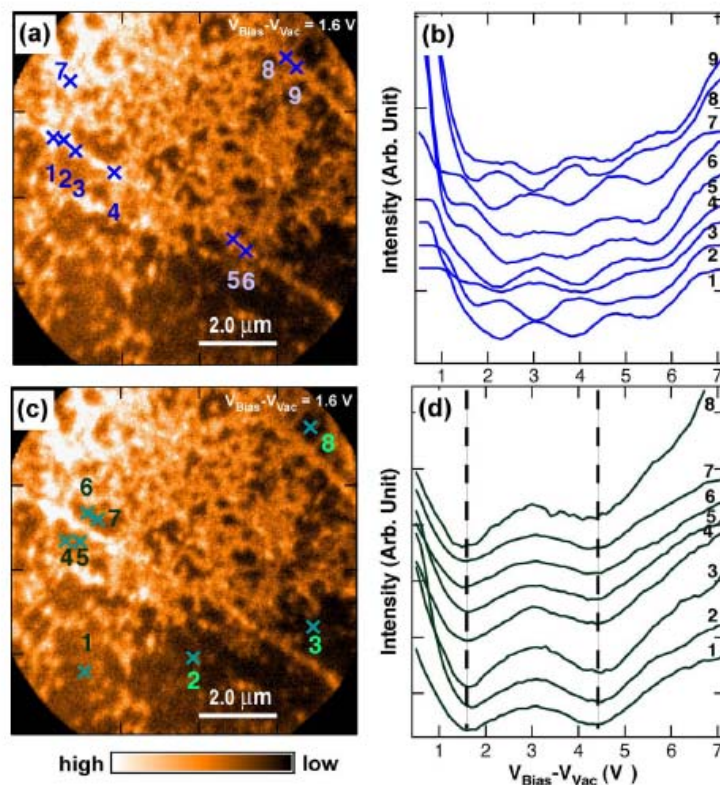graphitization process which will be described in the next paragraph. From the AFM measurement, scratches which occur during the polishing process (i.e. due to polishing substance) have widths and depths distributed mainly around two sets of values: (1) 120 nm wide and 1–2 nm deep, and (2) 230 nm wide and 5 nm deep. The scratch lengths are usually longer than 50 μm. Low energy electron microscopy (LEEM) and low energy electron diffraction (LEED) measurements were then performed in situ with a Elmitec LEEM III equipped hemisphere electron energy analyzer at Beamline 3.2b, Synchrotron Light Research Institute (SLRI), Thailand. The base pressure during measurement was 3×10^{-10} torr.

Before putting the SiC substrate in the vacuum chamber, the substrate was cleaned by (i) the mixture of NH_4OH, H_2O_2, and de-ionized water with a ratio of 1:1:5 as well as heated at 70 °C for 10 min, (ii) etched by 5% HF acid and (iii) the mixture of HCL, H_2O_2, and de-ionized water with a ratio of 1:1:5 as well as heated at 70 °C for 10 min. The substrate was then flashed to around 1200 °C by electron-beam bombardment 3 times in order to remove oxides from the surface. After the oxides were removed, we observed $6\sqrt{3} \times 6\sqrt{3}$ reconstruction of SiC in the LEED pattern; this

indicates that the first carbon layer, the so called buffer layer [21], was formed. To reduce some scratches on the sample surface, the sample was heated to around 1300 °C while flowing purified hydrogen gas into the UHV chamber for 40 min with base pressure 1×10^{-7} torr and then the sample was flashed to 1400 °C. During these etching and flashing processes, the thermal decomposition of the substrate surface occurred and graphene was formed on the surface. LEEM images of graphene formed on the SiC substrate were measured at the field of view (FOV) of 25 μm, as shown in Fig. 1.

While some information regarding the surface topography can be obtained from the LEEM image, the LEEM technique can also determine the distribution of local graphene thickness by measuring a series of LEEM images at different incident-electron bias voltages (i.e. varying electron energy) [18,20,22–24]. Information on the number of graphene layers is contained in the oscillating intensity of reflecting electrons as a function of the voltage, i.e. I–V LEEM analysis [20,23]. In the I–V LEEM analysis, given a graphene thickness, electrons with only certain discrete energy levels are allowed inside the quantum well potential [20,25]. Due to these discrete energy levels, incident electrons with various energies

Manuscript accepted for publication in Applied Surface Science 258 (2012) 672-4677
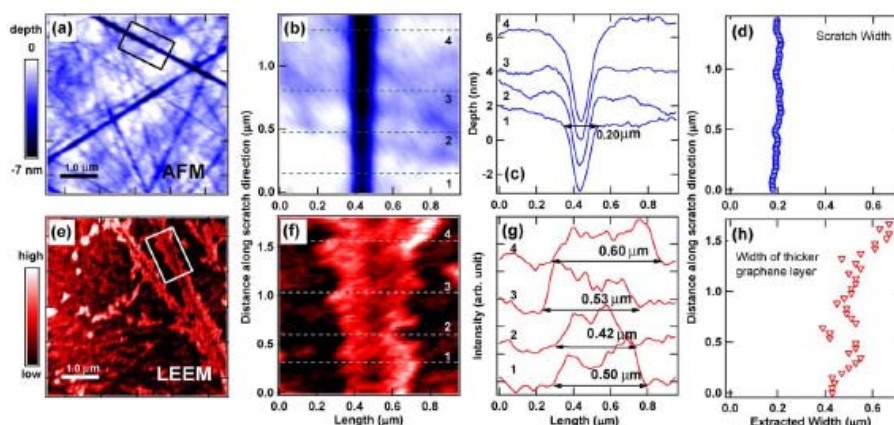
Fig. 3. Comparison of the scratch width and the width of the thicker graphene layer. (a) shows AFM image of SiC substrate before the graphitization process with 5 μm FOV where the color represents relative depth of the surface. (b) shows the magnified area of the black rectangle in (a). (c) shows the depth profiles corresponding to the dashed lines in (b) and (d) shows the full width along the scratch direction in (b). (e) shows the LEEM image of graphene on the SiC substrate after the graphitization process where the color represents LEEM intensity. The same procedures as (b)–(d) are applied to the LEEM image as shown in (f)–(h) to get the width of the thicker graphene layer, except that the width is obtained from the distance between the bottoms of the two leading edges.

will get reflected differently, creating an oscillating I–V spectrum which corresponds to the particular thickness. When the thickness of graphene layers changes, the oscillating I–V curve will change accordingly. We performed this I–V LEEM analysis on a set of LEEM images to determine the number of graphene layers at different locations in the sample as shown in Figs. 1 and 2.

3. Results and discussions

Fig. 1 shows the LEEM images taken after etching and flashing processes, with FOV of 25 μm. In Fig. 1(b), the scratch marks are mostly visible along high-intensity lines and the flat regions are mostly in low-intensity areas. However, these high and low intensities do not solely originate from the contrast of the surface topography since the LEEM technique also picks up the contrast from the electronic structure at the surface. As shown in Fig. 1(a)–(f), LEEM images are taken at the same spatial region while the adjusted bias voltage, $V_{Bias} - V_{Vac}$, is varied between 0–9 V where the voltages are 1.0, 1.6, 2.1, 3.0, 3.8 and 4.5 V respectively; note that V_{Vac} is defined as the vacuum energy level divided by electron charge, e [26]. As the electron energy is varied, the contrast of the LEEM image changes dramatically; at some energy (e.g. Fig. 1(c)), some of the scratch marks coming from the surface topography are barely visible. As briefly explained in Section 2, this change of the image intensity as a function of bias voltage is set by the electronic structure (i.e. quantum well states [20,25]) of graphene layers on SiC substrate. As shown in Fig. 1(g), the image intensities from the two selected spots (see blue and green squares in panel (a)–(f)) oscillate differently when the bias voltages vary in the same range as in Ref. [20]. The number of dips in this oscillation will equal the number of graphene layers at that spot [20,22,23]. The blue (green) curve has 4 (2) dips, indicating that there are 4 (2) layers of graphene on the selected blue (green) spot.

We have then applied this I–V LEEM method to various locations on LEEM images as shown in Fig. 2. In Fig. 2(a), spots labeled numbers 1–9 are selected from scratched areas and the corresponding I–V curves are then extracted and shown in panel (b). The numbers of dips are mostly 3–4, indicating that the numbers of graphene

layers are mostly 3–4 in the scratched areas. On the other hand, in Fig. 2(d), the I–V curves selected from the smooth, low-intensity areas (spot numbers 1–8 in Fig. 2(c)) have mostly only two dips, indicating that the smooth areas are mostly covered with two layers of graphene. This data clearly suggests that scratches on the SiC surface can promote the enhanced growth of graphene. This behavior is similar to other studies [27–29] which show that the graphitization process usually starts near the steps of a surface rather than flat terraces. Ref. [29] describes "steps" on substrates as the kicker of graphene nucleation by providing C atoms. In our case, it is slightly different as a scratch has a wedge shape rather than a step shape; we observed that the enhanced growth of graphene happened not only right above the scratch areas but also extended significantly further from both edges of a scratch (see schematic picture in Fig. 4). Note that although we could not tell whether the additional layers are on top or underneath from our I–V LEEM analysis, we speculate that the additional layers are underneath based on the model in Ref. [27].

We then investigated further to what extent the enhanced graphene growth occurs away from the edges of a scratch. To measure the width of the scratches on the SiC substrate, we first performed AFM measurements before the graphitization process. The AFM image in Fig. 3(a) shows the relative depth at each spatial position; we then selected a portion of the scratch with a large width as shown in Fig. 3(b) which is the magnified area of the black rectangle in panel (a). The depth profiles along the perpendicular direction (e.g. dashed lines) are plotted in Fig. 3(c). The width along the scratch direction is then measured from the full width of these profiles, plotted in Fig. 3(d). We find that the average scratch width from this section is around 0.20 ± 0.01 μm. After the graphitization process, we performed the same procedure to the LEEM image of graphene on the SiC substrate (predominately within the white rectangle in panel (e)), as shown in Fig. 3(e)–(h). We note that for the LEEM image used for this analysis, we adjusted bias voltage so as to maximize the image contrast between the graphene domains in the vicinity of the scratches and the rest of the area (see the left vertical dashed line in Fig. 2(d), around $V_{Bias} - V_{Vac} = 1.6$ V). As shown in Fig. 3(h), the widths of graphene with more than

Manuscript accepted for publication in Applied Surface Science 258 (2012) 672-4677
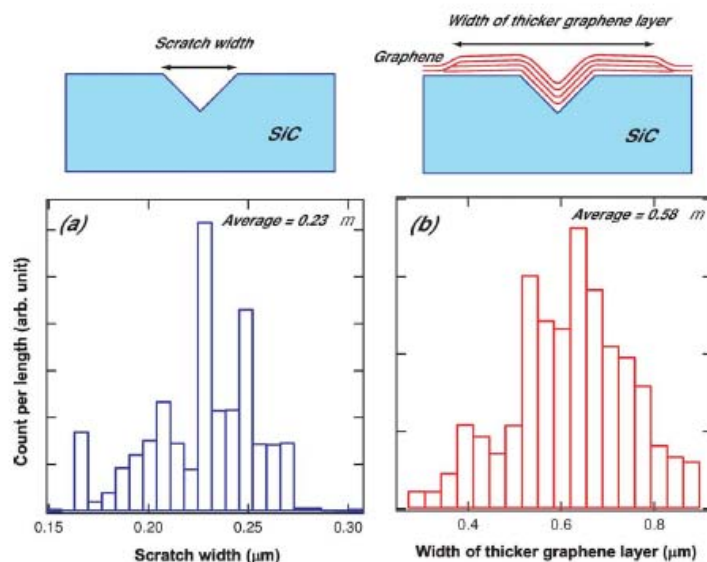
Fig. 4. (a) and (b) show the histograms of scratch widths extracted from various parts of AFM images and width of thicker graphene layer extracted from various parts of LEEM images, respectively. Above of the graphs are the schematic pictures of the widths measured from the scratch and the thicker graphene layers respectively.

2 layers, along the scratch direction, are extracted from the distance between bottoms of the two leading edges (see arrows in panel (g)). The average value of this width is around $0.52 \pm 0.07\,\mu m$ which is approximately 2.6 times larger than the average scratch width from Fig. 3(d).

Focused on other regions with large widths, we extracted more data from both AFM and LEEM images to get a better average. The histograms of these extracted widths are shown in Fig. 4. Note that these widths are measured along scratch direction with combined lengths of $20\,\mu m$ and $30\,\mu m$ from AFM and LEEM images, respectively (approximately 15 and 20 times longer length used in Fig. 3). The average scratch width is $0.23\,\mu m$ and the average width of thicker graphene layer is around $0.58\,\mu m$ which is approximately 2.5 times larger, similar to the ratio obtained in Fig. 3.

By comparing these extracted widths it is clear that the enhanced growth of graphene can extend much further from the edge of a scratch: see the schematic pictures in Fig. 4. This graphene formation near the wedge-shape groove appears to be different from the studies of graphene formed on [27,29,30] as these studies report that the thicker graphene layers usually occur within the two edges of the steps. Hence, the results of our investigation suggest that different shapes of surface discontinuities alter the formation of enhanced graphene growth in different ways. Although the microscopic origin is still subject to further investigation, this data already suggests a new method of using wedge-shape grooves to spatially vary the thickness of graphene formed on a SiC substrate.

4. Conclusion

By performing I–V LEEM analysis on graphene grown on SiC substrates, we find that the number of graphene layers is usually greater near scratched areas of SiC substrate. These thicker areas of graphene occur not only within the scratch itself but also extend significantly outwards from the edges of a scratch. From this case study, the width of the thicker graphene layers can be up to 2.5 times larger than the scratch width itself. While it would be interesting to investigate further on how to control this width, the current study already suggests an alternative way of using a scratch (i.e. wedge shape grooves) pattern for spatially varying graphene layers grown on a 6H–SiC(0 0 0 1) substrate.

References

[1] K.S. Novoselov, et al., Science 306 (2004) 666.
[2] A.K. Geim, K.S. Novoselov, Nat. Mater. 6 (2007) 183.
[3] K.S. Novoselov, et al., Science 315 (2004) 1379.
[4] A. Bostwick, et al., Science 328 (2010) 999.
[5] E.V. Castro, et al., Phys. Rev. Lett. 99 (2007) 216802.
[6] T. Ohta, et al., Phys. Rev. Lett. 98 (20) (2007) 206802.
[7] K.S. Novoselov, et al., PNAS 102 (2005) 10451.
[8] P.W. Sutter, et al., Nat. Mater. 7 (2008) 406.
[9] A. Siokou, et al., Appl. Surf. Sci. 257 (2011) 9785.
[10] K.S. Kim, et al., Nature 457 (2009) 706.
[11] J.L. Qi, et al., Appl. Surf. Sci. 257 (2011) 6531.
[12] A. Bostwick, et al., Nat. Phys. 3 (2007) 36.
[13] S.Y. Zhou, et al., Nat. Mater. 6 (2007) 770.
[14] X. Wu, et al., Appl. Phys. Lett. 95 (2009) 223108.
[15] J. Jobst, et al., Phys. Rev. B 81 (2010) 195434.
[16] K.V. Emtsev, et al., Nat. Mater. 8 (2009) 203.

Manuscript accepted for the Siam Physics Congress 2008, Nakhon Ratchasima (2008)

Elimination of Charging Effects in Total-electron-yield XAS Measurements

J.Osaklung[1], H.Nakajima[2], W.Meevasana[2,3] and P.Songsiriritthigul[1,2,*]

[1]*School of Physics, Suranaree University of Technology, Thailand*
[2]*Synchrotron Light Research Institute, Nakhon Ratchasima, Thailand*
[3]*Department of Physics, Stanford University, Stanford, California, USA*

We demonstrate the technique to avoid the building up of charge on the surface of an insulating specimen in total-electron-yield X-ray absorption (TEY XAS) measurements. Microscope slide-cover glass was used as a test specimen. In TEY XAS measurements, the photon energy range was chosen to study Si L-edge absorption spectra. Photo-excitation of the specimen causes charging on the surface. Charging can be observed from the shift of the kinetic energy of the photoelectrons toward lower values. The absorption edge could not be observed with such a specimen. The charging effects could be reduced when a thin Pt film was deposited on the specimen. With a proper thickness, the charging effects could be eliminated and thus good TEY XAS spectra could be obtained.

Keywords: Charging effects, XAS, Photoelectron, X-PEEM

1. INTRODUCTION

X-ray Photoemission Electron Microscopy (X-PEEM) is a powerful tool for nano-spectroscopy. X-PEEM is a combined microscopic and spectroscopic technique, namely spectromicroscopy. In X-PEEM measurements, monochromatized synchrotron light is focused on the surface of the specimen causing photoelectron and/or Auger electron ejection. The photo-excited electron beam is accelerated and magnified by a series of magnetic or electrostatic lenses. The magnified electron beam finally forms an image on a microchannel plate and phosphor screen assembly [1]. By scanning of photon energy, a series of images can be obtained and the total-electron-yield X-ray absorption (TEY XAS) spectra can be collected on a micron to nanometer scale. This provides possibilities to obtain element-specific electronic and structural information at the atomic scale from nano-structures or interested areas with nanometer spatial resolution. However, TEY XAS measurements are limited only for conducting specimens. Insulating specimens suffer severely from charging effects, building by clustering positive holes created with the ejection of photoelectrons and Auger electrons [2-4]. In this work, thus, we demonstrate a technique to suppress or eliminate the charging effects in TEY XAS measurements on insulating samples.

2. EXPERIMENT

Microscope slide-cover glass made by MENZEL-GLASER [5] (72.20% of SiO_2, 14.30% of Na_2O, 6.40% of CaO, 4.30% of MgO, 1.20 % of K_2O, 1.20% of Al_2O_3, 0.30% of SO_3 and 0.03% of Fe_2O_3), was used as an insulating test sample in this work. The experiments were performed at the multi-UHV-chamber photoemission end station of the BL4 beamline of the Siam Photon Laboratory (SPL) [6-7]. The measurement set up is shown in figure 1.

The suppression or elimination of charging effects on the surface of the insulating sample was done by coating a thin Pt film. The Pt deposition was carried out in a molecular beam deposition (MBD) system connected to the

*Corresponding author. Tel.: + 668945 9032; fax: + 66 4421 7047
E-mail: prayoon@slri.or.th

photoemission experimental station. The base pressure of the MBD system was $\sim2\times10^{-10}$ torr. The "average" thickness of the Pt film was varied between ~2 and 4 monolayers (MLs). After deposition, the sample was transferred in vacuum from the MBD chamber to the photoemission analysis chamber by the sample transfer system, allowing *in-situ* measurements and thus preventing contamination on the surface of the sample. The magnitude of charging was deduced from the shift of the kinetic energy of the Pt $4f$ photoelectrons measured by a VG Scientific CLAM2 electron energy analyzer.

3. RESULTS AND DISCUSSIONS

a. Observation of Charging Effects

As expected, it was not possible to obtain good photoelectron spectra of a bare clean microscope slide-cover glass when excited by 110-eV photons. The ejected photoelectrons and/or Auger electrons leave positive holes on the surface, which cannot be neutralized since the surface of the sample is not conducting. The building up of excessive charges modifies the kinetic energy of the emitting photoelectrons resulting in the shift and broadening
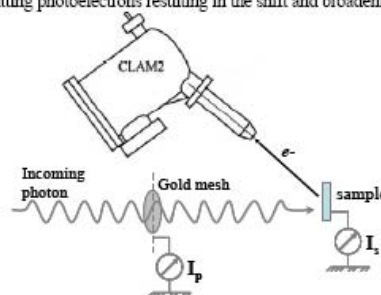

FIGURE 1. A measurement set-up showing only important elements. A CLAM2 electron energy analyzer was used for measuring photoelectron spectra. TEY XAS spectra were deduced from the sample drain current (I_s) and the drain current of a gold mesh (I_p).

Abstract submitted for the Siam Physics Congress 2009, Phetchburi (2009)

Low-energy Ion Bombardment of Nafion® Membrane

Y. Rattanachai[1], J. Osaklung[1], T. Puntheeranurak[4], H. Nakajima[2] and P. Songsiriritthigul[1,2,3]*

[1]School of physics, Suranaree University of Technology
[2]Synchrotron Light Research Institute, Nakhon Ratchasima, Thailand
[3]Nanospectroscopy Laboratory – ThEP Center, Nakhon Ratchasima, Thailand
[4]Department of Biology, Faculty of Science, Mahidol University, and Center of Excellence, National Nanotechnology Center at Mahidol University, Bangkok, Thailand

Abstract

Nafion® membranes bombarded by low-energy Ar^+ ions were investigated. The energy of the ions was varied from 0.5 to 3 keV. A mass spectrometer was used to analyze the fragmentations during the ion bombardment. The morphology of the bombarded surface was studied by AFM. The ion bombardment induced the change in chemistry of the surface as observed from photoemission measurement. The relation between the ion energy, fragmentation, surface morphology and the change in the electronic structure will be discussed in this report.

Keyword: nafion membrane, AFM, photoemission spectroscopy, fragmentation

* Corresponding author. Email: prayoon@slri.or.th

Abstract submitted for the Siam Physics Congress 2010, Kanchanaburi (2010)

LEEM investigations of epitaxial graphene formed by thermal decomposition of 6H-SiC(0001)

J. Osaklung[1], C. Euaruksakul[2], P. Songsiriritthigul[1,2,3*]

[1]School of physics, Suranaree University of Technology
[2]Synchrotron Light Research Institute (Public organization), Nakhon Ratchasima, Thailand
[3]Nanospectroscopy Laboratory – ThEP Center, CHE, Bangkok, Thailand

Abstract

This report presents preliminary results from the investigations of epitaxial graphene formed by thermal composition of a 6H-SiC(0001) crystal. The formation of the graphene was carried out in an Elmitec LEEM-PEEM III system at the Siam Photon Laboratory. The LEEM system allows the sample to be heated to form epitaxial graphene, and to be characterized _in-situ_. The surface morphology was observed from the LEEM imaging mode while the crystal surface structure of the sample was obtained from the diffraction mode, know as LEED or low energy electron diffraction. The reflectivity as a function the electron energy deduced from the LEEM images shows that epitaxial graphene was formed on the 6H-SiC(0001) after heating at ~1300°C. _Ex-situ_ AFM measurements were also been performed to observe the surface morphology after the heat treatment.

Keyword : Graphene, SiC, LEEM.

[*]Corresponding author: prayoon@slri.or.th

Abstract submitted for the Siam Physics Congress 2011, Chonburi (2011)

Spatial variation of graphene layers formed on scratched 6H-SiC(0001) surface

J. Osaklung[1], C. Euaruksakul[2], W. Meevasana[1,2,3], P. Songsiriritthigul[1,2,3*]

[1]*School of physics, Suranaree University of Technology, Nakhon Ratchasima, 30000, Thailand*
[2] *Synchrotron Light Research Institute, Nakhon Ratchasima, 30000, Thailand*
[3] *Thailand Center of Excellence in Physics, CHE, Bangkok, 10400, Thailand*
*Corresponding author. E-mail: prayoon@slri.or.th

Abstract

Over the last half decade, graphene, a monolayer of graphite, has shown various unique properties. One of these includes high carrier mobility which promises electronic devices with performance exceeding the conventional semiconductors. As these properties can depend on the number of graphene layers, precise growth control over a large area is needed for applications in electronic devices. Here, by using low energy electron microscopy (LEEM), we investigate how the scratching on surface of 6H-SiC(0001) could affect the epitaxial growth of graphene layers. The oscillation in the LEEM reflectivity as a function of electron energy shows that the numbers of graphene layers differ between the scratched and unscratched areas. By using atomic-force-microscopy (AFM), scratch width on the SiC substrate is extracted for comparing with the width of graphene formed along the scratch.

Keywords: Graphene, LEEM, AFM, Scratching on surface.

CURRICULUM VITAE

Miss Jarin Osaklung was born on February 7, 1977. She received her B.Sc. in physics with second-class honours from Kasetsart University in 1998 through a Thai government scholarship from the Development and Promotion of Science and Technology Talent Project (DPST). She continued her master study in physics at Suranaree University of Technology under the supervision of Professor Edward B. Manoukian. Then, she obtained a position as a physics lecturer at Kasetsart University in 2001. In 2007, she decided to pursue her Ph.D. study in physics at Suranaree University of Technology under the supervision of Assoc. Prof. Prayoon Songsiriritthigul using a scholarship from the Office of the Higher Education Commission, Thailand, under the program of Strategic Scholarships for Frontier Research Network. She investigated the structural and electrical properties of graphene grown on Silicon Carbide using various synchrotron radiation techniques, in particular, Photoemission Electron Microscopy (PEEM) and Low Energy Electron Microscopy (LEEM). During her Ph.D study, she had an opportunity to build, install and operate a new PEEM beamline at the Synchrotron Light Research Institute (Thailand), designed a plasma chamber for her experiment, worked in a clean room environment, and operated ultrahigh vacuum systems.